Doctoral Dissertation

Direct Numerical Simulation of Hindered Settling of Particles

Syed Ali Abbas Zaidi

January 2015

Graduate School of Engineering

Osaka University

Table of contents

Chapter 1 **Introduction**

1.1 Background

1.1.1 Multiphase flows

Multiphase flow is the ‘phenomenon’ that is composed of states of matter like gas state, liquid state, solid state. They can be classified according to the combination of the different phases into four categories: gas-liquid, gas-solid, liquid-solid or three phase flows. It is worthwhile to notice that multiphase flows are ubiquitous and have wide application areas. Virtually most of the processing technologies deal with multiphase flow, for example: spray drying, pollution control, papermaking, pneumatic transport, fluidized beds, slurry flows, hydro and sediment transport[1]. The amount of granular material, coal, grain, ore, etc. that is transported every year is enormous. It is roughly estimated according to one of the surveys[2] of NASA (National Aeronautics & Space Administration) that the transport and handling operations of granular materials using hoppers, chutes, belts and pneumatic conveyors account for one trillion dollars a year in gross sales in United States (with 63 percent of capacity). Hence, it is important to study these processes to increase their efficiency and effectiveness.

Multiphase flows which will be discussed in this thesis are the fluid-solid multiphase flows that contain the liquid-solid and gas-solid flows. In the fluid-solid multiphase flows, the solid phase cannot be limited to particles; they might be cells, leaves, or snowflakes. In the particle inertia dominant flows, the particle-particle and particle-wall interactions are also important in addition to the forces due to the interstitial fluid. If the particles become motionless the problem is reduced to flow through a porous medium in which the viscous and pressure forces on the particle surface is the primary mechanism affecting the gas flow (e.g. pebble-bed heat exchanger in which inert gases like helium or nitrogen passes through stationary balls of hot nuclear fuel). On the other hand in moving-particle cases, particles experience different fluid drag owing to the changing arrangements of neighbor particles. These are called hydrodynamic interactions[3] and are long range which makes the suspension microstructure constantly changing.

1.1.2 Hindered settling

The topic which is specifically studied in this thesis is hindered settling. The main motivation is that the results from hindered settling can be easily applied to other fluid-solid multiphase processes e.g. aerosols, sprays, separation processes, spreading of nuclear wastes, pneumatic transport, circulating fluidized bed, cleaning of water etc. Hindered settling is the settling of suspension through fluid under the action of body force and inter-particle hydrodynamics interactions.

The main sources of interferences between particles are inter-particle hydrodynamic interactions and particle-particle collisions. The inter-particle hydrodynamic interactions are formed when the fluid structures from one particle are experienced by another particle. These interactions make hindered settling a dynamic and complex process as the particles are constantly changing their positions and make it necessary to track each particle. Moreover, these long range interactions can lead to either particle dispersion or clustering depending upon the imposed boundary and initial conditions. All these characteristics of hindered settling make it quite challenging both in experiments and numerical simulations.

1.1.3 Importance of numerical simulations

Experiments can be performed for the study of multiphase flows but they pose two severe limitations. First the quality of experiments strongly depends on how well the experimental conditions are controlled. For example, in experiments involving solid particle suspensions, the results depend on the polydispersity and non-sphericity of particles. Furthermore, during experiments change in temperature can change the viscosity of suspended fluid and thus the settling Reynolds number. Thus to get a better understanding by experiments, one must put great effort in improving the experimental conditions such that the factor of interest can be isolated and other non-ideal effects can be minimized. Second, even in well-controlled experiments, quantities such as the fluctuations in particle velocities, drag force on particles and microstructures during settling are difficult to measure. These quantities are important for the understanding of the rheology of the suspension.

Computer simulations can be a very useful tool for the understanding of such flows,

design and scale-up of such processes. In simulations, the methods which are widely used for designing these systems must be capable of simulating large size systems and should not be computationally very expensive. These methods include Eulerian-Eulerian (e.g. two-fluid models[4,5]) and Eulerian-Lagrangian methods (e.g. CFD-DEM model[6-10]). The Eulerian-Eulerian approaches fall under the category of mesoscopic simulations. The two-fluid model assumes both the gas and the solid phases as inter-penetrating continua and is computationally cost-efficient when the volume fractions of the phases are comparable, or when the interactions within and between the phases play a significant role in determining the hydrodynamics of the system. On the other hand, the Eulerian-Lagrangian approaches are classified into mesoscopic and microscopic simulations. In the Eulerian-Lagrangian mesoscopic simulations, the flow of continuum fluid is described by the local averaged fluid equations that can be solved by Computational Fluid Dynamics (CFD), for particle-particle interactions Discrete Element Methods[11] (DEM) can be used. These methods are computationally more expensive in dense solid flows, however require less assumptions and the particle properties like particle size and density distributions can be directly taken into account in the simulation.

In either of the above two approaches, flow domain is divided into cells, the size of which is smaller than the mesoscopic structures like bubbles or clusters of particles but larger than the particle size. The model equations rely on various constitutive relations to account for the unknown terms emerging from averaging-fluid-particle drag, added-mass, lift, history force, solid phase stresses and fluid phase stresses. With the advancement of computing power and numerical methods microscopic Eulerian-Lagrangian or particle resolved direct numerical simulation (DNS) has become possible. In DNS the grid size is smaller than the size of particle thus it eliminates the need of additional closure terms in the fluid equations. These closure terms are necessary for other two approaches mentioned before. Reliable and accurate results can be obtained in DNS by careful selection of grid and simulation parameters. By using DNS one can have a better control of parameters which can certainly increase the insight for understanding the suspensions. The aim of this thesis is by using DNS provide more accurate correlations for fluid-solid flows and increase the understanding of these flows.

1.2 Purpose and outline of thesis

The aim of this thesis is to give possible explanations of the phenomena occurring in hindered settling for different ranges of Reynolds number and solid volume fractions. In chapter 2 the details of the methods which are used in the simulations are given. The main investigations are given in chapter 3 to 5. At the end in chapter 6, the thesis is concluded by principal investigations. The explanation about following the mentioned sequence of thesis and importance of this study is given in the following paragraphs.

Before actually performing the simulations for hindered settling, first it is necessary to study the parameters e.g. grid resolution, domain size, flow direction and ensemble averaging which can affect the results. In Chapter 3 these parameters are studied extensively to make sure that the results in the coming chapters will be reliable. In Chapter 3, besides the study of affecting parameters, drag force on fixed spheres are also studied. Drag force on fixed spheres are studied by Hill et al.[12,13], Beetstra et al.[14] and Tenneti et al.[15] using numerical simulations. The primary objective of the study by Hill et al.[12,13] was to investigate the relationship of average drag force with Reynolds number up to $Re \leq 100$. The objective of the study by Beetstra et al.[14] was to propose a drag correlation for Reynolds number up to 1000. Both of these studies employed Lattice Boltzmann method (LBM). Tenneti et al.[15] used Immersed Boundary method (IBM) and proposed a drag correlation for Reynolds number up to 300. The novelty of chapter 3 is to study the relationship of average drag force on spheres with Reynolds number up to $Re \leq 1000$. It benchmark the study done by Hill et al.[12,13] and also present the change of slope of the linear curve between average drag force and Reynolds number which was not studied by Hill et al.[12,13]. At the end of this chapter, possible explanation of this change of slope is given and a new drag correlation is proposed which is valid for Reynolds number 1000 and more reliable than the relation proposed by Beetstra et al.[14]

The main objectives of this thesis and the study of hindered settling are covered in chapter 4 and 5. In these chapters, solid volume fractions and Reynolds number are studied up to 0.4 and 300 respectively. The literature review about low Reynolds number can be found in Chapter 4. This thesis is focused on the study of hindered settling for moderate and high Reynolds number. For moderate Reynolds number ($Re \leq 20$), Climent and Maxey[16], Yin and Koch[17,18] performed numerical simulations.

The work of Climent and Maxey[16] was focused on the benchmarking of their force coupling method and code and not on the explanation of phenomenon occurring in hindered settling. Yin and Koch[17,18] used an LBM code for studying hindered settling. They used SUSP3D[19,20] code developed by Ladd. In SUSP3D code, the effective diameter that was approximated by the comparison with the theoretical equation was used and it can give unreliable results. Moreover, their simulations were more focused for dense suspensions. For high Reynolds number (about $Re>175$), Kajishima and Takiguchi[21], Kajishima[22] and Douchev et al.[23] performed numerical simulations. All these work were more focused on particle clusters formation for very dilute suspension and turbulence enhancement by these clusters. The objective of Chapter 4 is to study the effects of two body (characteristics of dilute suspension) and multi-body (characteristics of dense suspension) interactions in hindered settling for moderate Reynolds number ($Re\leq50$). The novelty of this chapter is the study of non-linearity of average settling velocity due to the increase in two body interactions with Reynolds number, the study of the paradox of increase in velocity fluctuations with domain size which is generally present in numerical simulations for moderate Reynolds number and dispersion of particles in dilute suspension by increase in Reynolds numbers.

In Chapter 4, it is observed that the effects of Reynolds number are about negligible for high solid volume fractions. Thus in Chapter 5, dilute suspension is studied in detail. The novelty of chapter 5 is the study of inverse effect of solid volume on particle clustering at high range of Reynolds number and proposing that the ratio of average particle velocity to fluid velocity fluctuations can be used as an indicator of particle clustering in particle induced turbulence. Previously[24], this ratio was used as a measure of particle clustering for point particles in homogenous turbulence.

Chapter 2 **Formulation**

In this thesis, for particle-fluid interactions Immersed Boundary Method (IBM) is used. IBM lies in the category of particle resolved direct numerical simulations (DNS) and for particle-particle interactions Discrete Element Method (DEM) is used. The reason for using IBM is that IBM can capture the flow structures formed during settling and the underlying physical phenomenon without any empirical relation. Since the particles simulated in the simulations are of finite size thus point particle DNS approach which employs one-way coupling is not sufficient. Furthermore in hindered settling, particles settle freely and sometimes collide with each other. The reason for using DEM is to model these particle-particle collisions. The description of these methods is given in the following sections.

2.1 Fluid calculations

2.1.1 Introduction

For fluid calculations Immersed Boundary Method (IBM) is used. IBM is a method first proposed by Peskin[25] to simulate cardiac mechanics and associated blood flow. The distinguishing feature of this method is that the entire simulation is carried out on a Cartesian grid, which does not conform to the geometry of the heart, and a novel procedure is formulated for imposing the effect of the immersed boundary (IB) on the flow. After the introduction of this method by Peskin, numerous modifications, refinements and a number of variants of this approach have been proposed.

2.1.2 Immersed Boundary Method (IBM)

2.1.2.1 Fluid equations and steps in IBM

The basic equations for fluid flow are the equations of continuity and incompressible Navier-Stokes equation which are given by:

$$\nabla \cdot \boldsymbol{u}_f = 0 \tag{2.1}$$

$$\frac{\partial \boldsymbol{u}_f}{\partial t} + \boldsymbol{u}_f \cdot \nabla \boldsymbol{u}_f = \nu \nabla^2 \boldsymbol{u}_f - \frac{\nabla p}{\rho} \tag{2.2}$$

where $\boldsymbol{u}_f$ is the fluid velocity, ρ is the density, ν is the kinematic viscosity and p is the pressure.

The IBM used in current simulations is proposed by Kajishima et al.[26]. It is a body-force type IBM in which fluid can be liquid or gas but it is assumed to be incompressible and Newtonian. The solid particles are assumed to be rigid spheres and the grid for performing fluid calculations remains fixed. The grid size used for discretizing the computational domain is smaller than the size of particles and fluid flow equations are solved by assuming that the fluid occupies the entire flow field and the effect of particles is expressed by a body force in the momentum equation which constrains the no slip boundary condition at the particles surface. For improving the efficiency of numerical integration fluid-particle volume-weighted velocity $(\boldsymbol{u})$ is defined, which is given by:

$$\boldsymbol{u} = \alpha \boldsymbol{u}_p + (1 - \alpha)\boldsymbol{u}_f \tag{2.3}$$

where $\boldsymbol{u}_p$ is the velocity inside the solid particle and α is the volume fraction of particle at a target cell. α takes the value zero for fluid and one for particle and in the range of zero to one at the particle interfacial cell. The velocity inside the solid particle is defined by:

$$\boldsymbol{u}_p = \boldsymbol{v}_p + \boldsymbol{\omega}_p \times \boldsymbol{r} \tag{2.4}$$

where $\boldsymbol{v}_p$ is the velocity of particle center, $\boldsymbol{\omega}_p$ is the angular velocity of particle rotation and $\boldsymbol{r}$ is the unit vector from the center of rotation to the surface. For the case of no slip and no permeable conditions at the interface ($\boldsymbol{u}_f = \boldsymbol{u}_p$), the continuity restriction should also be satisfied for $\boldsymbol{u}$. The momentum equation of fluid in IBM is given by:

$$\frac{\partial \boldsymbol{u}}{\partial t} + \boldsymbol{u} \cdot \nabla \boldsymbol{u} = \nu \nabla^2 \boldsymbol{u} - \frac{\nabla p}{\rho} + \boldsymbol{f}_p \tag{2.5}$$

where $\boldsymbol{f}_p$ is the force to modify the flow predicted as if the field is occupied by fluid to the velocity defined by Eq. (2.3). The time-marching of Eq. (2.5) consist of time integral which is given by:

$$\boldsymbol{u}_{n_0+1} = \boldsymbol{u}_{n_0} + \Delta t\left(-\frac{\nabla p}{\rho} - \boldsymbol{u}\cdot\nabla\boldsymbol{u} + \nu\nabla^2\boldsymbol{u} + \boldsymbol{f}_{pd}\right)_{n_0} \tag{2.6}$$

where n_0 denotes the previous time step, $\boldsymbol{f}_{pd}$ is the forcing term in discretized form and Δt is the time increment. The time-marching consists of two steps. In the first step the fluid velocity is predicted by using Eq. (2.2) without $\boldsymbol{f}_{pd}$:

$$\tilde{\boldsymbol{u}} = \boldsymbol{u}_{n_0} + \Delta t\left(-\frac{\nabla p}{\rho} - \boldsymbol{u}\cdot\nabla\boldsymbol{u} + \nu\nabla^2\boldsymbol{u}\right)_{n_0} \tag{2.7}$$

Then this predicted velocity ($\tilde{\boldsymbol{u}}$) should be modified by $\boldsymbol{f}_{pd}$ to meet the definition of $\boldsymbol{u}_{n_0+1}$. For the cell inside the particle ($\alpha = 1$), $\boldsymbol{f}_{pd} = \alpha_{n_0}(\boldsymbol{u}_{p_{n_0}} - \tilde{\boldsymbol{u}})/\Delta t$ gives $\boldsymbol{u}_{n_0+1} = \boldsymbol{u}_p$. For the cell occupied by fluid ($\alpha = 0$) Eq. (2.6) is identical to Eq. (2.7) because of $\boldsymbol{f}_{pd} = 0$. For the calculation of $\boldsymbol{f}_{pd}$, first order linear interpolation of α is used. The forcing term is given by:

$$\boldsymbol{f}_{pd} = \alpha_{n_0}(\boldsymbol{u}_{p_{n_0}} - \tilde{\boldsymbol{u}})/\Delta t \tag{2.8}$$

The fluid force $\boldsymbol{F}_f$ and fluid moment $\boldsymbol{M}_f$ on a particle are calculated by the volume integral equations given by:

$$\boldsymbol{F}_f = -\rho\int_{Vp}\boldsymbol{f}_{pd}dv \quad + \boldsymbol{G}_p \tag{2.9}$$

$$\boldsymbol{M}_f = -\rho\int_{Vp}\boldsymbol{r}\times\boldsymbol{f}_{pd}dv + \boldsymbol{N}_p \tag{2.10}$$

where Vp is the volume of cube whose sides are equal to the sphere diameter and enclosing all the interfacial cells, $\boldsymbol{G}_p$ and $\boldsymbol{N}_p$ are the external forces and moments respectively.

2.1.2.2 Calculation of $\boldsymbol{\alpha}$ in IBM

Evaluation of α in a cell is critical in this method. It can be calculated with exact

geometrical shape of surface. But this is very time consuming especially in three-dimensional computations. In the original method by Kajishima et al.[26], the surface is approximated by tangential planes normal to the relative vector from the center of particle to a center of interfacial cells. Although this method reduces the computational time, but in three-dimensional simulations, it is not so easy to generate the tangential planes at each interfacial cell. Besides, when the number of particles increases, it is expected that it still occupy significant part of total computation time. To solve these problems, Tsuji et al.[27] proposed a new method which they called Subdivision Volume Counting (SVC). In this method, each interfacial cell is subdivided into small elements. If the length between the center of particle and element is shorter than the particle radius, the volume of the element is counted as particle in this cell. This can be seen in Fig. 2.1.

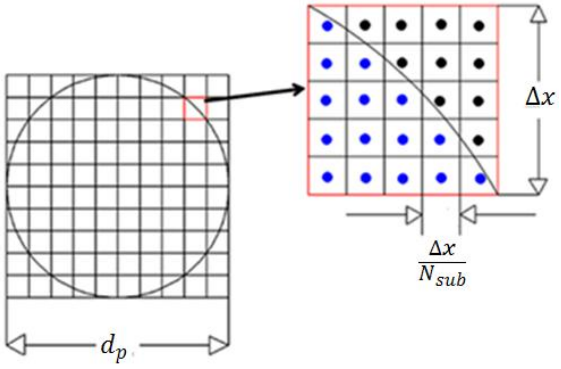

Fig. 2.1 Subdivision volume counting method[27]

where Δx =mesh size, d_p is the particle diameter and N_{sub} is the number of sub-divisions in Δx. In simulations, it is observed that for fine resolutions i.e. $d_p/\Delta x \geqq 16$, $N_{sub} \geqq 6$ takes the volume in the cell with an error of order of magnitude O(10^{-5}). In all studied cases, $d_p/\Delta x \geqq 16$ thus $N_{sub}=6$ is used.

2.1.2.3 Time marching of fluid equation

In simulations for advancing the unsteady fluid equation Eq. (2.7) to the next time step, fractional step method is used. In this method, pressure is used to enforce continuity. This method consists of predictor and corrector step. In the predictor step (Eq. (2.12) and Eq. (2.13)) the momentum equation is solved, without taking into account of pressure term and only convective $\boldsymbol{C}$ and diffusive $\boldsymbol{D}$ terms are solved sequentially. In the corrector step Eq. (2.14), the poison equation for pressure is solved

so that continuity equation is satisfied. The time advancement of fractional step method is as follows:

$$\tilde{\boldsymbol{u}}_{n^0+1} = \tilde{\boldsymbol{u}}_{n^0} + \Delta t(\boldsymbol{C} + \boldsymbol{D} + p)_{n^0} \tag{2.11}$$

$$\tilde{\boldsymbol{u}}_{*} = \tilde{\boldsymbol{u}}_{n^0} + \Delta t(\boldsymbol{C})_{n^0} \tag{2.12}$$

$$\tilde{\boldsymbol{u}}_{**} = \tilde{\boldsymbol{u}}_{*} + \Delta t(\boldsymbol{D})_{n^0} \tag{2.13}$$

$$\tilde{\boldsymbol{u}}_{n^0+1} = \tilde{\boldsymbol{u}}_{**} + \Delta t(p)_{n^0} \tag{2.14}$$

where $\tilde{\boldsymbol{u}}_{*}$ and $\tilde{\boldsymbol{u}}_{**}$ are the fluid velocities at the fractional step. In the simulations the fluid equations are discretized by staggered grid in the orthogonal coordinate system shown in Fig. 2.2. Staggered grid has a property that the pressure oscillations in the solution can be prevented.

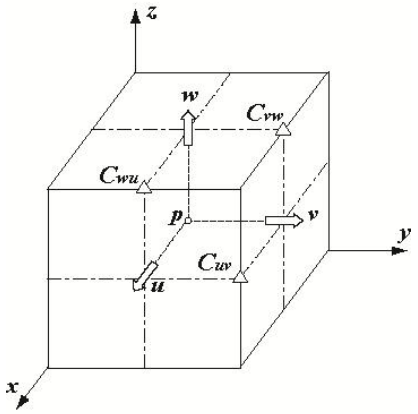

Fig. 2.2 Variable array of three dimensional staggered grid

2.1.2.4 Spatial difference approximation for convection term

The convection term in the Navier Stokes equation is given by Eq. (2.15). It can be seen that it has non-linear terms, the convection term in the Cartesian coordinate system is given by Eq. (2.15).

$$C_x = u\frac{\partial u}{\partial x} + v\frac{\partial u}{\partial y} + w\frac{\partial u}{\partial z}$$

$$C_y = u\frac{\partial v}{\partial x} + v\frac{\partial v}{\partial y} + w\frac{\partial v}{\partial z} \qquad (2.15)$$

$$C_z = u\frac{\partial w}{\partial x} + v\frac{\partial w}{\partial y} + w\frac{\partial w}{\partial z}$$

where u, v and w are the components of fluid velocity and C_x, C_y and C_z are convective term in x, y and z Navier-Stokes equations. The difference stencil used in simulation is given by Fig. 2.3 and the interpolation terms for the convection terms are given by Eq. (2.16), Eq. (2.17) and Eq. (2.18) in the calculation of *x* component of convection term in the Navier-Stokes equation.

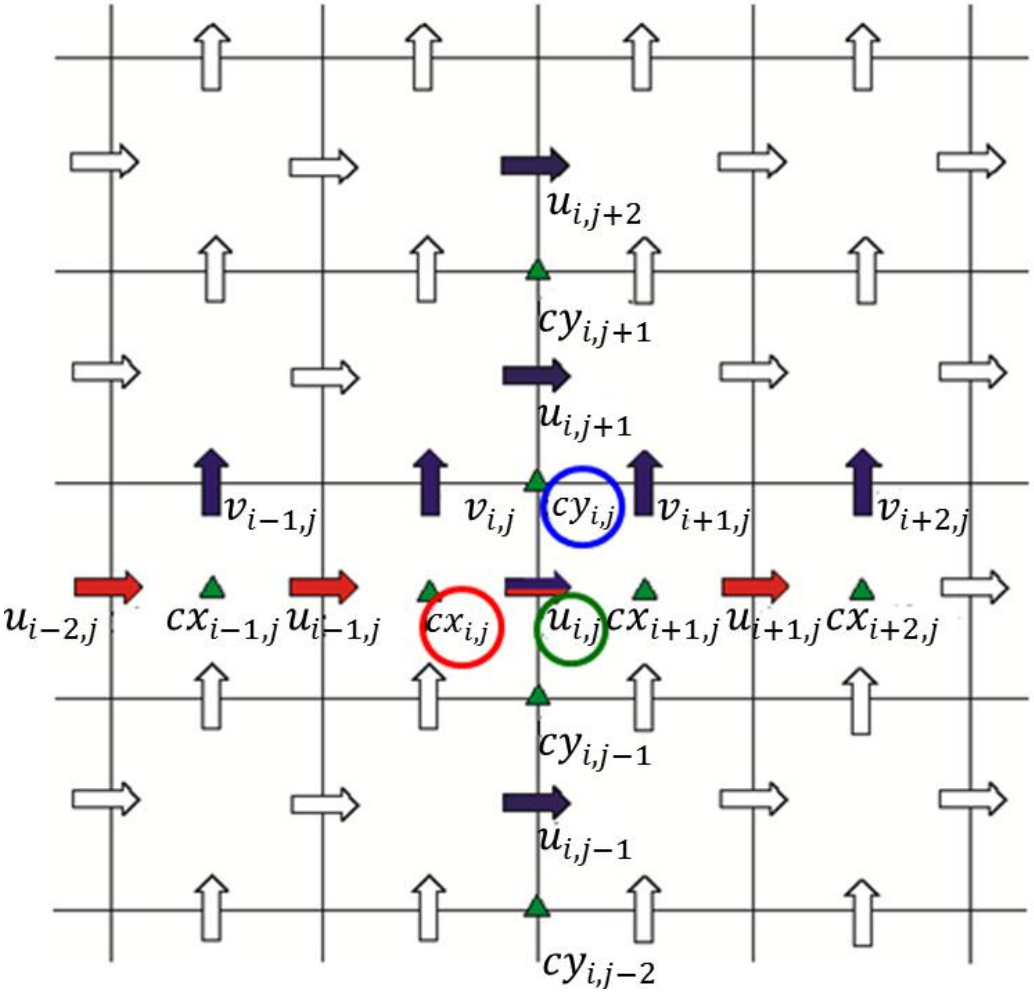

Fig. 2.3 Discretization stencil for convection term

$$cx_{i,j,k} = \frac{1}{16}\left(-u_{i-2,j,k} + 9u_{i-1,j,k} + 9u_{i,j,k} - u_{i+1,j,k}\right) \times \frac{1}{24\Delta x}\left(u_{i-2,j,k} - 27u_{i-1,j,k} + 27u_{i,j,k} - u_{i+1,j,k}\right) \tag{2.16}$$

$$cy_{i,j,k} = \frac{1}{16}\left(-v_{i-1,j,k} + 9v_{i,j,k} + 9v_{i+1,j,k} - v_{i+2,j,k}\right) \times \frac{1}{24\Delta y}\left(u_{i,j-1,k} - 27u_{i,j,k} + 27u_{i,j+1,k} - u_{i,j+2,k}\right) \tag{2.17}$$

$$cz_{i,j,k} = \frac{1}{16}\left(-w_{i-1,j,k} + 9w_{i,j,k} + 9w_{i+1,j,k} - w_{i+2,j,k}\right) \times \frac{1}{24\Delta z}\left(u_{i,j,k-1} - 27u_{i,j,k} + 27u_{i,j,k+1} - u_{i,j,k+2}\right) \tag{2.18}$$

where $cx_{i,j,k}$, $cy_{i,j,k}$ and $cz_{i,j,k}$ are the interpolation terms in *x*, *y* and *z* directions, respectively. The convection term discretization represented by $A_{i,j,k}$ in *x*-direction is given by:

$$A_{i,j,k} = \frac{1}{16}\left(-cx_{i-1,j,k} + 9cx_{i,j,k} + 9cx_{i+1,j,k} - cx_{i+2,j,k}\right) + \frac{1}{16}\left(-cy_{i,j-2,k} + 9cy_{i,j-1,k} + 9cy_{i,j,k} - cy_{i,j+1,k}\right) + \frac{1}{16}\left(-cz_{i,j,k-2} + 9cz_{i,j,k-1} + 9cz_{i,j,k} - cz_{i,j,k+1}\right) \tag{2.19}$$

The *y* and *z* directions convection terms can also be discretized in a similar way.

2.1.2.5 Spatial difference approximation for viscous term

The viscous term in Navier-Stokes equation in the Cartesian coordinate system is given by Eq. (2.20).

$$D_x = \upsilon\left(\frac{\partial^2 u}{\partial x^2} + \frac{\partial^2 u}{\partial y^2} + \frac{\partial^2 u}{\partial z^2}\right)$$

$$D_y = \upsilon\left(\frac{\partial^2 v}{\partial x^2} + \frac{\partial^2 v}{\partial y^2} + \frac{\partial^2 v}{\partial z^2}\right) \tag{2.20}$$

$$D_z = \upsilon\left(\frac{\partial^2 w}{\partial x^2} + \frac{\partial^2 w}{\partial y^2} + \frac{\partial^2 w}{\partial z^2}\right)$$

where D_x, D_y and D_z are the diffusive terms in x, y and z Navier-Stokes equations. In the simulations, central differencing with fourth order accuracy is used. The viscous term discretization represented by $B_{i,j,k}$ in the *x*-direction is given by:

$$\begin{aligned} B_{i,j,k} = {} & \frac{1}{(24\Delta x)^2}(u_{i-3,j,k} - 54\,u_{i-2,j,k} + 783\,u_{i-1,j,k} \\ & -1460\,u_{i,j,k} + 783\,u_{i+1,j,k} - 54\,u_{i+2,j,k} + u_{i+3,j,k}) \\ & \frac{1}{(24\Delta y)^2}(u_{i,j-3,k} - 54\,u_{i,j-2,k} + 783\,u_{i,j-1,k} \\ & -1460\,u_{i,j,k} + 783\,u_{i,j+1,k} - 54\,u_{i,j+2,k} + u_{i,j+3,k}) \\ & \frac{1}{(24\Delta z)^2}(u_{i,j,k-3} - 54\,u_{i,j,k-2} + 783\,u_{i,j,k-1} \\ & -1460\,u_{i,j,k} + 783\,u_{i,j,k+1} - 54\,u_{i,j,k+2} + u_{i,j,k+3}) \end{aligned} \tag{2.21}$$

The *y* and *z* directions viscous terms can be discretized in a similar way.

2.1.2.6 Solution of Poison's equation for pressure

As mentioned in Section 2.1.4 that the correction step of fractional step method consists of solving the poison's equation for pressure for satisfying the continuity equation. The poison equation is elliptic form of partial differential equation with a non-zero term $f(x, y, z)$ on the right hand side. It can be written as:

$$\frac{\partial^2 p}{\partial x^2} + \frac{\partial^2 p}{\partial y^2} + \frac{\partial^2 p}{\partial z^2} = f(x, y, z) \tag{2.22}$$

During simulations, fourth order central differencing is used. In discretized form, Eq. (2.22) can be written as:

$$\begin{aligned}&\frac{-p_{i+2,j,k}+16p_{i+1,j,k}-30p_{i,j,k}+16p_{i-1,j,k}-p_{i-2,j,k}}{12(\Delta x)^2}\\&+\frac{-p_{i,j+2,k}+16p_{i,j+1,k}-30p_{i,j,k}+16p_{i,j-1,k}-p_{i,j-2,k}}{12(\Delta y)^2}\\&+\frac{-p_{i,j,k+2}+16p_{i,j,k+1}-30p_{i,j,k}+16p_{i,j,k-1}-p_{i,j,k-2}}{12(\Delta z)^2}=f_{i,j,k}\end{aligned} \tag{2.23}$$

In simulations, same grid spacing is used in all directions i.e. $\Delta x=\Delta y=\Delta z$ and for solving Eq. (2.22) point successive over-relaxation method (PSOR) is used. In PSOR, pressure at every grid point is evaluated using initial guessed values of neighboring grid points. Iterations are carried out until a specified convergence criteria is met (In present simulations it is 0.05). In order to speed-up the convergence process an over-relaxation parameter (w_1) is multiplied. The iteration process for PSOR method is given by Eq. (2.24). The superscript k_1 shows pressure at old iteration and k_1+1 shows pressure at new iteration.

$$\begin{aligned}{p_{i,j,k}}^{k_1+1}=&{p_{i,j,k}}^{k_1}+\frac{w_1}{90}(-{p_{i+2,j,k}}^{k_1}+16{p_{i+1,j,k}}^{k_1}-30{p_{i,j,k}}^{k_1}\\&+16{p_{i-1,j,k}}^{k_1+1}-{p_{i-2,j,k}}^{k_1+1}-{p_{i,j+2,k}}^{k_1}+16{p_{i,j+1,k}}^{k_1}\\&-30{p_{i,j,k}}^{k_1}+16{p_{i,j-1,k}}^{k_1+1}-{p_{i,j-2,k}}^{k_1+1}-{p_{i,j,k+2}}^{k_1}\\&+16{p_{i,j,k+1}}^{k_1}-30{p_{i,j,k}}^{k_1}+16{p_{i,j,k-1}}^{k_1+1}-{p_{i,j,k-2}}^{k_1+1}\\&-12(\Delta x)^2f_{i,j,k})\end{aligned} \tag{2.24}$$

2.2 Particle motion

During the simulations the particles are assumed to be spherical. In hindered settling the particles settle freely and develop relative motion with respect to each other. Sometimes this relative motion leads to particle-particle contact or particle-particle collision. In order to eliminate the non-physical situations of particle overlaps different approaches are used by different researchers. One approach[28] is to use artificial repulsion potential when the particles are in the vicinity of other particles. This approach is easy to implement but is generally reasonable for dilute suspensions. Another approach is to use hard sphere model. Hard sphere model assumes the particles to be rigid and solves the impulse equations of dynamics for the calculation of inter-particle forces. The hard sphere model is computationally less expensive but is

only applicable for modeling binary collisions or semi-dilute suspensions. One more approach which is reasonable for both dilute and dense suspensions is soft sphere model or discrete element method (DEM). DEM uses mechanical elements such as spring and dash-pot for modeling the contact force. The range of solid volume fractions (ratio of volume of particle to volume of the domain) studied in the present study will be explained in chapters 4 and 5. This study encompasses both dilute and dense suspensions thus DEM is used in the present simulations.

2.3 Discrete Element Method

The contact force model between particles in DEM is illustrated in Fig. 2.4.

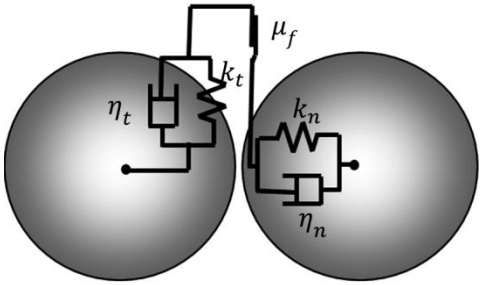

Fig.2.4 Contact force model

The contact force is divided into normal $\boldsymbol{f}_{Cn}$ and $\boldsymbol{f}_{Ct}$ tangential components which are given by:

$$\boldsymbol{f}_{Cn} = \left(-k_n\delta_n - \eta_n \boldsymbol{V}_{ij} \cdot \boldsymbol{n}\right)\boldsymbol{n} \tag{2.25}$$

$$\boldsymbol{f}_{Ct} = \min\left[(-k_t\boldsymbol{\delta}_t - \eta_t \boldsymbol{V}_{sij}, -\mu_f|\boldsymbol{f}_{Cn}|\boldsymbol{t}\right] \tag{2.26}$$

where δ_n and $\boldsymbol{\delta}_t$ are the displacements of particle caused by the normal and tangential forces respectively, k is the spring constant, η is the damping coefficient, μ_f is the friction coefficient, $\boldsymbol{t}$ is the tangential unit vector and $\boldsymbol{n}$ is the normal unit vector. $\boldsymbol{V}_{sij}$ is the tangential direction relative velocity of particle j with respect to particle i and can be expressed by Eq. (2.27). It is to be noted that $\boldsymbol{\delta}_t$ is a vector and its direction is generally not equal to the slip velocity vector $\boldsymbol{V}_{sij}$in three-dimensional motion.

$$\boldsymbol{V}_{sij} = -(\boldsymbol{V}_{ij} \cdot \boldsymbol{n})\boldsymbol{n} + (\boldsymbol{r}_i\boldsymbol{\omega}_i + \boldsymbol{r}_j\boldsymbol{\omega}_j) \times \boldsymbol{n} \tag{2.27}$$

$\boldsymbol{t}$ is the tangential unit vector which is given by:

$$\boldsymbol{t} = \frac{\boldsymbol{V}_{sij}}{|\boldsymbol{V}_{sij}|} \tag{2.28}$$

The function $\min[A, B]$ in Eq. (2.26) gives the smaller value of either *A* or *B*. It is used to take account the sliding of particles.

2.3.1 Viscous damping coefficient and stiffness

After modeling the contact forces between particles the next step is to determine the stiffness and the damping coefficient. During the contact of particles the dashpots represents the energy dissipation. The viscous damping coefficient is calculated from the coefficient of restitution (Tsuji et al, 1993). It is assumed that the collision between particles and the collision between particle and wall is head-on-collision in the normal direction. Thus the repulsive force can be calculated by the equation of motion for one-dimensional spring mass damped oscillation system given by the following equation.

$$m_p\ddot{x} + \eta\dot{x} + kx = 0 \tag{2.29}$$

Solving Eq. (2.29) under the initial conditions $v=v_i$ at $t=0$, $x=0$. where x is the displacement, v is the velocity and v_i is the initial velocity.

$$x = \frac{v_i}{q}\sin(qt)\exp(-\gamma\omega_0 t) \tag{2.30}$$

$$\dot{x} = \frac{v_i}{q}\exp(-\gamma\omega_0 t)\{q\cos(qt) - \gamma\omega_0\sin(qt)\} \tag{2.31}$$

where

$$\omega_0 = \sqrt{\frac{k}{m_p}} \tag{2.32}$$

$$\gamma = \frac{\eta}{2\sqrt{m_p k}} \tag{2.33}$$

$$q = \omega_0 \sqrt{1-\gamma^2} \tag{2.34}$$

As can be seen from Eq. (2.30) the period of oscillation is $2\pi/q$. At half period of oscillation i.e. $t=\pi/q$, the velocity will be:

$$v = \dot{x}|_{t=\pi/q} = -v_i(-\gamma\omega_0\pi/q) \tag{2.35}$$

We can obtain the following relationship from the definition of coefficient of restitution e_p.

$$e_p = {}^{v}/_{v_i} = (-\gamma\omega_0\pi/q) \tag{2.36}$$

Viscous damping coefficient ratio γ can be obtained by Eq. (2.34) and Eq. (2.36) which is given by:

$$\gamma = -\frac{\ln e_p}{\sqrt{\pi^2 + (\ln e_p)^2}} \tag{2.37}$$

Therefore the viscous damping coefficient η can be obtained by Eq. (2.33) which is given by:

$$\eta = -\frac{2\ln e_p}{\sqrt{\pi^2 + (\ln e_p)^2}}\sqrt{m_p k} \tag{2.38}$$

In the above derivation it was assumed that the coefficient of restitution e_p is constant. Thus it is possible to analytically obtain the viscous damping coefficient by Eq. (2.38).

Stiffness can be determined from the material properties like Young's modulus and Poisson's ratio. However it is often difficult in practice to use the stiffness calculated by the Hertzian theory, because the time step required for numerical integration becomes so small that an excessive amount of computational time is needed. The time step should be one-tenth of natural oscillation period of a spring-mass system (Tsuji et al., 1993) which is given by Eq. (2.39).

$$t = 2\pi\sqrt{\frac{m}{k}} \tag{2.39}$$

Fortunately for fluid-particle multiphase flows the results based on the stiffness much smaller than an actual value are not very different from those based on the precise value. Thus a much smaller value can be used for simulations.

2.3.2 Lubrication Force

IBM resolves the hydrodynamics and fluid force on particles at all times except when the gap between colliding particles becomes comparable to the grid step. To overcome this problem, Simenov and Calantoni[29] proposed a method to introduce analytical expressions of lubrication force for such small inter-particle distances in DNS. Details of this method can be find in the reference[29]. The normal component $\boldsymbol{f}_{ln}$ of lubrication force on *j*th particle due to relative translation with respect to *i*th particle along the line of center is given by.

$$\boldsymbol{f}_{ln} = 3\pi\mu d_p \lambda(\Omega)\left(\frac{1}{4}\left(\frac{1}{\Omega} - \frac{1}{\Omega_{res}}\right) - \frac{9}{40}\ln\left(\frac{\Omega}{\Omega_{res}}\right)\right)\left(\boldsymbol{U}_{ij}\cdot\boldsymbol{e}_{ij}\right)\boldsymbol{e}_{ij} \tag{2.40}$$

where μ is viscosity, $\boldsymbol{U}_{ij}$ is relative translation velocity $\boldsymbol{U}_{ij} = \boldsymbol{U}_j - \boldsymbol{U}_i$, $\boldsymbol{e}_{ij}$ is the unit vector from the center of particle *i* to particle *j* and $\lambda(\Omega)$ is a step function given by

$$\lambda(\Omega) = \begin{cases} 1 & \Omega_{res} > \Omega > \Omega_{cut} \\ 0 & \text{otherwse} \end{cases} \tag{2.41}$$

Ω_{res} is dependent on grid size. In the present simulations Ω_{res} is taken to be 1.5 times Δx and Ω_{cut} to be 10^{-4}mm.

The tangential force $\boldsymbol{f}_{lt}$ and torque $\boldsymbol{T}_{tt}$ on the *j*th particle due to relative translation with respect to *i*th particle in the direction perpendicular to the line of centers is given by.

$$\boldsymbol{f}_{lt} = -3\pi\mu d_p \lambda(\Omega) \ln\left(\frac{\Omega}{\Omega_{res}}\right)\left(\frac{1}{6}\left(\boldsymbol{U}_{ij} - (\boldsymbol{U}_{ij}\cdot\boldsymbol{e}_{ij})\boldsymbol{e}_{ij}\right)\right) \tag{2.42}$$

$$\boldsymbol{T}_{tt} = -2\pi\mu {d_p}^2 \lambda(\Omega) \ln\left(\frac{\Omega}{\Omega_{res}}\right)\left(\frac{1}{8}\left(\boldsymbol{e}_{ij}\times\boldsymbol{U}_{ij}\right)\right) \tag{2.43}$$

2.4 Parallelization

In order to reduce the computational time the fluid part of the code is parallelized with standard 1D domain decomposition using MPI routines[24]. As an example in Fig. 2.5 rectangular computational grid is divided among four nodes or processors. Each processor performs its own calculations and also communicates with neighbor processors.

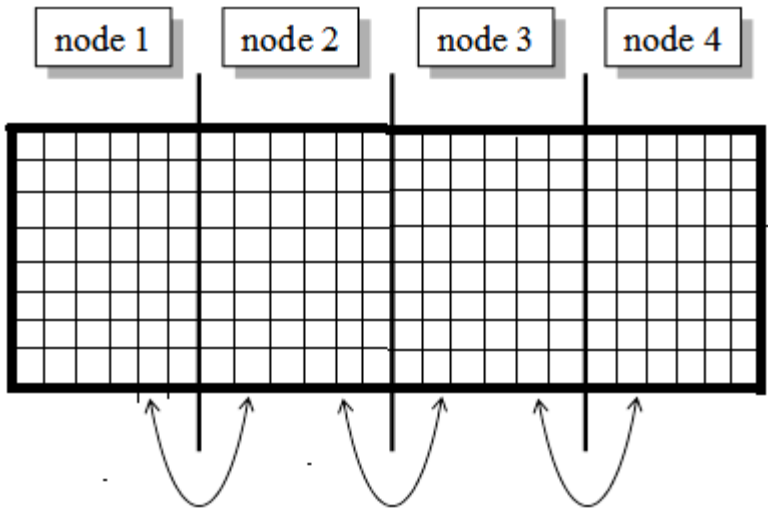

Fig. 2.5 Communication between neighbor nodes in global region

However the calculation of particle contacts in DEM part is not parallelized and information such as update of particle contact is performed at every computer node. The main reason for adopting this strategy is the number of particles simulated is of the order of 10^3, thus the parallelization of the DEM will not make big difference on the computational time. Furthermore, in parallelization of DEM part another problem arises i.e. the number of particles assigned with each node will be different this arises the problem of waiting time in some nodes. In the present approach every node is simulating same number of particles thus the above mentioned problem can be ignored.

2.5 Time marching of particles

For time marching of particle velocity Adams-Bashforth method is used.

$$\boldsymbol{V}_{p_{n_0+1}} = \boldsymbol{V}_{p_{n_0}} + \frac{\Delta t}{2m_p}\begin{pmatrix} 3\left(\boldsymbol{F}_{IB_{n_0}} + \boldsymbol{F}_{DEM_{n_0}} + \boldsymbol{F}_{lub_{n_0}} + \boldsymbol{F}_{g_{n_0}}\right) \\ -\left(\boldsymbol{F}_{IB_{n_0-1}} + \boldsymbol{F}_{DEM_{n_0-1}} + \boldsymbol{F}_{lub_{n_0-1}} + \boldsymbol{F}_{g_{n_0-1}}\right) \end{pmatrix} \tag{2.44}$$

$$\boldsymbol{\omega}_{p_{n_0+1}} = \boldsymbol{\omega}_{p_{n_0}} + \frac{\Delta t}{2I_p}\begin{pmatrix} 3\left(\boldsymbol{F}_{IB_{n_0}} + \boldsymbol{F}_{DEM_{n_0}} + \boldsymbol{F}_{lub_{n_0}}\right) \\ -\left(\boldsymbol{F}_{IB_{n_0-1}} + \boldsymbol{F}_{DEM_{n_0-1}} + \boldsymbol{F}_{lub_{n_0-1}}\right) \end{pmatrix} \tag{2.45}$$

where $\boldsymbol{V}_p$ and $\boldsymbol{\omega}_p$ are the particle translational and rotational velocities. $\boldsymbol{F}_{IB}$, $\boldsymbol{F}_{DEM}$, $\boldsymbol{F}_{lub}$ and $\boldsymbol{F}_g$ are the forces due to IBM, DEM, lubrication force and gravity respectively. I_p is the moment of inertia. For time marching of particle displacement $\boldsymbol{X}_p$, Crank-Nicholson method is used.

$$\boldsymbol{X}_{p_{n_0+1}} = \boldsymbol{X}_{p_{n_0}} + \Delta t\left(\frac{\boldsymbol{V}_{p_{n_0}} + \boldsymbol{V}_{p_{n_0-1}}}{2}\right) \tag{2.46}$$

2.6 Flowchart

Fig. 2.6 shows the flow chart of the calculation used in the present thesis.

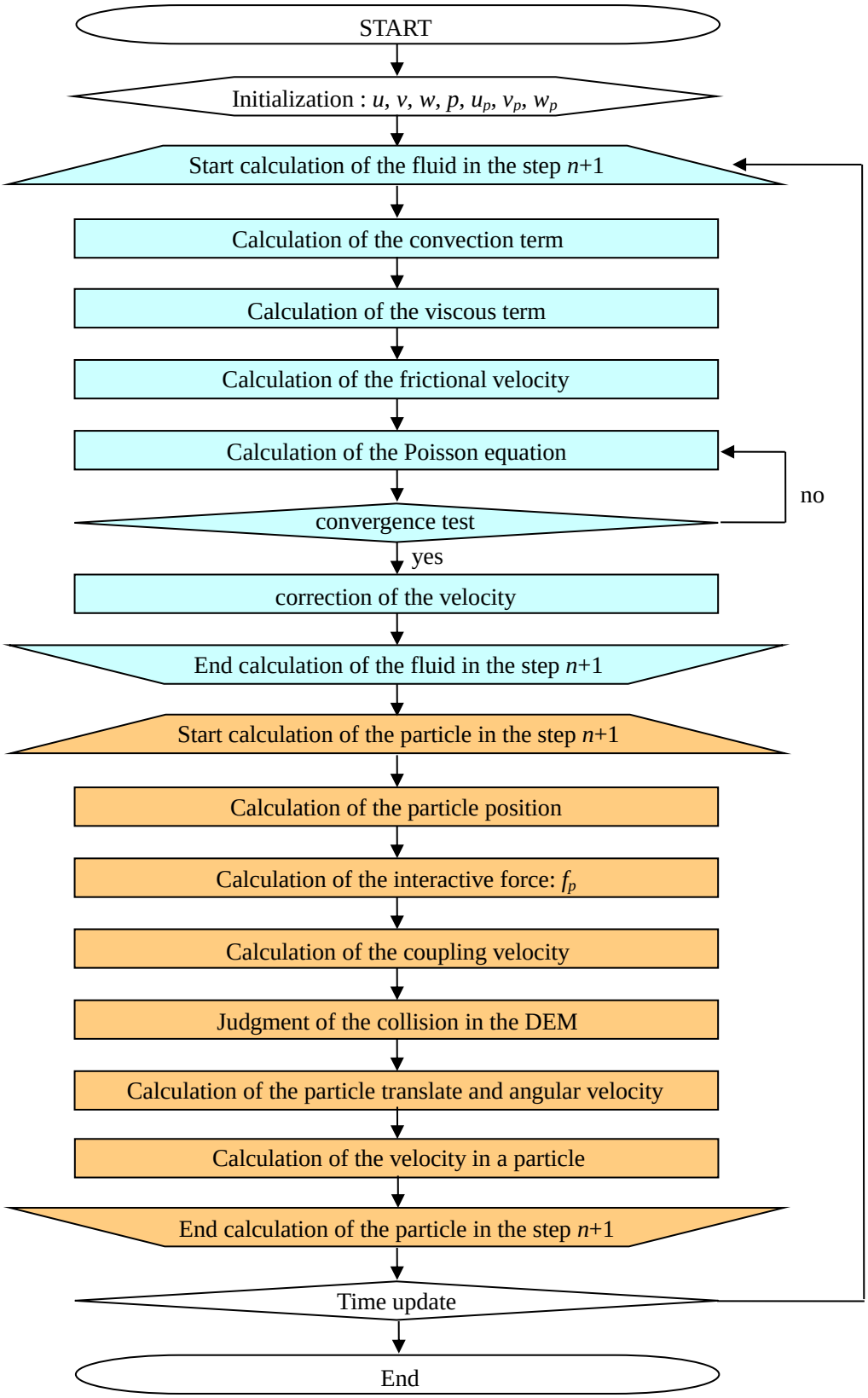

Fig. 2.6 Flowchart of the calculation

Chapter 3 **Benchmarking of IBM and drag force calculation on monodisperse spheres**

In the previous chapter, the methodology of IBM-DEM simulation is given. In this chapter, using Immersed Boundary Method, direct numerical simulations are made for the fluid flow through fixed monodisperse spheres. The objectives of this chapter are twofold: first is to make benchmarking and grid independency studies for IBM and simulation code and second is to propose drag correlation and study underlying physics. The drag correlation proposed in this chapter is useful for performing Eulerian-Eulerian and Eulerian-Lagrangian mesoscopic simulations. The simulations results and the drag correlation are valid for solid volume fractions from 0.05 to 0.5 and Reynolds number based on superficial velocity from 0.01 to 1000. The sequence of this chapter is: In Section 3.1, introduction and modeling approaches for the flows is given. In Section 3.2, literature review and motivation of the present research is given. It is followed by simulation setup in Section 3.3, results and their discussions in Section 3.4, curve fitting in Section 3.5 and the physics of the proposed relation in Section 3.6.

3.1 Introduction

In either Eulerian-Eulerian or Eulerian-Lagrangian mesoscopic approaches, flow domain is divided into computational grid for fluid flow calculations. The size of grid cell in these approaches is smaller than the mesoscopic structures like bubbles or clusters, but larger than the particle diameter. For accounting fluid-particle drag, Saffman lift force, history force, particle phase stresses and fluid phase stresses; one has to rely on various constitutive relations. Among all these forces, the fluid-particle drag is particularly important. The drag correlation can be obtained from theory, experimentation or direct numerical simulations (DNS). The details of previous researches in the respective area are given in the next section. Among them, DNS is one of the most promising areas. DNS gives better control of setup like particle size, shape without any requirement of closure relations. Furthermore, DNS gives better insight and understanding of the underlying physics. Thus DNS is used to propose the drag correlation in the present thesis.

3.2 Literature review

The drag force is the primary force to suspend and transport particles and has a significant influence on the results. For example, Benyahia[30], Gomez and Milioli[31], Heynderickx et al.[32] and Wang et al.[33] compared solid volume fraction variations in the riser of circulating fluidized bed. They observed that the drag laws based on empirical relations give more homogenous structures in comparison with experiments. Du et al.[34] compared voidage, particle velocity profiles and solid flow patterns by different drag relations in spouted beds. They observed that different drag relations change the spout shape profiles in spouted bed. Bokkers et al.[35] analyzed the effect of drag law in bubble formation and Leboreiro et al.[36] simulated segregation in a fluidized bed.

In literature, research for obtaining the drag correlations can be classified into three categories: theoretical, experimental and numerical simulations. Theoretically, there is little information available for drag force on particles and particle clouds. Most of the studies are limited to low Reynolds number (*Re*) and solid volume fractions (φ) which are usually used in literature for benchmarking simulation codes rather than for actual applications. Some of the examples of theoretical works are the work of Hashimoto[37], Sangani and Acrivos[38], Kim and Russel[39] and Goldstein[40].

Experimentally, some empirical relations are obtained by measurements of pressure drop in packed beds and calculation of average settling velocity in sedimentations. For example, Ergun[41] proposed a relation for pressure drop in packed bed based on his experiments, Richardson and Zaki[42] proposed a drag relation by calculation of hindered settling velocity at different solid volume fractions. Wen and Yu[43] also conducted a series of fluidization experiments and proposed a drag relation. Based on these empirical relations some modifications can also be found in literature. For example, one of the most widely used relations in chemical engineering is the relation proposed by Gidaspow[44]. He combined Ergun[41] and Wen and Yu[43] relation. He suggested the use of Ergun[41] relation for φ>0.2 and Wen and Yu[43] relation for φ<0.2. One of the shortcoming of this relation is at φ=0.2, there is a discontinuity in the calculation of drag force and this discontinuity increases with the Reynolds number. Di Felice[45] suggested that the exponent in Wen and Yu[43] equation should not be constant but a function of Reynolds number. Syamlal et al.[46] proposed their drag relation by modifying the terminal velocity correlations of Richardson and Zaki[42].

In numerical simulations, some of the early works for the calculation of drag force is in porous media and cylinders by Koch and Ladd[47], Andrade et al.[48] and Rojas and Koplik[49]. Later, three dimensional simulations are performed by Hill et al.[12,13] for drag force calculation for ordered and random arrangements of mono-disperse spheres for Reynolds number up to 100. Van der Hoef et al.[50] extended the work for poly-disperse spheres and Stokes flow condition. Beetstra et al.[14] simulated flow through poly-disperse spheres for Reynolds number up to 1000. Yin and Sundaresan[51,52] and Holloway et al.[53] performed simulations for Stokes and moderate Reynolds number for poly-disperse spheres with relative motion. All these simulations are performed using SUSP3D code based on lattice Boltzmann method (LBM) developed by Ladd[19,20]. Recently Tenneti et al.[15] proposed a new drag relation using IBM with much refined grid resolution up to *Re*=300. Their work raised number of controversies in the drag relation proposed by LBM. For example: Their proposed relation showed large deviations from the relation proposed by Beetstra et al.[14] (about 37% over-estimation at *Re*=300). Furthermore, they also observed that the simulation setup used by Holloway et al.[53] do not satisfy the Galilean invariance of particles and may result an error of about 10%. So the conclusion is: In literature there is still ambiguity in the development of drag relation even for mono-disperse spheres by direct numerical simulation and further investigations are possible. The innovative ideas which will be proposed in this chapter are: (1) the drag relation for extended range of Reynolds number and solid volume fractions and (2) the explanation of physics behind the difference of average drag force for low and high solid volume fractions. This study can also be used for benchmarking the ambiguity of the simulation results of Beetstra et al.[14] as pointed out by Tenneti et al.[15] for extended range of Reynolds number. Because of the frequent use of some of the references in this chapter from now on we will use HEL for Hill et al.[12,13], BEL for Beetstra et al.[14] and TEL for Tenneti et al.[15]

3.3 Simulation setup

The cubic computational domain with length L in each side is discretized with regular Cartesian grid. For making random assemblies, the particles configurations are obtained by elastic collisions (in the absence of ambient fluid) of spheres from regular arrangements. The solid volume fraction (φ) is defined by Eq. (3.1). The Reynolds number (Re) used in this chapter is based on the superficial velocity (U_{sp}) which is the

product of magnitude of average slip velocity between the solid and gas (u) and void fraction $(1-\varphi)$ given by Eq. (3.2).

$$\varphi = \frac{n_p V_p}{V} \tag{3.1}$$

$$Re = \frac{U_{sp} d_p}{\nu} \tag{3.2}$$

$$U_{sp} = (1-\varphi)u \tag{3.3}$$

where n_p is the number of particles in the domain, V_p is the volume of a single particle and V is the volume of computational domain. The average drag force (F_d) is calculated by averaging of drag force over all particles in the domain.

In the limit of infinite dilution and when inertial effects can be neglected, the drag force takes the Stokes form:

$$F_s = 3\pi\mu d_p U_{sp} \tag{3.4}$$

where μ is the viscosity and F_s is the Stokes drag. For convenience and to get rid of small values, the drag force is made dimensionless by Stokes-Einstein drag.

$$\hat{F} = \frac{F_d}{3\pi\mu d_p U_{sp}} \tag{3.5}$$

The range of solid volume fraction and Reynolds number analyzed in the current simulation are $\varphi \cong$ 0.05, 0.1, 0.2, 0.3, 0.4 and 0.5; *Re*=0.01, 10, 50, 100, 200, 400, 600, 800 and 1000 respectively. The randomly arranged particles under no relative motion with respect to each other are forced to move with the same constant velocity (v_p) without any gravity effects. This is the Galilean invariant of fixed particles. The reason for choosing moving particles in comparison with fixed particles is due to the no-slip boundary condition imposed by IBM proposed by Kajishima et al.[26]. As mentioned in Subsection 2.1.2, in IBM the effects of solid particles on fluid are imposed by modifying the computational grid both inside and at the surface of particles. In case of fixed particles, the modification of fluid grid at the same surface grid points of

particles result in overestimation of drag force. However for moving particles this effect is reduced resulting in more reliable calculation of drag force. The motion of particles increases the average fluid velocity and associated volume flow rate in the direction of particles motion due to no slip boundary condition at particle surface. At every time step this increase in volume flow rate is calculated. Then a negative volume flow rate is applied at every time instant to counter balance the increase in volume flow rate due to motion of particles. This makes the average fluid velocity in the domain to about zero (For example in the case of average particle velocity of O(10) the average fluid velocity in the domain was $O(10^{-4})$). It follows from this setup that the superficial velocity is equal to the particle velocity. Periodic boundary condition is used in all directions. All the simulations are carried out till quasi-steady state is obtained i.e. the fluctuations in the calculation of average drag force on spheres become reasonably small ($\pm 1.8\%$ of quasi-steady state average drag force).

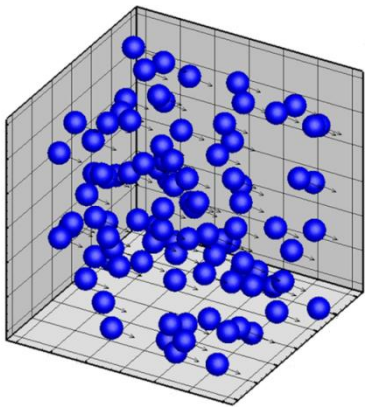

Fig. 3.1 Simulation Setup

Fixed arrangements of particles give better control over the simulation setup and thus is a good example for the checking the code. Later, the grid-independent and reliable setup is used for studying the free settling suspension. It is also to be noted that similar type of setup was used by BEL. HEL kept the particles fixed and allow the fluid to flow by applying pressure as a uniform body force and calculated the average particle Reynolds number. This kind of setup results in Reynolds number as a variable which need to be calculated, thus resulting in lesser control over Reynolds number selection. TEL also used fixed particles but rather than applying the body force they applied constant volume flow rate at a given Reynolds number. The simulation setup of BEL and TEL gives much better control over the flow Reynolds number.

3.4 Selection of parameters

In order for the drag correlation and results in the later chapters to be reliable, the parameters which are affecting the simulations are carefully studied and discussed in the next sub-sections.

3.4.1 Ensemble averaging of simulation results

In order to get statistically invariant results, ensemble averaging is performed for five independent random particle arrangements. Ensemble averaged drag force (F) is later used for curve-fitting.

$$F = \frac{\hat{F}}{5} \tag{3.6}$$

where $\hat{F}$ is the summation of drag force for five independent random particle arrangements. Relative standard deviation (R_{SD}) is used for calculating the difference of values between different particle arrangements which is given by:

$$R_{SD} = \frac{\text{Standard Deviation of data}}{\text{Average of data}} \times 100 \tag{3.7}$$

A lower value of R_{SD} indicates a lower scatter in data about the average and vice versa. The R_{SD} of simulation results for different φ and Re studied is shown in Fig. 3.2. It can be seen from Fig. 3.2 that R_{SD}'s in simulations are less than 7% which shows simulation results to have small scatter about the average value.

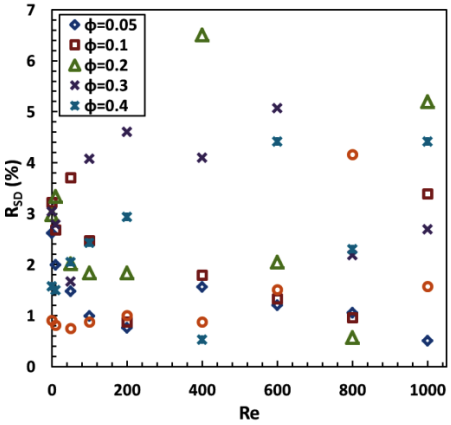

Fig. 3.2 Relative standard deviation of F on spheres from five independent random assemblies of particles at Re=0.01, 10, 50, 100, 200, 400, 600, 800, 1000

3.4.2 Effect of domain size

Another parameter which may affect the simulation results is the domain size. Small domain leads to less reliable results because of averaging over smaller number of particles and large interactions between periodic images. But computational time increases with L^3 with the increase of domain size L. Test cases for L/d_p=5, 10, 15 at $d_p/\Delta x$=24 under the conditions of φ=0.05 and 0.4 at Re=0.01, 100, 600 and 1000. Fig. 3.3 shows R_{SD} for these test cases. It is observed that the value of R_{SD} for all these test cases is either comparable or about the same as observed in ensemble averaging. In this study, L/d_p=10 for $\varphi \leq 0.1$ and L/d_p=5 for φ>0.1 is used for keeping reasonable number of particles in the computational domain.

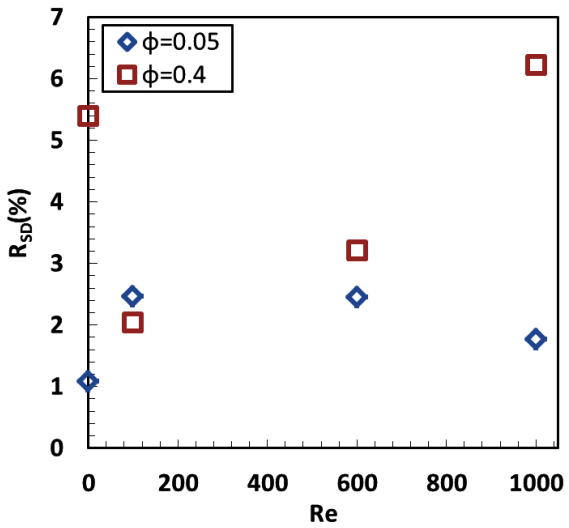

Fig. 3.3 Relative standard deviation of F on spheres for L/d_p=5, 10 and 15 at $d_p/\Delta x$=24 for particles at Re=0.01, 100, 600 and 1000

3.4.3 Effect of flow direction

HEL, in his simulations for regular arrangements of particles for non-Stokes regime in a fully periodic domain, observed that the direction of fluid flow relative to particles affects the drag force calculation. For random arrangement of particles, direction in which the particles move relative to fluid also affect the drag force especially for φ=0.05 and $Re \geqq 100$. Particle motion along the axis directions resulted in reduced drag force on the spheres (e.g. particle motion along one of the axis at φ=0.05 and Re=1000 resulted in about 9% lesser value than the average obtained from the other directions)

because of the interactions of spheres with the wakes of their own periodic images. At higher solid volume fraction the downstream wakes are diffused among particles and this effect becomes less important. This effect was also observed in a similar problem in the direct numerical simulation of free settling particles in fully periodic domain by Yin and Koch[17].

Based on the foregoing discussion, particle motion at an angle of about 10 degrees from the axis direction is used in the present simulations. This deviation angle in particle motion enlarges the distance between a particle and its own periodic image in the moving direction about six times of the length of one of side of computational domain. Thus in all simulations, the deviation angle 10 degrees between particle motion and the axis of periodic domain is used.

3.4.4 Effect of grid resolution

Selection of proper grid size is very important to resolve the microscopic fluid flow around particles in direct numerical simulations. In the simulation Reynolds number up to 1000 is investigated which is far beyond the laminar region[1]. Furthermore, in simulations more than one sphere is used; so the inter-particle distance between spheres is also important. The principal objective in this subsection is to obtain the grid converged solution by resolving accurately the flow field around the particles. Thus to ensure grid independent results, two test cases for solid volume fractions i.e. φ=0.05 and 0.4 and for each φ analyzed four Reynolds number i.e. *Re*=0.01, 100, 600 and 1000. For each Reynolds number the grid resolution is increased in steps of eight grid points per particle diameter i.e. if the initial studied $d_p/\Delta x$ is 8 then the second refined $d_p/\Delta x$ is going to be 16 and so on. The grid resolution kept increasing until the percentage difference between two successive grid sizes becomes less that 2%. The reason for this smaller value of percentage difference is to be more accurate and reliable. The percentage difference is defined by:

$$\mathrm{E}_r\% = \frac{\acute{F} - F^*}{\acute{F}} \times 100 \tag{3.8}$$

where $\acute{F}$ and F^* is the average drag force on less and more refined grids respectively. The grid-independent results for φ=0.05 is later used for φ=0.05 and 0.1, φ=0.4 is used for φ=0.2, 0.3, 0.4 and 0.5.

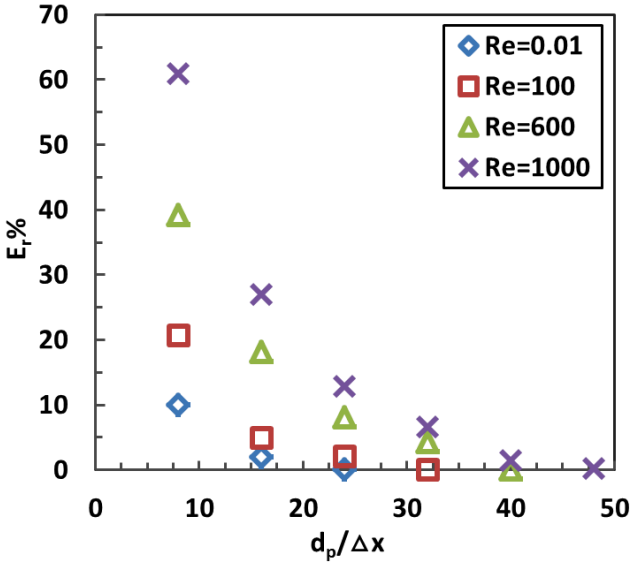

(a) φ=0.05

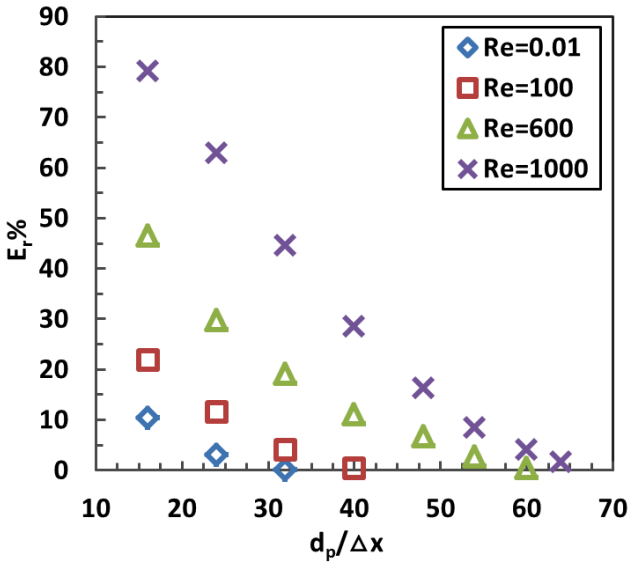

(b) φ=0.4

Fig. 3.4 $E_{r\%}$ of of $\acute{F}$ from F^*

3.5 Results

In this section, benchmarking for the calculation of average drag force for regular and random arrangement of particles, curve fitting of simulation data for randomly arranged particles, drag correlation and the underlying physics for the drag relation is given.

3.5.1 Drag force for regular arrangement of particles

The reason for simulations of regular arrangements (e.g. face centered cubic, simple cubic) of particles in periodic domains is: it gives an idea about the flow structures and drag force in packed beds. Moreover in literature there are various analytical and numerical results available for benchmarking. For regular arrangements of particles constant volume flow is applied and particles are kept fixed.

For Stokes flow regime (i.e. $Re \leq 1$) there are various theoretical and simulation results available. The relation of Sangani and Acrivos[38] and the results of HEL, Zick and Homsy[54] and TEL is used for comparison. The mathematical relation of Sangani and Acrivos[38] for simple cubic arrangement of particles is given by:

$$F = 1 - 1.7601\varphi^{\frac{1}{3}} + \varphi - 1.5593\varphi^{2} + 3.9799\varphi^{\frac{8}{3}} - 3.0734\varphi^{\frac{10}{3}} + O(\varphi^{\frac{11}{3}}) \tag{3.9}$$

$d_p/\Delta x$ for simple cubic arrangements varies from 16 to 32 for φ=0.05 to 0.523. For face centered cubic arrangements, $d_p/\Delta x$ varies from 24 to 80 for φ=0.05 to 0.653. Fig. 3.5 shows the variation of F with solid volume fractions. The results of Zick and Homsy (mentioned as Zick in Fig, 3.5)[54] and TEL showed quantitative agreement with the current simulation results. Moreover, reasonable qualitative agreement is observed between the current simulation results and the results of HEL and the theoretical relation of Sangani and Acrivos[38].

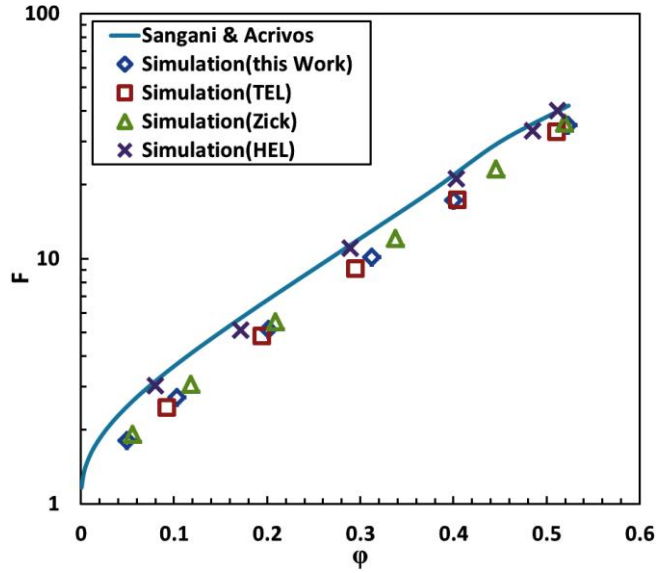

(a)

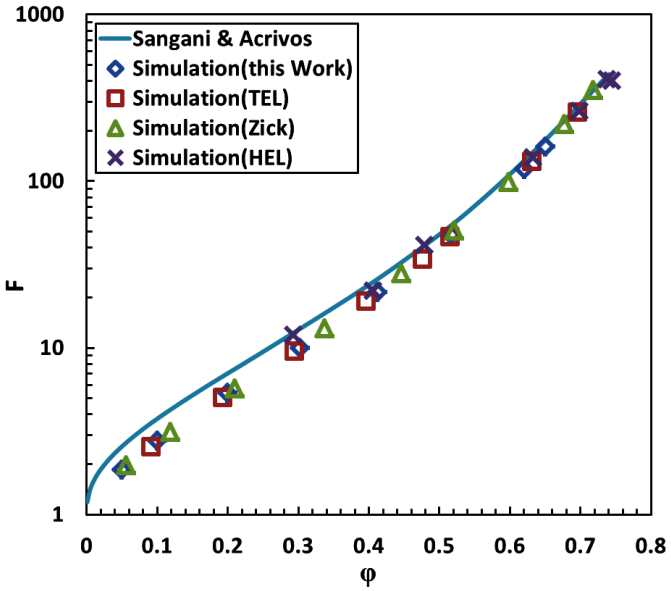

(b)

Fig. 3.5 Variation of *F* on spheres with solid volume fraction in Stokes flow regime for (a) Simple Cubic (b) Face Centered cubic arrangement of spheres.

In moderate Reynolds number, the inertial effects of fluid become important. The results are compared with the simulation results of TEL because of lack of available theoretical studies. Fig. 3.6 shows the variation of *F* with Reynolds number and for different solid volume fractions. Current simulation results showed good quantitative agreement with the results of TEL.

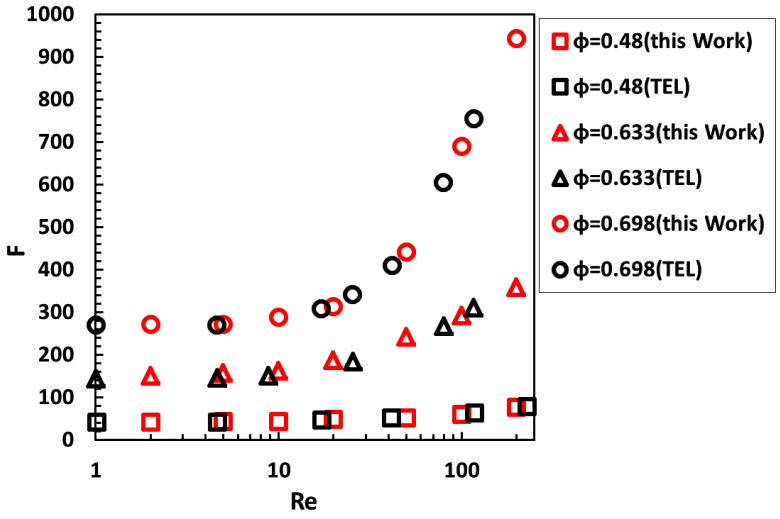

(a)

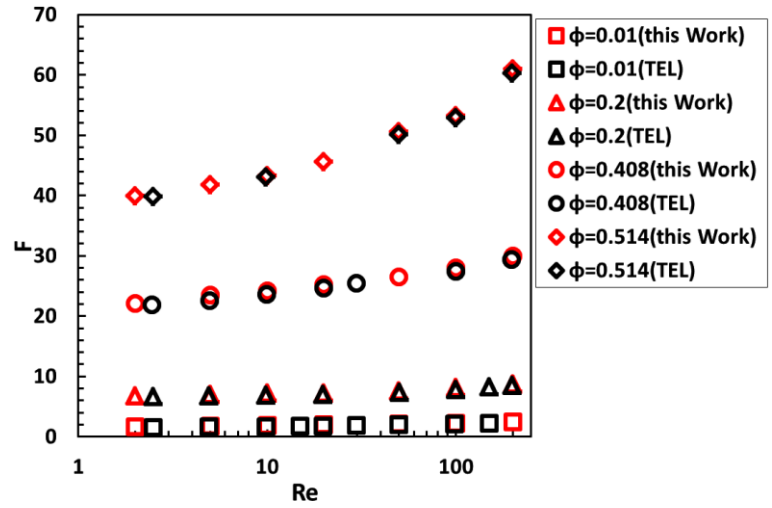

(b)

Fig. 3.6 Variation of *F* on spheres with Reynolds number for various solid volume fractions for (a) Simple Cubic (b) Face Centered cubic arrangement of spheres

3.5.2 Drag force for random arrangements of particles

For Stokes flow and random arrangement of particles, the relation of Koch and Sangani[55] and simulation results of Ladd[56], Van der Hoef et al.[50] and HEL are used for comparison. The mathematical relation of Koch and Sangani[55] is given by.

$$F = \begin{cases} \dfrac{(1+\frac{3}{\sqrt{2}}\sqrt{\varphi}+\frac{135}{64}\varphi\ln\varphi+16.14\varphi}{1+0.681\varphi-8.48\varphi^2+8.16\varphi^3} & (\varphi<0.4) \\ \dfrac{10\varphi}{(1-\varphi)} & (\varphi>0.4) \end{cases} \tag{3.10}$$

Fig. 3.7 shows the variation of F with solid volume fraction. It can be seen that there is good agreement between the present simulation results and the results of literature.

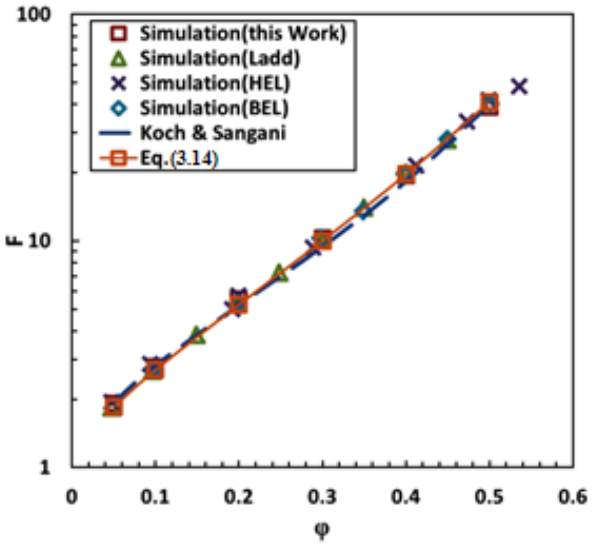

Fig. 3.7 Variation of F on spheres with solid volume fraction; in Stokes flow regime for random arrangement of spheres

In Fig. 3.8, simulation data (symbols) for the studied range of solid volume fraction and Reynolds number is given. The error bars are scatter in the data. For comparison of average drag force on particles, the simulation results of BEL, HEL and TEL is used in Fig. 3.8. The range of solid volume fraction and Reynolds number studied by these researchers are given in the Table 3.1.

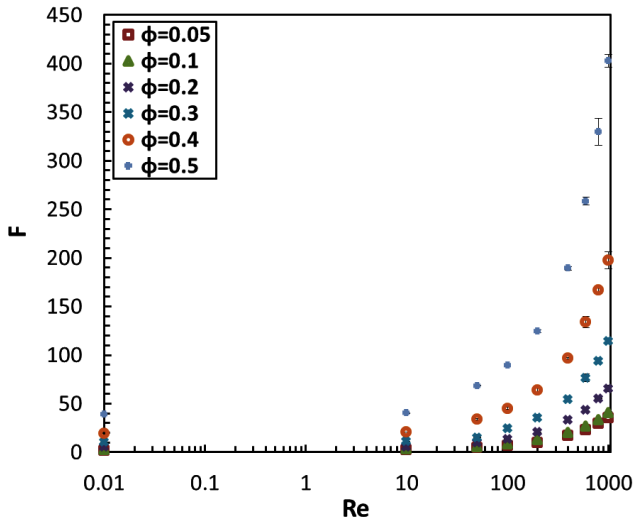

Fig. 3.8 Variation of *F* on monodisperse spheres with Reynolds number for various solid volume fractions for random arrangement of spheres. The error bars in the graph are the scatter in data due to the different particle arrangements.

Table 3.1 Range of solid volume fraction and Reynolds number studied in literature by other researchers

	Re	*φ*
Beetstra et al. (2007)	≅1000	0.1, 0.2, 0.3, 0.4, 0.5, 0.6
Tenneti et al. (2011)	300	0.1, 0.2, 0.3, 0.4, 0.5
Hill et al. (2001)	≅100	≅0.1, 0.2, 0.3, 0.4, 0.5, 0.6

Simulation results showed good agreement with the results of TEL and HEL. One particular point that was also observed by TEL, is the over estimation of *F* in the simulation results of BEL. This difference increases more and more as the solid volume fraction and Reynolds number increases (for instance the value of *F* calculated by BEL for φ=0.4 and φ=0.5 at *Re*=1000 becomes more than two times the value calculated by the current simulations). The main reason for this deviation is grid resolution used by BEL. Their space resolution was not sufficient enough to resolve the fluid length scales of the problem. In all their work, constant resolution of 17.5 lattice units per particle diameter was used for $\varphi \leq 0.3$ and for $\varphi > 0.3$ averaging over two resolutions i.e. 17.5 and 25.5 is used for the calculation of *F*.

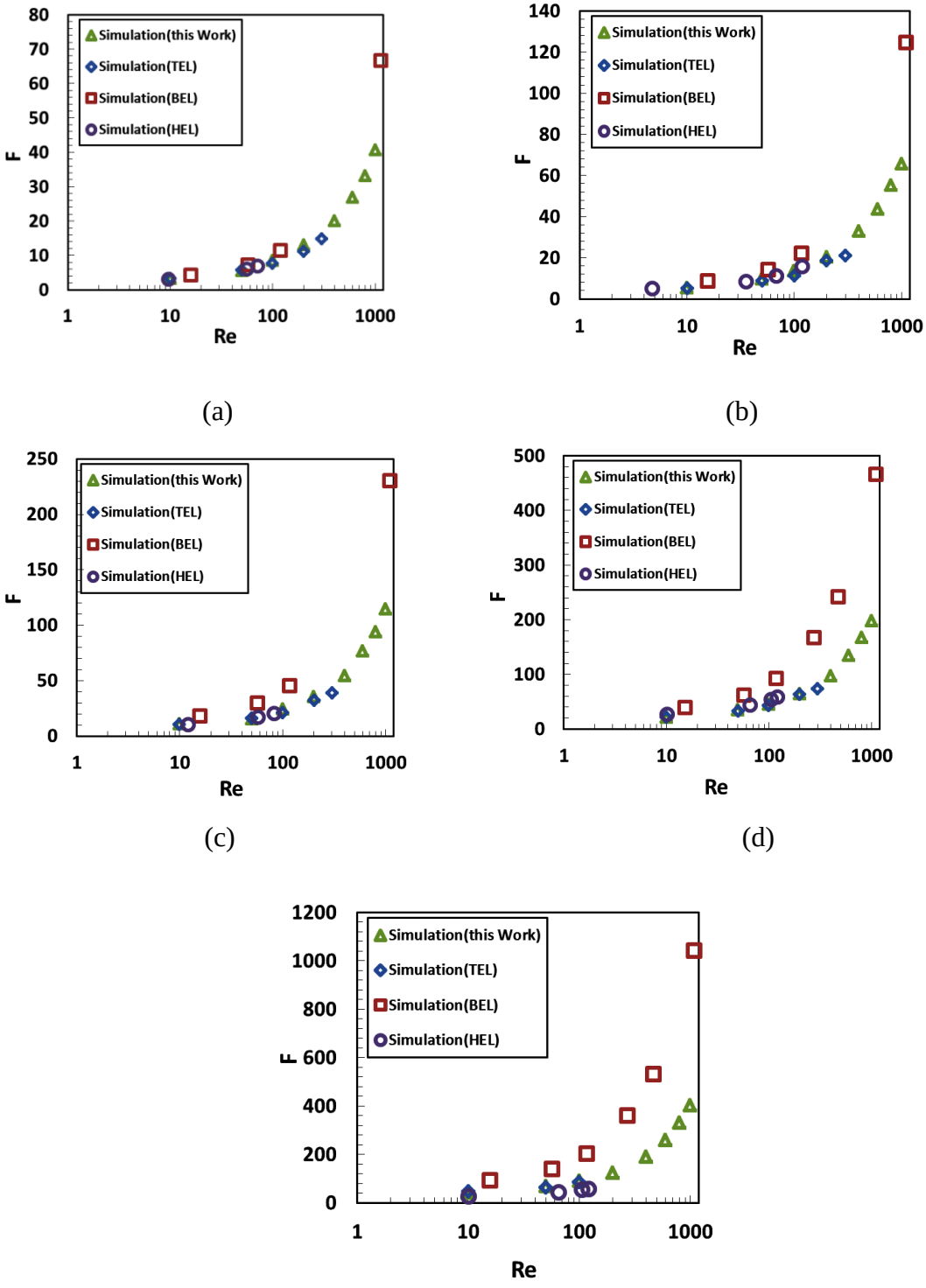

Fig. 3.9 Variation of F on spheres with Reynolds number for (a) φ=0.1 (b) φ=0.2 (c) φ=0.3 (d) φ=0.4 (e) φ=0.5

As it is already proved in grid resolution study, as the Reynolds number and solid volume increases the requirement of more refined grid also increases. It is possible that the grid used by BEL is too coarse for performing simulations up to the mentioned φ and *Re*. Another factor that may affect the simulation results of BEL is the large scattering in their results (more than 2.5 times the standard deviation). TEL and HEL take care of this point more carefully. For example HEL improved the grid from 9.6 to 33.6 lattice unit for φ=0.1 to 0.5 and TEL for *Re*>100 improved the grid from $d_p/\Delta x$=30 to 60 for φ=0.1 to 0.4. Since the grid resolution used in the present simulations are better than BEL and simulation results are in agreement with HEL and TEL thus it can be concluded that the results in the present thesis are reliable. In Subsection 3.5.5, these results are fitted to obtain the drag relation.

3.5.3 Forms of drag correlation

In literature[13,14,41,43,45], basically two classes of relations can be found for *F*. The first class of relations is given by:

$$F = F_{\mathrm{Re}\to 0} + f(\varphi)Re \tag{3.11}$$

where $F_{Re\to 0}$ is the drag force in the limit of Stokes flow and the second term is added to account for inertial force, let it to be denoted by $F_{\mathrm{int}} = f(\varphi)Re$. In the standard form, it is assumed that both $F_{\mathrm{Re}\to 0}$ and $f(\varphi)$ are the functions of only solid volume fraction and hence the variation of F_{int} with Reynolds number is linear. Ergun equation for packed beds is in this form. The variation of F_{int} with Reynolds number is plotted in Fig. 3.10. For observing the general trend, F_{int} is normalized by F_{int} at *Re*=200 for each φ. F_{int} calculated from the Ergun equation for φ=0.05 and 0.5 is also plotted for comparison. The general trend of the data for $\varphi \geqq 0.2$ is shown by small dashed black line.

It can be seen that the assumption of F_{int} to be a single linear function of Reynolds number for $10 \leq Re \leq 1000$ is not reasonable. Ergun relation based on this assumption will lead to overestimation of drag force on particles at higher Reynolds number. This over-estimation will be particularly more prominent for low solid volume fractions as can be seen in Fig. 3.9. F_{int} follows a linear law with Reynolds number up to about $100 \leq Re \leq 200$ and later the linear law decreases its angle with the Reynolds number axis. HEL proposed single linear relationship between F_{int} and Reynolds number. Since the

range of Reynolds numbers studied by HEL was less than about 100, thus their findings are correct. The reason for this change of slope will be explained in the next sub-section.

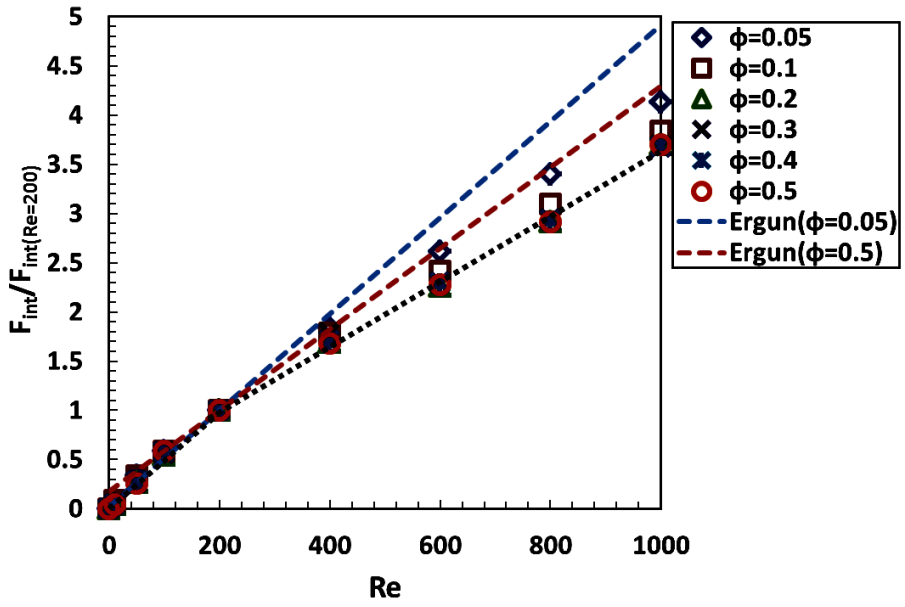

Fig. 3.10 Variation of F_{int} with Reynolds number.

In the second class of relations the expression for F can be written as the product of drag force on a single particle (F_o) and power law function of voidage. It can be written as:

$$F = F_{\text{o}}(1-\varphi)^{-\text{n}} \tag{3.12}$$

Wen and Yu[43] and Di Felice[45] relations lies in this class. Wen and Yu[43] proposed a constant value equal to 3.7 for exponent n, while Di Felice[45] proposed that n should be the function of Reynolds number. The expression for n proposed by Di Felice[45] is given by:

$$n = 3.7 - 0.65\exp\left[\frac{-(1.5-\log Re)^2}{2}\right] \tag{3.13}$$

From simulation data, F/F_{o} is calculated and for observing the general trend, it is normalized by F/F_o at Re=200 for each φ. For F_{o}, the drag correlation of Schiller and

Naumann[57] is used. It is denoted by F_{ratio} and shown in Fig. 3.11. F_{ratio} calculated from Wen and Yu[43] and Di Felice[45] is also shown in figure.

In Wen and Yu[43] relation, as *n* has a constant value thus the variation of F_{ratio} with Reynolds number remains equal to one. Di Felice[45] relation shows that initially F_{ratio} decreases with Reynolds number, obtain a minimum and then increases again for all φ. Current simulations show similar trend like Di Felice[45]. However the increase of F_{ratio} after $Re>200$ for $0.1<\varphi\leq0.5$ is relatively slower than for $\varphi\leq0.05$. The reason for this behavior of F_{ratio} will be explained in the next sub-section.

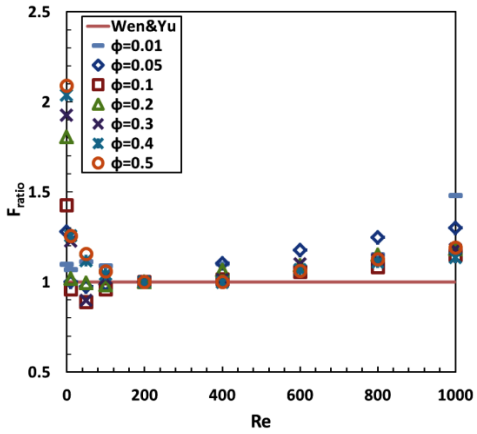

(a)

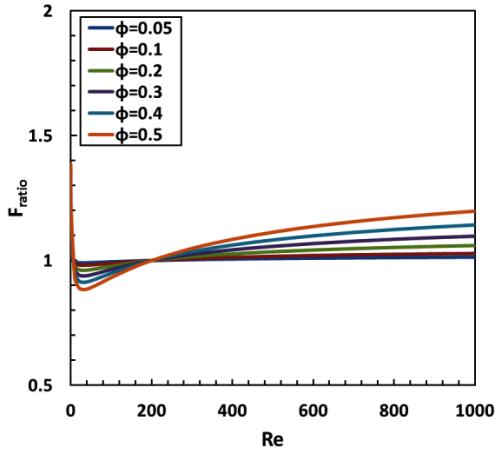

(b)

Fig. 3.11 Variation of F_{ratio} with Reynolds number (a) from simulation (b) from Di Felice[45].

3.5.4 Effects of Reynolds number on fluid flow

For understanding the effect of Reynolds number on flow and vortical structures, iso-surfaces of $\nabla^2 p$ and distribution of magnitude of vorticity are examined. The reason for the use of iso-surfaces of $\nabla^2 p$ is to identify the tube-like high vortical structures from the flow field. It was proposed by Tanaka and Kida [58] and details can be found in the mentioned reference. The basic idea is to take the divergence of the incompressible Navier-Stokes equation and thus forming the pressure Laplacian term on one side of the equation and difference of vorticity and strain rate tensor terms on the other side. In vortex tubes, vorticity dominates the strain rate. Thus positive values of iso-surfaces of $\nabla^2 p$ show the regions of vortex tubes.

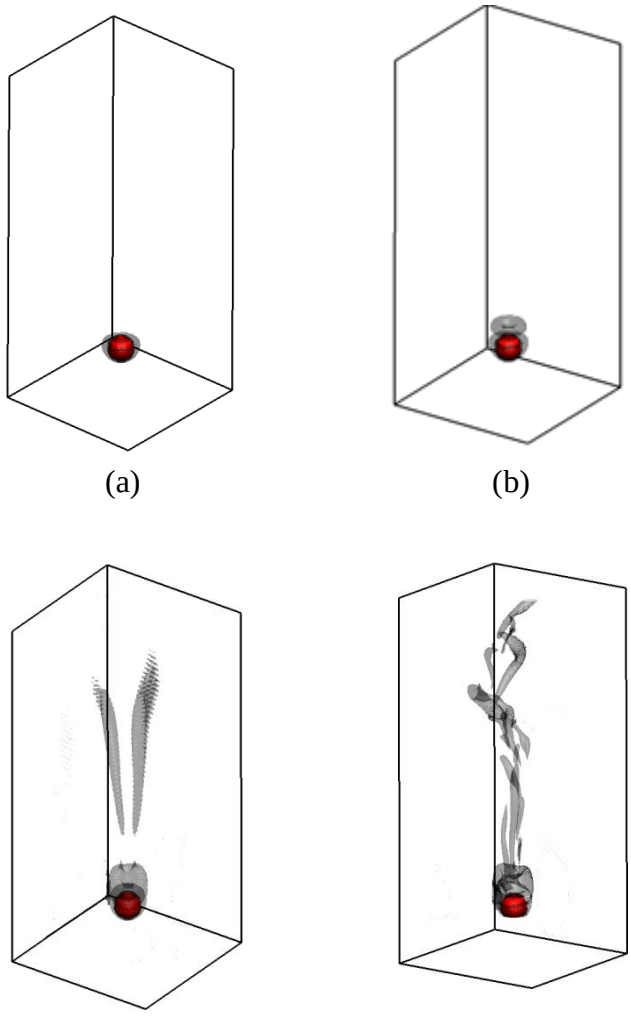

Fig. 3.12 Iso-surfaces of $\nabla^2 p$=1.5×10^6 around single sphere (a) *Re*=100 (b) *Re*=250 (b) *Re*=300 (d) *Re*=450.

The effect of Reynolds number on the flow around a single sphere is first explained as an example and later this concept is extended for group of spheres. For single sphere problem, periodic domain is taken with dimensions equal to twelve diameters of particle in the flow and six diameters in the cross-flow direction. The range of Reynolds number studied are *Re*=100, 200, 250, 300 and 450. It was observed in the previous subsection that F_{int} and F_{ratio} changes its trend in these ranges of Reynolds number. The iso-surfaces of $\nabla^2 p$=1.5×10^6 is used for visualization of fluid wakes around spheres and shown in Fig. 3.12. Flow is directed perpendicular to the horizontal plane.

It can be seen that the wakes from a single sphere remain axisymmetric and attached ring type for *Re*=100. At *Re*=250, an unattached ring is formed on the downstream side of sphere and further increase in Reynolds number enables unsteady vortex shedding as can be seen for *Re*=300 and 450. It is not shown here, but any further increase in Reynolds number alters the orientation, shape and period of vortex shedding. These vortices increase the turbulent kinetic energy and fluid velocity fluctuations both along and perpendicular to the flow direction[21,22].

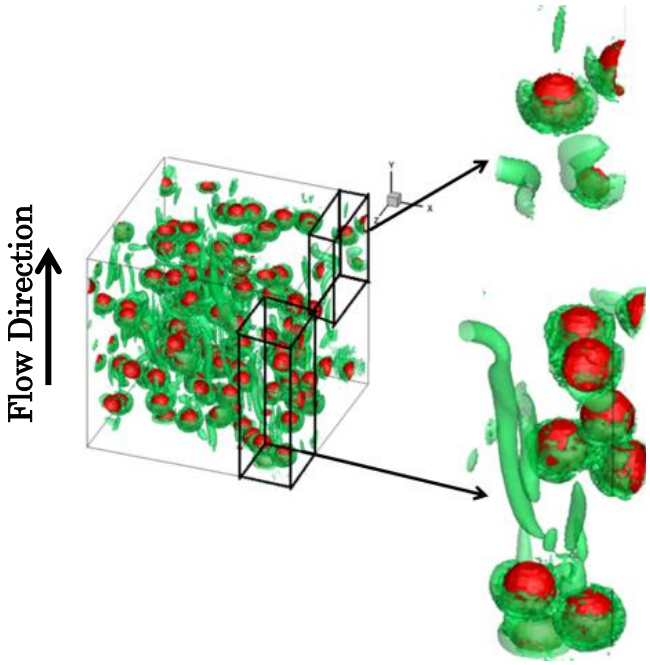

Fig. 3.13 Iso-surfaces of $\nabla^2 p$=1.5×10^6 for φ=0.05 and *Re*=200.

In randomly arranged spheres in the computational domain, particle pairs which are very close, act like a single identity. As Reynolds number is directly proportional to the sphere diameter, thus unsteady vortex shedding starts for lower ranges of Reynolds

number. For elaborating this point, the iso-surfaces of $\nabla^2 p$=1.5×10^6 for case φ=0.05 and *Re*=200 is shown in Fig. 3.13.

It can be seen in the lower enlarged view in Fig. 3.13 that unsteady vortex shedding starts around close particles even at *Re*=200. However, for single particles under identical conditions the vortex ring remains attached. The reason for the change of slope of F_{int} and F_{ratio} for 100≤*Re*≤200 in Fig. 3.10 and Fig. 3.11 is due to the entrapment of particles in these wakes. As particles in the downstream wakes, experience reduced drag, thus the increase of F_{int} with Reynolds number decreases in comparison with particles which are not in wakes. It can be seen in Fig. 3.10 and Fig. 3.11 that for $\varphi \geqq 0.2$ and *Re*>200, the trend of F_{int} and F_{ratio} is about same. Fig. 3.14and Fig. 3.15 shows the distribution of magnitude of vorticity intensity for φ=0.05 and φ=0.4 for different Reynolds number.

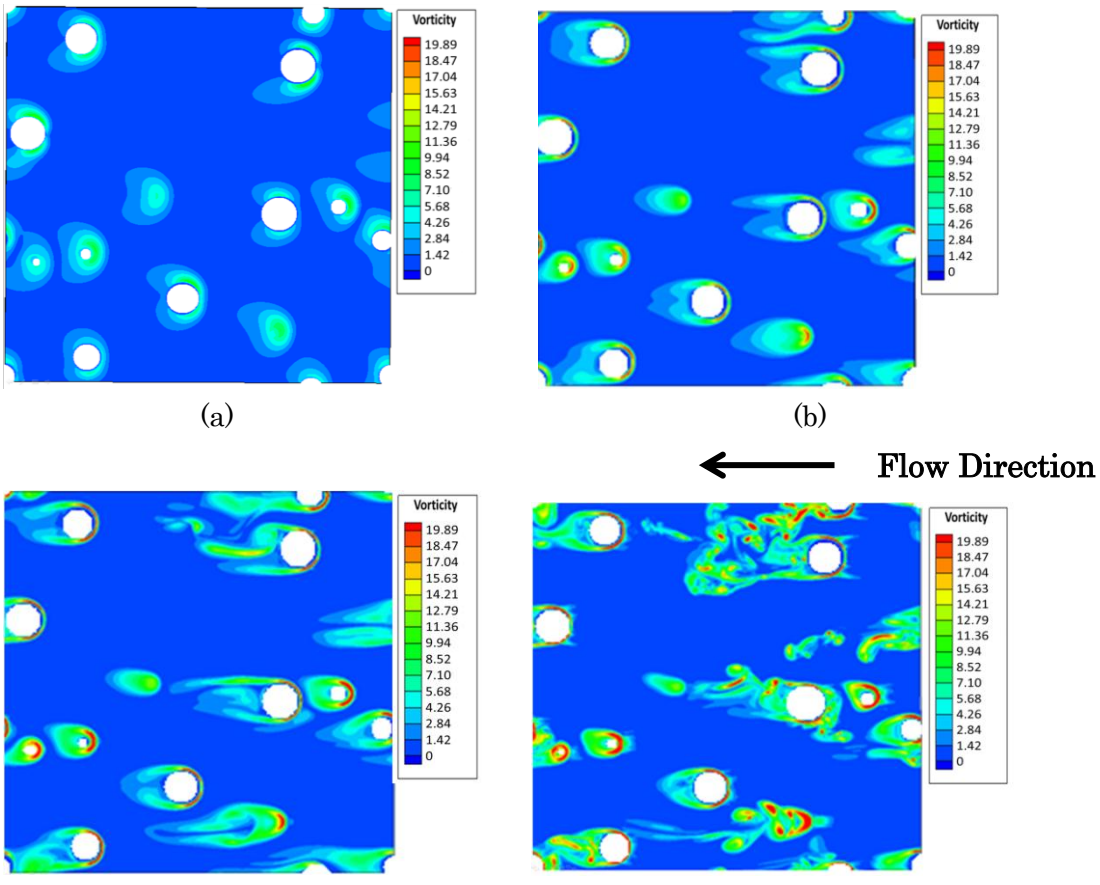

Fig. 3.14 Non-dimensional plot of vorticity intensity for φ=0.05 (a) *Re*=10 (b) *Re*=200 (c) *Re*=400 (d) *Re*=1000.

These plots are non-dimensionalized with v_{p}/d_p. For φ=0.05 because of the relatively larger inter-particle spacing wake structures develop with Reynolds number and there are regions of low or zero vorticity. However for φ=0.4 and *Re*>200 the whole computational domain is filled with high fluid shear regions. The saturation of F_{ratio} and F_{int} after $\varphi \geqq 0.2$ may be due to relatively smaller inter-particle spacing which lead to similar flow structures.

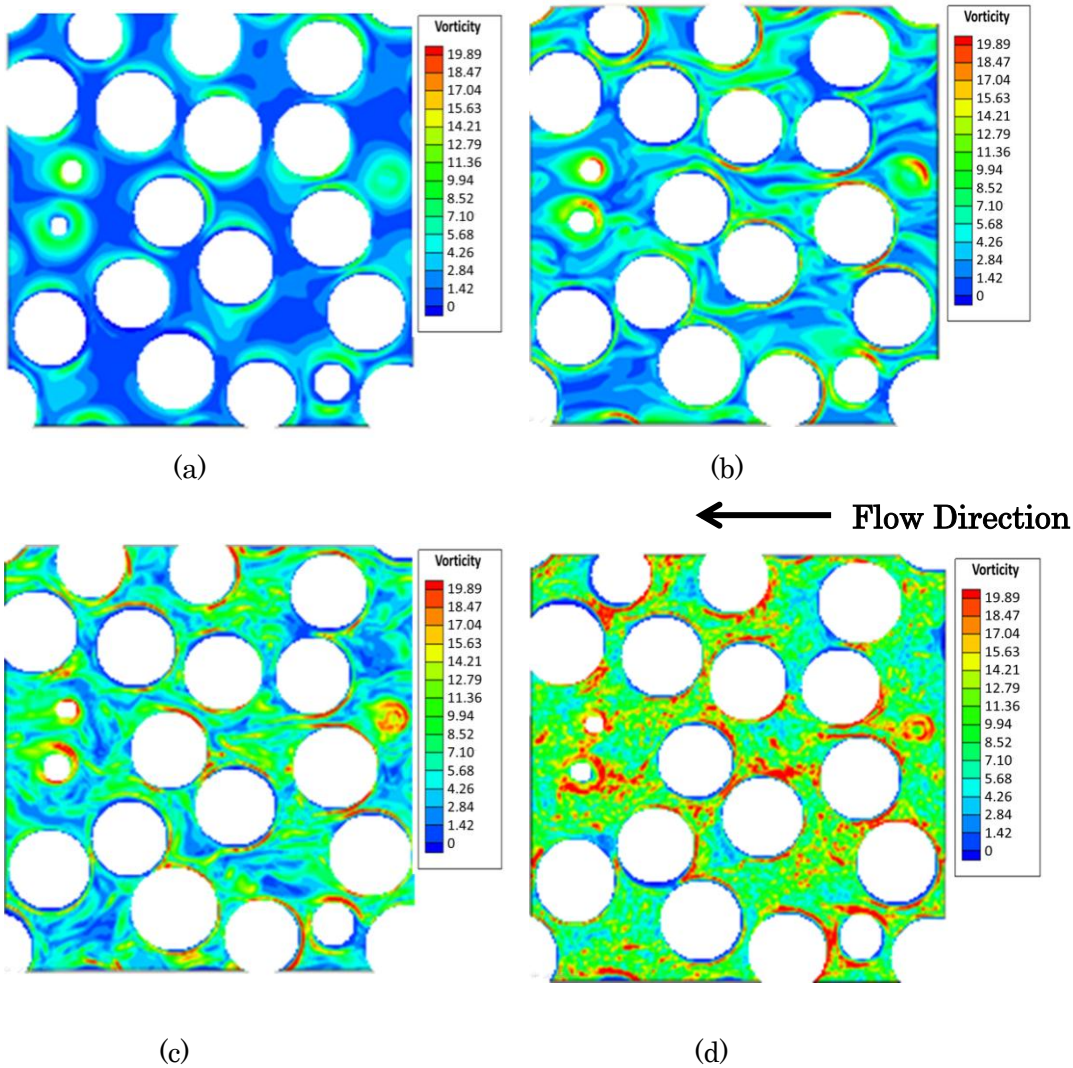

Fig. 3.15 Non-dimensional plot of vorticity intensity for φ=0.4 (a) *Re*=10 (b) *Re*=200 (c) *Re*=400 (d) *Re*=1000.

3.5.5 Curve fitting

It is observed that for curve fitting the simulation data for monodisperse spheres either drag form described before can be used. However, the literature assumptions

need to be modified. In the present thesis, the drag form of Eq. (3.11) is used. To accommodate the change of slope and obtain better fit the equation consists of two parts: one for $Re \leq 200$ and other for $200 < Re \leq 1000$.

$$F = \begin{cases} \left(\frac{10\varphi}{(1-\varphi)^3} + (1-\varphi)(1+1.5\sqrt{\varphi})\right) + \left(\frac{0.034}{(1-\varphi)^{3.7}}\right) Re & Re \leq 200 \\ \frac{10.9\varphi^{0.4}}{(1-\varphi)^{2.7}} + \left(\frac{0.024}{(1-\varphi)^{3.86}}\right) Re & 200 < Re \leq 1000 \end{cases} \quad (3.14)$$

Curve fitting is done using MATLAB. Initially the data for Stokes flow condition is fitted to obtain the first part of Eq. (3.14) i.e. $F_{\mathrm{Re}\to 0}$. The curve fitting of $F_{\mathrm{Re}\to 0}$ involves only φ. Later the inertial drag force i.e. F_{int} is obtained by subtracting the viscous drag force from the simulation data. The standard form of F_{int} in Eq. (3.11) is $f(\varphi)Re$. During curve fitting, for each studied Reynolds number, various functions for $f(\varphi)$ e.g. polynomial, power, rational functions etc. are tested to observe which function best follow the trend of the simulation data. When the best function is obtained then the multiplying factors and the exponents of φ are obtained by iterations to give the best possible fit for the simulation data.

To show goodness of fit, absolute percentage deviation ($E_{r\%}$) is plotted in Fig. 3.16. It can be seen that the curve fitted equation reasonably follows the simulation data.

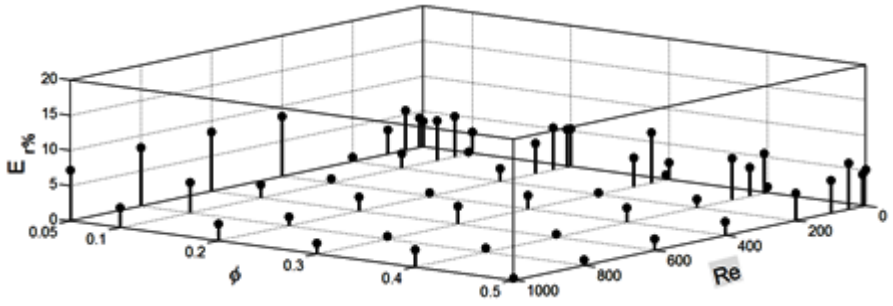

Fig. 3.16 Percentage error between simulation and Eq. (3.14)

3.6 Conclusions

In the present chapter, direct numerical simulations are used for the simulations of fluid flow through fixed monodisperse spheres. Extensive studies are done for the

parameters (e.g. domain size, gird resolution, flow direction) that can affect the results. The range of the parameters studied are φ=0.05-0.5 and *Re*=0.01-1000. The simulation results showed good agreement with most of the simulations data of literature both for regular and random arrangements of monodisperse particles for *Re*<300. For *Re*=400-1000, better predictions are made, thus the present simulation results are valid for wide range of parameters. In addition, a new drag relation for randomly arranged monodisperse system based on the results of present simulation is given by Eq. (3.14). The current drag relation can be used for closing the momentum transfer term in the mesoscopic model. The benchmarking studies done in this chapter show the reliability of the IBM, grid resolution and code used in the simulations. In later chapters, the same code and grid resolution are used for free settling particles.

Chapter 4 Particle settling for moderate Reynolds number

In the previous chapter, it was shown that the IBM and simulation code used in this thesis is capable for performing simulations for high Reynolds number and solid volume fractions. Moreover, the grid resolutions for different simulations conditions were also studied in detail in previous chapter. In this chapter, similar simulation conditions are used, the only difference is particles are allowed to move freely and the condition of zero relative motion between particles is removed. Thus the hydrodynamic interactions between particles become important and the particle microstructures are affected by their relative position with their neighbors'. The studied Reynolds number based on the terminal velocity of particle ranges from 0.1 to 50. The solid volume fraction ranges from that corresponding to a single particle in a calculation domain to 0.4. The objectives of this chapter are the calculation of average or hindered settling velocity and development of its mathematical relation and the study of velocity fluctuations during settling. The sequence of this chapter is: in Section 4.1 introduction to sedimentation and literature review is given. It is followed by simulation setup in Section 4.2, discussion of the obtained results in Section 4.3, explanation of physics in Section 4.4 and conclusions in Section 4.5.

4.1 Introduction

The transport properties of sedimenting particles play an important role in many natural and industrial processes. It uses gravitational force to separate particles from fluid streams. Some of its specific applications are separating dirt and debris from incoming raw material, crystals from their mother liquor, dust or product particles from air streams and removal of contaminants in ground water etc. The understanding of sedimentation is still challenging because of the long-range hydrodynamic interactions between particles and constantly changing particle arrangements during settling.

Reasonable data from literature is available by experiments[59-64], by theory[65,66] and numerical simulations[67-69] for low Reynolds number ($Re<0.1$). Most of the researches in this regime of Reynolds number are primarily focused on the paradox of divergence of velocity fluctuations with the increase of domain size. Theoretical studies[66] and

computer simulations[3,19,67,68] argued that in Stokes flow regime the velocity fluctuations keep on increasing with the increase in domain size. However, larger scale experiments[59-61] have found no such evidence. Recent experiments by Segre[62] answered this question that the computational domain size should be large enough to accurately capture the whirls formed in settling.

In hindered settling, moderate Reynolds regime (Re≅1-210) and high Reynolds number regime (Re>300) pose greater difficulty. In moderate and high Reynolds number regimes, wakes are formed around particles. Thus the computational grid should be fine enough to capture the flow structures. Some of the hot topics for high Reynolds number regime are the particle clustering due to turbulence for small solid volume fractions[21-23], turbulence modulation by particle clusters[70] and the effect of finite size particles on the flow structure[24].

For moderate and high Reynolds number regime the numerical simulations for particle settling are scarce. These regimes pose greater difficulty because of the requirement to resolve smaller scale flow structures. Based on the author's knowledge, only three studies are available in literature for moderate Reynolds number regime i.e. Climent and Maxey[16] and two studies by Yin and Koch[17,18]. The work of Climent and Maxey[16] is limited to $0<Re<10$ and $0.01<\varphi<0.12$ and the work of Yin and Koch[17,18] is limited to $1<Re<20$ and $0.005<\varphi<0.4$. The work of Climent and Maxey[16] was more focused on the benchmarking studies of their force coupling method code rather than explanation of new phenomenon in dilute suspensions. The studies of Yin and Koch[17,18] were more focused for dense suspensions. Moreover, they used the SUSP3D code developed by Ladd[19,20]. In SUSP3D code the surface of sphere is approximated by stair shape and effective diameter for simulation is defined based on the drag force on the cubic arrangement of monodisperse spheres for Stokes condition using the analytical solution by Hasimoto[37]. For higher Reynolds number regime according to the author's knowledge there are also three investigations in literature i.e. Kajishima and Takiguchi[21], Kajishima[21] and Doychev and Uhlmann[23]. These investigations were principally focused on particle clustering due to turbulence for very dilute suspensions (the maximum solid volume fraction studied was $\varphi\leq0.4\%$) and turbulence modulation by particle clusters.

The theme of this chapter and the next chapter is to study hindered settling for both dilute (in which two body hydrodynamic interactions are important) and dense

suspension (in which multi-body hydrodynamic interactions are important) for $Re \leq 300$. IBM uses spherical shape of particles and original particle diameter is used without any priori benchmarking studies thus the results of IBM are more reliable than the simulations done using SUSP3D code. The new concepts that are presented in this chapter are deviation of average settling velocity from standard power law of literature and it's possible explanation, study of the screening of velocity fluctuations with domain size for moderate Reynolds number and the particle structure formations.

4.2 Simulation setup

In simulations, cubic computational domain of length L in each direction is used. Similar like in previous chapter, periodic boundary condition and zero volume flow rate at every time step is used to mimic the unbounded suspension (for details about the imposition of zero volume flow rate please read Section 3.3). The initial particles configurations are random and are obtained by elastic collisions (in the absence of ambient fluid) of spheres from regular arrangements. The numbers of spheres used in the domain are taken to obtain desired solid volume fraction. The density of particles and fluid is taken to be 2500 kg/m^3 and 1000 kg/m^3 respectively. It is analogous to settling of aluminium particles in water. The diameter of particles used in simulations is 1.2 mm. The direction in which the particles settle for both single and multiple particles are taken to be away from the periodic axis i.e. X, Y and Z Cartesian directions and usually at an angle between 10-30 degrees to reduce the chances of particles to interact with their own wakes. It can be obtained by resolving the gravity components in two or three Cartesian directions. Three different initial particle distributions are studied for each case to get statistically reliable results. Furthermore all the results presented in the next section are time averaged for about 300-500 Stokes time ($t' = t\, U_s/d_p$ where t' is Stokes time, t is the actual time, U_s is the terminal velocity of single particle and d_p is the particle diameter). The studied Reynolds number are $Re \cong 0.1$, 1, 10, 20, 30, 40 and 50; solid volume fraction from single sphere to 0.4. The particle Reynolds number is controlled by changing the gravity magnitude and in this chapter it is defined as:

$$Re = \frac{U_s d_p}{\nu} \tag{4.1}$$

The parameters shown in Table 4.1 are used for DEM solver:

Table 4.1: DEM parameters

Coefficient of Restitution [-]	0.9
Normal Spring Constant [N/m]	800
Coefficient of Particle Friction [-]	0.25

η can be obtained by Eq. (2.42). The normal spring constant is set to 800N/m that is much smaller than the actual value to increase the time step. It was evaluated that the estimated collision time is much smaller than the other physical time scales in the phenomenon and the maximum deformation of particle is much smaller than the particle diameter. It is observed in some test cases that the parameters used in DEM solver negligibly affect the particle settling results.

4.3 Results

In this section benchmarking of terminal velocity of single particle, calculation of average settling velocity, velocity fluctuations and structure formation during settling are given.

4.3.1 Calculation of terminal velocity

The settling or terminal velocity (U_s) of a single particle provides the simplest case for benchmarking of free settling particles. There are plenty of literature data and mathematical relations available for terminal velocity calculation. The relations of Hartman et al.[71] for the calculation of terminal velocity in an infinite medium is used for benchmarking.

$$\log_{10}\frac{U_s d_p}{\upsilon} = P + \log_{10} R \tag{4.2}$$

$$P = \big((0.0017795C - 0.0573)C + 1.0315\big)C \ -1.26222 \tag{4.3}$$

$$R = 0.99947 + 0.01853\sin(1.848C - 3.14) \tag{4.4}$$

$$C = \log_{10} Ar \tag{4.5}$$

$$\mathrm{Ar} = \frac{\rho_f(\rho_p - \rho_f) g {d_p}^3}{\mu^2} \tag{4.6}$$

Table 4.2: Comparison of terminal velocity by simulation and (4.2)

Re	U_s(m/s) by Eq.(4.2)	U_s(m/s) by Simulation	Percentage Difference
1	0.00068	0.000683	0.4
10	0.0068	0.00671	1.3
20	0.013	0.0127	2.3
30	0.020	0.0195	2.5
40	0.0267	0.0261	2.2
50	0.033	0.0321	2.7

The deviation between the equation and the simulation is observed to be less than 2.7% for all the cases. The terminal velocity calculated by simulations is used to normalize the hindered settling velocity in the next subsection.

4.3.2 Hindered settling velocity

4.3.2.1 Effect of domain Size

For analysing the effect of domain size six cases of solid volume fractions and Reynolds number are studied:

Table 4.3: Test cases for domain sizes for different φ and Re

Re	φ	L/d_p
1	0.01	10, 25, 50
50	0.01	10, 25, 50
1	0.05	10, 20, 25
50	0.05	10, 20, 25
1	0.2	5, 10, 15
50	0.2	5, 10, 15

The averaged particle velocity showed more variation with increasing domain size for low solid volume fractions and low Reynolds number (e.g. in the case of Re=1 and φ=0.01, the percentage difference from the largest domain size decreases from 10.8%

to 3.1% for increasing L/d_p from 10 to 25 and in the case of *Re*=50 and φ=0.01, it decreases from 2.4% to 0.2% for increasing L/d_p =10 to 25). The reason for the comparatively larger variation observed in the cases of low solid volume fractions is the small number of particles to give statistically reliable results and this tendency is more remarkable for the case of low Reynolds number due to the long range hydrodynamic interactions. The domain size in any case is selected in such a way that the percentage difference between two successive domain sizes is less than 5%. For $\varphi \leq 0.01$ and for $\varphi > 0.01$, L/d_p=25 and L/d_p=10 is used respectively.

4.3.2.2 Results and curve fitting

It is well known that the mean settling velocity of uniform sized spheres is less than the terminal velocity of an isolated sphere due to the inter-particle interactions. It is also observed in literature [e.g. work of Ham and Homsy[72], Al-Naafa and Selim[73] etc.]. Experimentally, it is not easy to obtain the average particle settling velocity especially for dilute suspensions because generally in experiments the average settling velocity is measured by the motion of fluid solid interface which is difficult to track for dilute suspension. Even for the measurement of particle terminal velocity uncertainty up to 10% in the experimental results are possible (Di Felice[74]). Thus numerical simulations give more reliable results by better control over the simulation setup and particle velocity calculations.

For comparison, the power law formula of Richardson and Zaki[42] (R&Z) is used. This relation is obtained by the experimental results of R&Z and is widely used in chemical engineering applications. In this relation, hindered settling velocity is expressed in terms of the terminal velocity of a single particle and void fraction. It is given by the following equation:

$$U = \frac{V_p}{U_s} = (1-\varphi)^{n_e} \tag{4.7}$$

where n_e is the power-law exponent which depends on the terminal particle Reynolds number and V_p is the average settling velocity. The equation of n_e proposed by R&Z is:

$$n_e = \begin{cases} 4.65 & Re < 0.2 \\ 4.4Re^{-0.03} & 0.2 < \mathrm{Re} < 1 \\ 4.4Re^{-0.1} & 1 < Re < 500 \\ 2.4 & Re > 500 \end{cases} \tag{4.8}$$

Garside and Al-Dibouni[75] (G&D) proposed another equation of n_e by a single correlation given by Eq. (4.9).

$$\frac{5.1 - n_e}{n_e - 2.7} = 0.1Re^{0.9} \tag{4.9}$$

In simulations, the mean settling velocity of particles is calculated after fully developed or steady state of fluid. The time evolution of average settling velocity of particles is shown in Fig. 4.1.

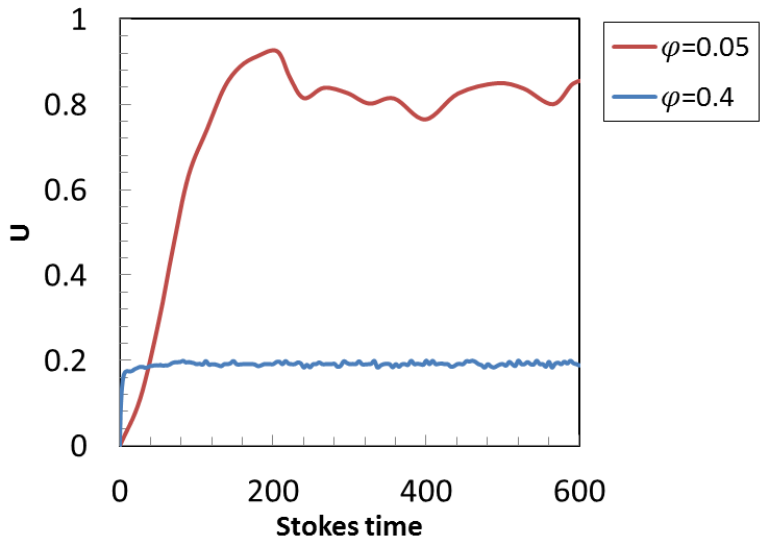

Fig. 4.1 Time evolution of average settling velocity of particles

The comparison between the simulation data and the correlation by R&Z (Eq. (4.7) and (4.8)) in shown in Fig. 4.2 and the percentage difference between them is shown in Fig. 4.3.

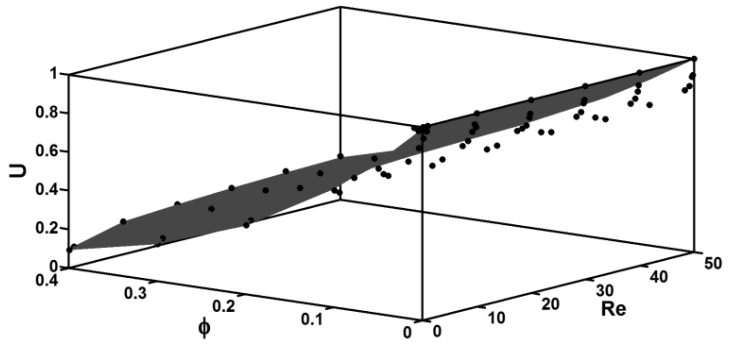

Fig. 4.2 Comparison of simulation data points (Black dots) and correlations of Eq.(4.7) and (4.8)

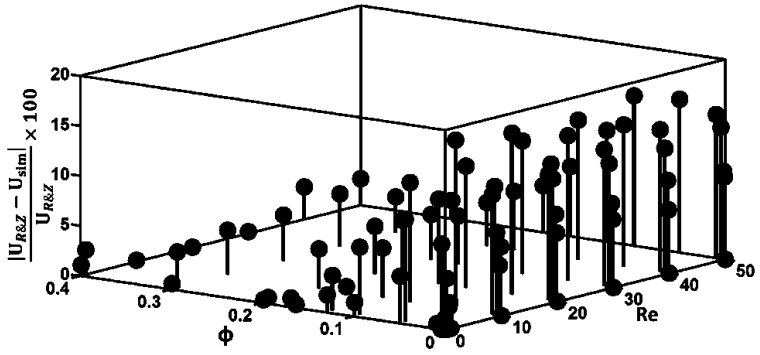

Fig. 4.3 Percentage difference of simulation data points and correlations of Eq.(4.7) and (4.8)

It can be observed that:

1. Simulation data reasonably agree with R&Z relation for low Reynolds number i.e. $Re \cong 0.1$ and all studied φ. For $Re > 0.1$, in very dilute ($\varphi \leq 0.01$) and dilute regimes ($\varphi > 0.01$ & $\varphi \leq 0.1$) the value of U by simulations is less than the prediction of R&Z and the difference keep increasing with the increase of Reynolds number (e.g. for $\varphi = 0.01$ the percentage difference between the simulation data and R&Z correlation increases from 3.6% to 14.4% with increase of Re from 0.1 to 50). Moreover for $\varphi \leq 0.01$ simulation results for U rapidly approaches the terminal velocity of single particle.
2. For dense case ($\varphi \geqq 0.2$) the simulation results are in reasonable agreement with R&Z correlation for all the range of studied Reynolds number (the max percentage difference between the simulation data and R&Z correlation in this range is 3.3% at $Re = 50$).

It will be explained later in Subsection 4.3.4 that two-body hydrodynamic interactions

dominate in dilute suspensions and multi-body hydrodynamic interactions dominate in dense suspensions. Dense suspensions have generally random particle arrangements during settling and do not support any particular particles configurations due to smaller inter-particle distances. For dilute suspensions, the two particle interactions vary with the change in the Reynolds number and contribute to different particle structures as will be explained later. The limits of Reynolds number proposed by R&Z are based on these particle structures formed in sedimentation. These particle arrangements are different at different solid volume fractions as will be explained in Subsection 4.4.3 and thus affect the hindered settling velocity. Similar behaviour of over-estimation of hindered settling velocity by R&Z was observed by the experiments of Di Felice[74] for dilute suspensions ($\varphi \leq 0.05$) and Re= 0.01-1000. The author thinks that the exponent n_e to be the function of only Reynolds number is not sufficient to describe the averaged particle velocity at different solid volume fractions. The author proposes that in the exponent besides Reynolds number there should also be a function of solid volume fraction for $\varphi > 0.01$ and a constant term for $\varphi \leq 0.01$ to accommodate the changing particle arrangements during settling. Moreover, it is also observed that the averaged particle velocity during settling for $\varphi \leq 0.01$ and $\varphi > 0.01$ are quite different and difficult to be expressed by single relation. Thus, the following relation is proposed for hindered settling velocity:

$$U = (1-\varphi)^{n_e} \tag{4.10}$$

for $\varphi \leq 0.01$

$$n_e = \begin{cases} 4.65 & Re < 0.2 \\ 4.4Re^{-0.03} + 9.348 & 0.2 \leq \mathrm{Re} \leq 1 \\ 4.4Re^{-0.1} + 15.74 & 1 < Re \leq 50 \end{cases} \tag{4.11}$$

for $0.01 < \varphi \leq 0.4$

$$n_e = \begin{cases} 4.65 & Re < 0.2 \\ 4.4Re^{-0.03} + 8.2(1-\varphi)^{26.33} & 0.2 \leq \mathrm{Re} \leq 1 \\ 4.4Re^{-0.1} + 7.75(1-\varphi)^{16.81} & 1 < Re \leq 50 \end{cases} \tag{4.12}$$

To visualize the effect of Eqs. (4.10), (4.11) and (4.12), simulation results are compared in Fig. 4.4 for Re=0.1, 1, 20 and 50.

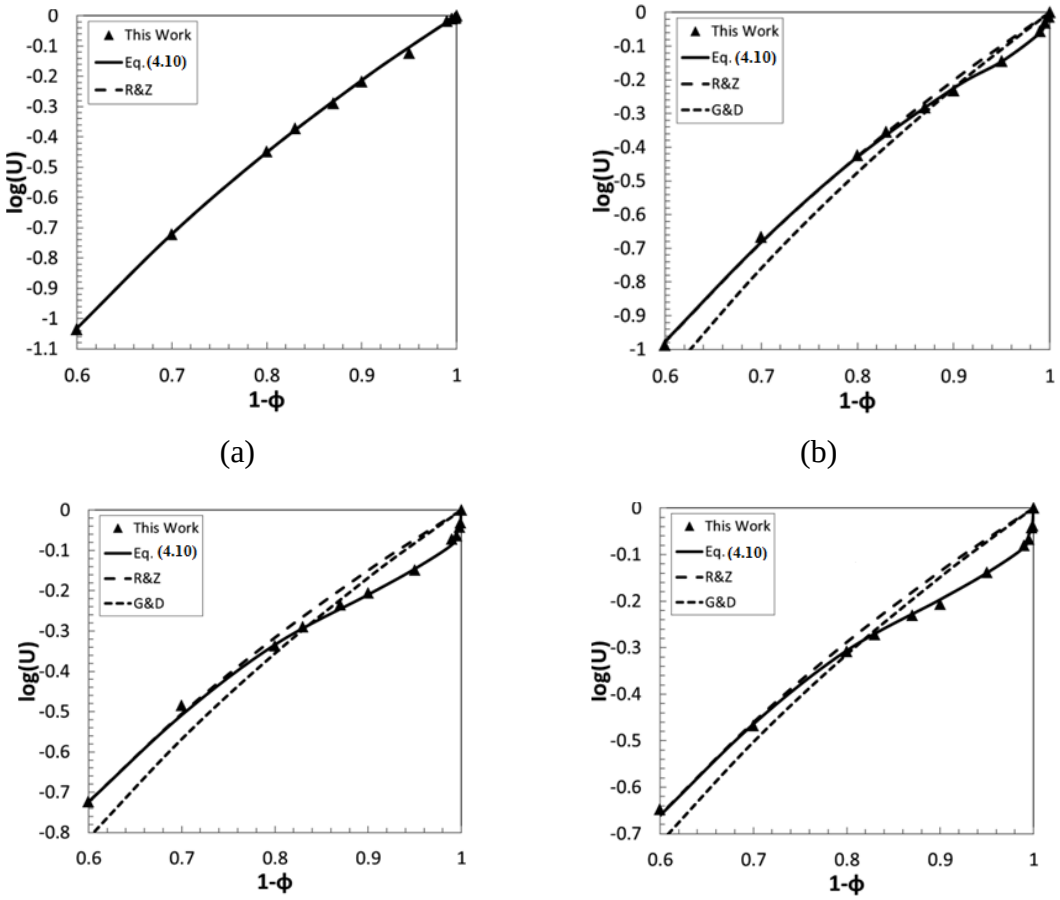

Fig. 4.4 Hindered Settling Velocity as function of (*1-φ*) (a) *Re*=0.1 (b) *Re*=1 (c) *Re*=20 (d) *Re*=50

It can be seen that Eqs. (4.10), (4.11) and (4.12) gives much better fit to the simulation data points in comparison with other relations. Quantitatively, the percentage difference between this improved correlation and the simulation data is less than 3% for all the Reynolds numbers. It can be also seen that in the dilute region of 1-φ>0.99, *U* markedly reduces with increasing φ and deviates from R&Z correlation. The same tendency is also observed in the results by Yin and Koch[17], however, the deviation from R&Z correlation with increasing φ is more gradual than the present result.

4.3.3 Velocity fluctuations

When the particles settle under gravity, all the particles are not settled with the same averaged velocity but develop some deviations and fluctuations about the mean

or average settling velocity. These deviations are called velocity fluctuations. The origin of these fluctuations is the hydrodynamic interactions between particles. These inter-particle hydrodynamic interactions are the primary source of mixing. Particle velocity fluctuations induce fluid velocity fluctuations. For low range of Reynolds number, Caflish and Luke[66] proposed that the hydrodynamic interactions among randomly distributed sedimenting particles lead to linear growth of the particle velocity fluctuations with the size of the suspension. Later numerical simulations[68,76] subject to periodic boundary conditions and low Reynolds number benchmarked the studies done by Caflish and Luke[66]. Recently, Segre[62] explained by experiments that there is a characteristic length of vortices above which the effect of domain size on velocity fluctuations becomes negligible. In the range of Oseen-wake interactions and dilute suspension; Koch[77] based on his theoretical study showed that wakes around particles should screen the velocity fluctuations with domain size. In this section, the effect of domain size on velocity fluctuations is discussed for both low and moderate Reynolds number i.e. *Re*=1, 50. In this subsection, only the results for φ=0.01 are shown for studying the velocity fluctuations and it is shown that similar trend is observed for higher solid volume fractions. For studying velocity fluctuations, variance of particle and fluid velocity is used and it is non-dimensionalized by the square of terminal velocity of single particle. The domain sizes studied for both cases are L/d_p=10, 15, 25, 35 and 50. Fig. 4.5 shows the velocity fluctuations in vertical and horizontal direction.

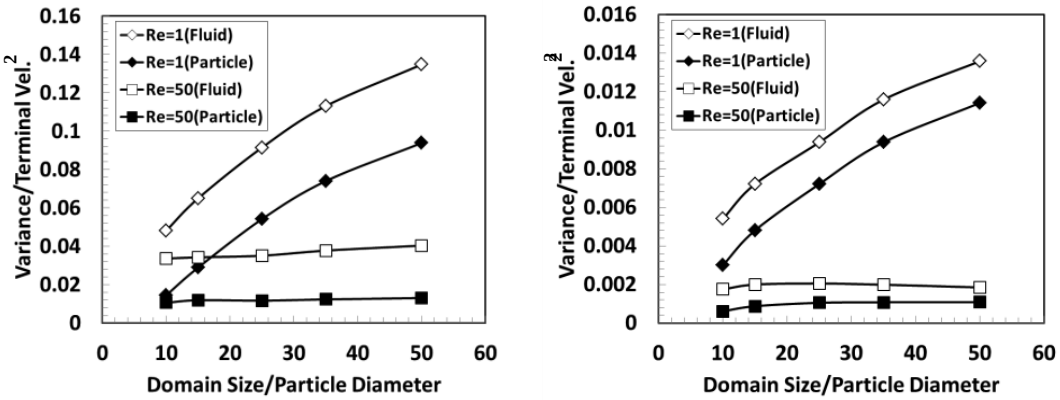

Fig. 4.5 Velocity fluctuations for φ=0.01 and *Re*=1 and 50 (a)Vertical Direction (b) Horizontal Direction.

It can be seen in Fig. 4.5 that for *Re*=1, the velocity fluctuations keep increasing with domain size. However, for *Re*=50 the increase of velocity fluctuations with domain size is much less pronounced. Moreover, comparison of vertical and horizontal velocity fluctuations indicates that anisotropy is still strong. Particle velocity fluctuations in the vertical direction is greater than the horizontal ones (about 7.5 times for *Re*=1 and 12 times for *Re*=50) indicating the influence of forcing due to gravity. Another important point is that the fluid velocity fluctuation is larger than the particle velocity fluctuation. However the variation of fluid velocity fluctuations with domain size is about parallel to the variance of particle velocity for both Reynolds number. The physical reason for this behavior of velocity fluctuations will be explained later.

To further elaborate the above mentioned point, snapshots of particle settling for different domains are shown in Figs. 4.6 and 4.7 for *Re*=1 and 50 respectively. Particles are coloured by settling velocity. The legend is non-dimensionalized by average settling velocity. Thus greater colour variations of particles in the domain show greater particle velocity fluctuations. It can be seen that for *Re*=1 the velocity fluctuations of particles is higher than for *Re*=50.

The reason for the relatively larger increase in velocity fluctuations with the domain size for Stokes flow condition is due to the larger affecting area around particles. However for moderate Reynolds number this region reduces. Thus the effect of domain size on velocity fluctuations decreases. Thus the paradox of divergence of velocity fluctuation with domain size is not valid for moderate Reynolds number.

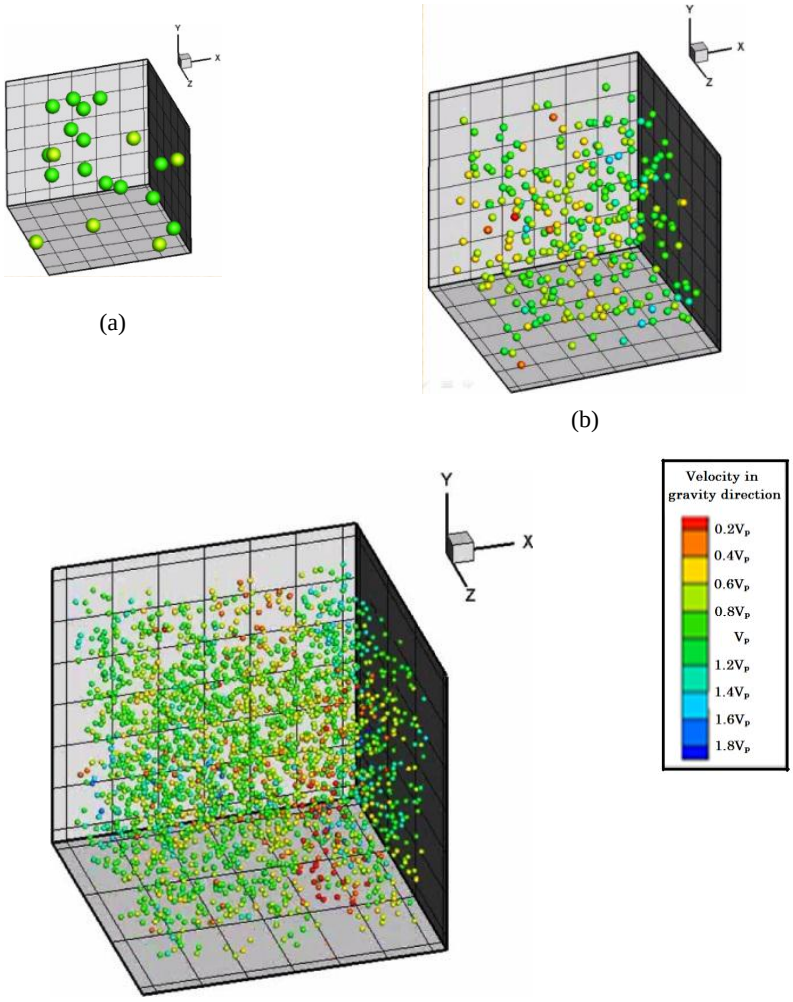

(a)

(b)

(c)

Fig. 4.6 Velocity fluctuations for φ=0.01 and *Re*=1 (a) L/d_p=10 (b) L/d_p=25 (c) L/d_p=50

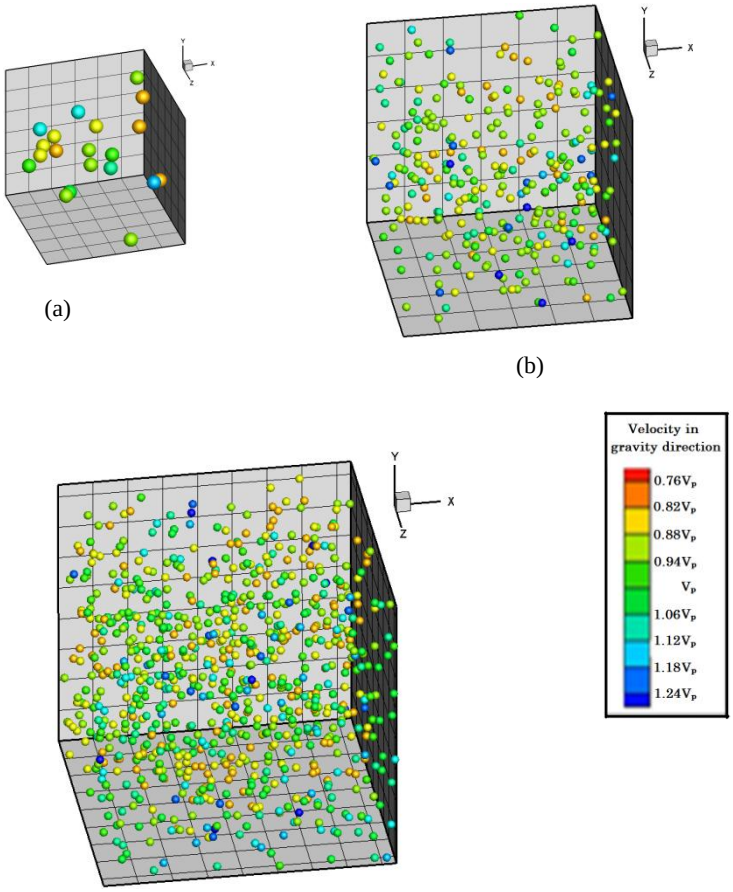

Fig. 4.7 Velocity fluctuations for φ=0.01 and *Re*=50 (a) L/d_p=10 (b) L/d_p=25 (c) L/d_p=35

4.3.4 Structure formation in suspension

In literature[67], it is evident that two particles in Stokes flow condition fall with weak but broad wakes and give rise to the long range velocity perturbations. However in the case of moderate Reynolds number, the symmetrical flow structure around the particle breaks and the wakes from the leading particle affect the downstream particle and thus leading to drafting kissing and tumbling scenario[78] (DKT). In the next subsections particle structures formed during hindered settling are discussed. It will be clear that DKT plays an important role in particle structures formed during settling and thus described in this subsection. Particle wakes are the regions of low drag for downstream particles. As the downstream particle experiences reduced drag it moves faster till it touches the leading particle which is called kissing. The approach phase of downstream particle is called drafting. Particles in the touching arrangement are

unstable and try to separate and form horizontally separated pairs. This is called tumbling. All these three phases for two particles are shown in Figs. 4.8 and 4.9. DKT is a two body event and is present for dilute suspensions. Moreover, in dilute suspensions (in the present chapter $\varphi \leq 0.1$) as the solid volume fraction increases the chances of DKT decreases due to the increase of multi-body interactions. It can be visualized that DKT will have a large effect on particle settling. It is observed that wakes for $Re \leq 0.2$ supports no DKT, for $0.2 \leq Re \leq 1$ wakes are strong enough to support DK and for about $Re > 1$ wakes becomes sufficiently strong to promote all the three phases of DKT. The frequency of DKT depends upon the Reynolds number i.e. the larger the Reynolds number more frequent will be DKT for particles.

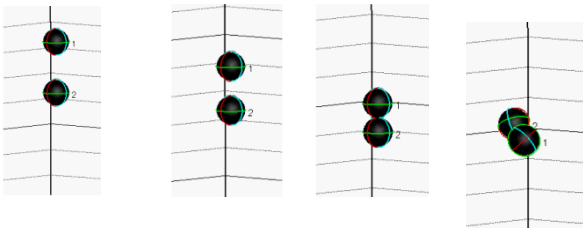

Fig. 4.8 Particle arrangements during DKT

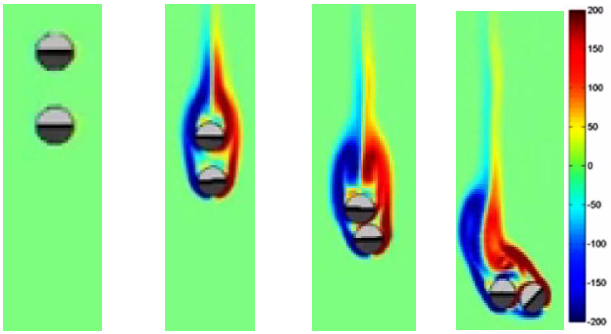

Fig. 4.9 Fluid vorticity during DKT

In the case of more than two particles these interactions become much more complex and anisotropic. Thus the structures of particles should be non-random. It is obvious that these particle structures are difficult to study experimentally and that's why in literature[78-80] experimental work is primarily focused for two dimensions and low solid volume fractions.

In DNS it is possible to keep track of all particles accurately for long durations. For the analysis of structure under the effect of different solid volume fraction and Reynolds number, particle clusters (which are local group of particles with large

correlations) and radial distribution function (RDF) are studied.

4.3.4.1 Cluster analysis

In hindered settling, clusters are close groups of particles. In simulations, clusters are defined in a mathematical way with the property that each particle lies within a distance ad_p of another particle in the cluster. Particles which do not have a neighbour particle in a cluster within ad_p are not considered in the same cluster. Similar method was proposed by Herrmann et al.[81] for percolation problem, i.e. two particles of diameter d_{pi} and d_{pj} with positions $\boldsymbol{r}_i$ and $\boldsymbol{r}_j$ are considered to be in the same cluster if:

$$\left|\boldsymbol{r}_i - \boldsymbol{r}_j\right| \leq \frac{a\left(d_{pi} + d_{pj}\right)}{2} \tag{4.13}$$

As mono-disperse spheres are considered in this study so both d_{pi} and d_{pj} are d_p. The parameter a is critical in cluster size classification. The domain size and the solid volume fraction can give some idea for its selection but still it is not explicit. Wylie and Koch[82] proposed that this parameter should be larger than the lubrication cut-off distance (they took lubrication cut-off distance equal to $0.01d_p$) and smaller than the particle radius for their results to remain independent with this parameter. Xiong et al.[83] studied this parameter and observed that the results remain qualitatively same by changing it from 1.05 to 1.2 of particle diameter. In the present simulations, a is studied for φ=0.05 and *Re*=50. The reason for φ=0.05 is that it gives more degree of freedom for its value selection (i.e. large value of *a* is possible without forcing all the particles into one single cluster) and *Re*=50 is that the temporal integration and disintegration of particle clusters is more frequent for *Re*=50. The values of *a* analyzed in simulation are 1.05, 1.1, 1.15, 1.2, 1.25, 1.5 and 2. For its understanding, the time evolution of N_c (percentage of particles participating in cluster of any size) is studied by taking the above mentioned values of a. N_c is defined by Eq. (4.15).

$$N_i = \frac{n_{ci}}{n_p} \times 100 \tag{4.14}$$

$$N_c = \sum_{i=2}^{M} N_i \tag{4.15}$$

where n_p is the total number of particles, n_{ci} is the number of particles participating in the clusters of size i, N_i is the percentage of particles participating in cluster of size i, M is the maximum cluster size formed in the simulations. The size of a cluster is defined as the number of particles that compose the cluster. The time evolution of N_c for φ=0.05 and Re=50 is shown in Fig. 4.10.

It can be seen from Fig. 4.10 that for $a \leq 1.25$ the temporal evolution patterns are almost not affected. However for a=1.5 and 2, the circle around a particle in which the neighbor is considered to be in the same cluster becomes so big that it cannot capture the sharp formation and dissolution of particle clusters. For both a=1.5 and 2 about more than 50% of particles are observed to be in clusters even for φ=0.05 which is clearly incorrect from physics. Based on the above discussions, a =1.05 is used throughout simulations because it is expected to work well for all high solid volume fractions.

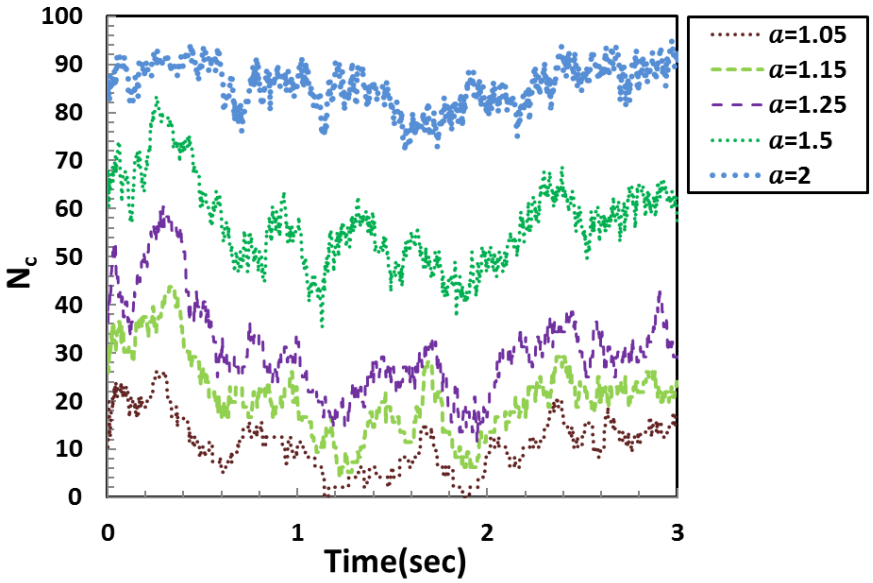

Fig. 4.10 Time evolution of percentage of particles as clusters (φ=0.05 and Re=50)

After the steady state is established, the fraction of particles as single particles N_1, two particle clusters (doublets) N_2, three particle clusters (triplets) N_3 and clusters of more than three particles N_{4-} are calculated and results are time averaged for about 300 Stokes time after the establishment of steady state. The results for Re=1, 10, 20, 30, 40 and 50 are shown in Fig. 4.11. For φ=0.01 the particles only formed doublets so

they are only shown in two particle cluster.

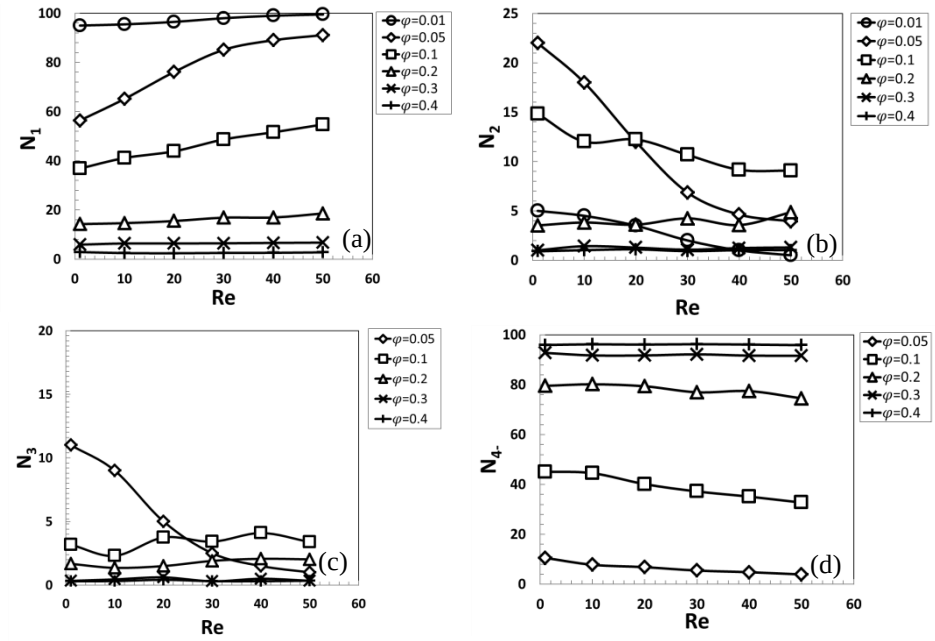

Fig. 4.11 Percentage of particles participating in clusters of (a) Single particle size (b) Two particle size (c) Three particle size (d) More than three particle size

It can be observed from Fig. 4.11 that for the same Reynolds number the particle clustering phenomenon becomes more pronounced by increase in solid volume fraction. This is indicated by the decrease in the fraction of particles being alone as the solids hold up increases from 0.01 to 0.4. These results are consistent with the statistical intuition as the solid volume fraction increases the average inter-particle distance decreases and hence the more particles move collectively.

The Reynolds number adversely affects the degree of particle clustering and this effect is more evident for low solid volume fractions. For example, for φ=0.01 and *Re*=50 about all of the particles are not participating in any cluster and for φ=0.05 the fraction of particles that are not participating in any clusters increases from about 0.56 to 0.91 for increase of Reynolds number from 1 to 50. The effect of Reynolds number becomes lesser as the solid volume fraction increases and almost no effect for φ= 0.3 and 0.4.

One more thing that needs to be discussed in this section is the effect of domain size on particle clustering. It is observed that for $Re \leq 1$ and $\varphi \leq 0.01$, the percentage of single particles decreases (i.e. from about 99% to 95% for L/d_p from 10 to 50) or in other words particle clustering increases with the domain size. However for $Re > 1$ and $\varphi \leq 0.01$ or $\varphi > 0.01$ and all studied range of Reynolds number, domain size negligibly affects the particle clustering. Thus the conclusion of this section i.e. particle clustering is inversely proportional to the Reynolds number for dilute suspension and about independent with Reynolds number for dense suspension is still valid for larger domain sizes.

4.3.4.2 Radial Distribution Function (RDF)

Another measure of the suspension microstructure is the radial distribution function (RDF). RDF is commonly used for analyzing the structures of molecules in solids[84,85], liquids[86] and gas[87] or to study the packing of different arrangements of spheres[88]. It is usually plotted as a function of the inter-particle distances. In the present and the next chapter it is used to give the information about overall structures formed in the suspension. Some of its features are: its value is always zero for distances less than particle diameter as particles cannot approach more closer than particle diameter, appearance of peaks at long range indicates a high degree of ordering and at very long range RDF tends to a value of 1 which happens because RDF describes the average number density at this range. The definition of RDF $g(r)$ is given by the equation:

$$g(r) = \frac{n(r)}{4\pi\rho^n r^2 \Delta r} \tag{4.16}$$

where $n(r)$ is the number of particles in the shell of radius r, ρ^n is the number density and Δr is the shell radius. This function is averaged over all particles to give the information for overall structure. Furthermore, the RDF's shown in the Fig. 4.12 are time averaged for 300 Stokes time after steady state. For comparison with the RDF for hard sphere molecules, the RDF for the Percus-Yevick equation[70,89] is used and shown in Fig. 4.12 by HS.

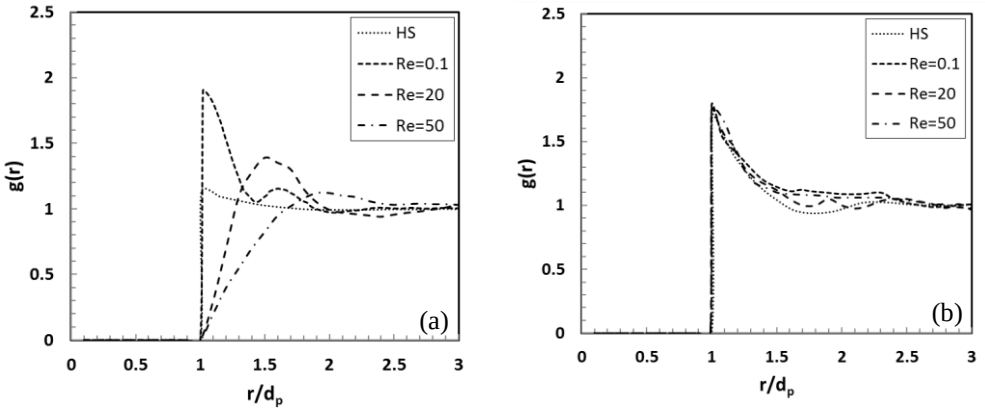

Fig. 4.12 Radial distribution function for (a) φ=0.05 (b) φ=0.2

For dense cases (φ=0.2) there is no significant effect of Reynolds number on RDF and it is quite similar like hard sphere distributions for all the Reynolds number. However, for relatively dilute case (φ=0.05), It can be seen that the particle distributions in settling is different from the random distribution of spheres. For *Re*=0.1-1 the particles show more close pairs with higher peaks of RDF at smaller shell radius in comparison with random distribution of particles. However as the Reynolds number increases for *Re*>1, RDF changes both in magnitude of the peak value and the region where this peak lies (the peak value shifts to r/d_p =2 and the peak value changes from 1.35 to 1.18 for *Re*=30-50). However, at long inter-particle distances i.e. $r/d_p \geqq 3$ the particles distributions show randomness with RDF≅1. The reason for decrease in the particle clustering and the behavior of RDF with Reynolds number will be explained in the next section.

For studying the effect of domain size on RDF, two cases have been studied i.e φ=0.01 and *Re*=1 and 50. Like velocity fluctuations in the previous section RDF changes with the increase in domain size for *Re*=1. However for *Re*=50 the effect of domain size on RDF is negligible for $L/d_p \geq 25$.

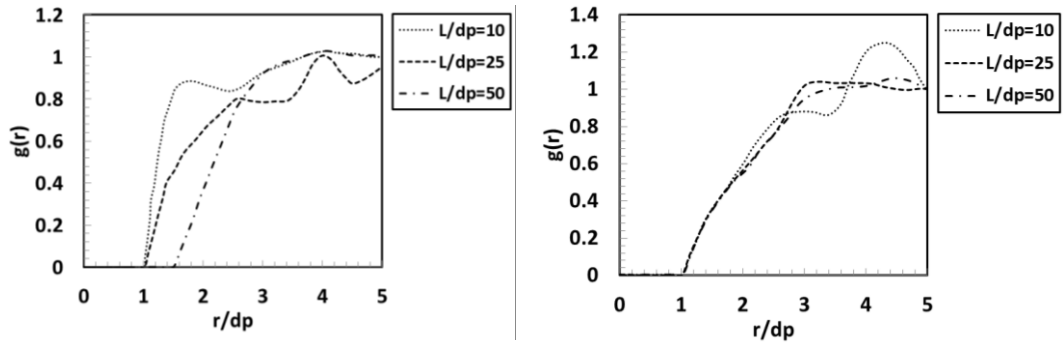

Fig. 4.13 Radial distribution function for φ=0.01
(a) *Re*=1 (b) *Re*=50.

4.4 Physics of hindered settling, velocity fluctuations and microstructures

For explaining the physics, the problem is need to be divided into three cases i.e.
Case 1: Low solid volume fraction ($\varphi \leq 0.1$) and low Reynolds number ($Re \leq 1$)
Case 2: Low solid volume fraction ($\varphi \leq 0.1$) and moderate Reynolds number ($Re > 1$)
Case 3: High solid volume fraction ($\varphi > 0.1$) and low and moderate Reynolds number.

For Case 1, the flow around the particles remains axisymmetric. Because of the hydrodynamic interactions between particles, the particles form pairs but because of the absence of strong wakes they remain in contact for longer times and remain stable in the form of particle pairs. The behavior of near particle pairs and high peaks of RDF at r/d_p=1 for Case 1 in Fig. 4.12 can be due to weak wake interactions. Similar phenomenon was also observed in the simulations of Hamid et al.[90] and Brady et al.[91] in their investigations of the effects of hydrodynamic forces on non-Brownian settling particles.

For Case 2 as the Reynolds number increases from the Stokes condition, fluid inertia breaks the symmetrical flow around the particles and wakes are generated from particles. These wakes from the leading particles reduces the drag for the trailing particle. The trailing particle therefore approaches the leading particle. Koch[77] proposed if the particles' inertia is small then the trailing sphere drifts away from the

wake of leading particle under the effect of Saffman lift force rather than touching the leading particle. However, if the particles' inertia is large the two spheres come into contact with each other and then the trailing sphere rotate and the particles form horizontal pairs. This horizontal arrangement of particles is unstable and makes the particles to move away from each other into pairs at some separation distance perpendicular to the settling direction (DKT). After DKT the particles remain separated as the particles experience repulsion fluid force in side-by-side arrangements. In the case of low φ, there is plenty of space for particles to move thus the DKT events can occur more easily. This leads to separated particles perpendicular to the gravity direction, less probable particle pairs and decrease of the magnitude of RDF for smaller shells.

For Case 3 because of the smaller inter-particle distances the multi body interactions dominates the DKT effects. This leads to relatively isotropic particle structures similar to the distribution of hard sphere molecules as was observed in the RDF and makes the particles distribution independent of the Reynolds number.

A sequential snapshots of one of the DKT events observed in the simulation for φ=0.05 and Re=50 are shown in Fig. 4.14. In this case the particles have sufficient inertia that enables the particles to kiss rather than drift-out from the wakes during the drafting stage.

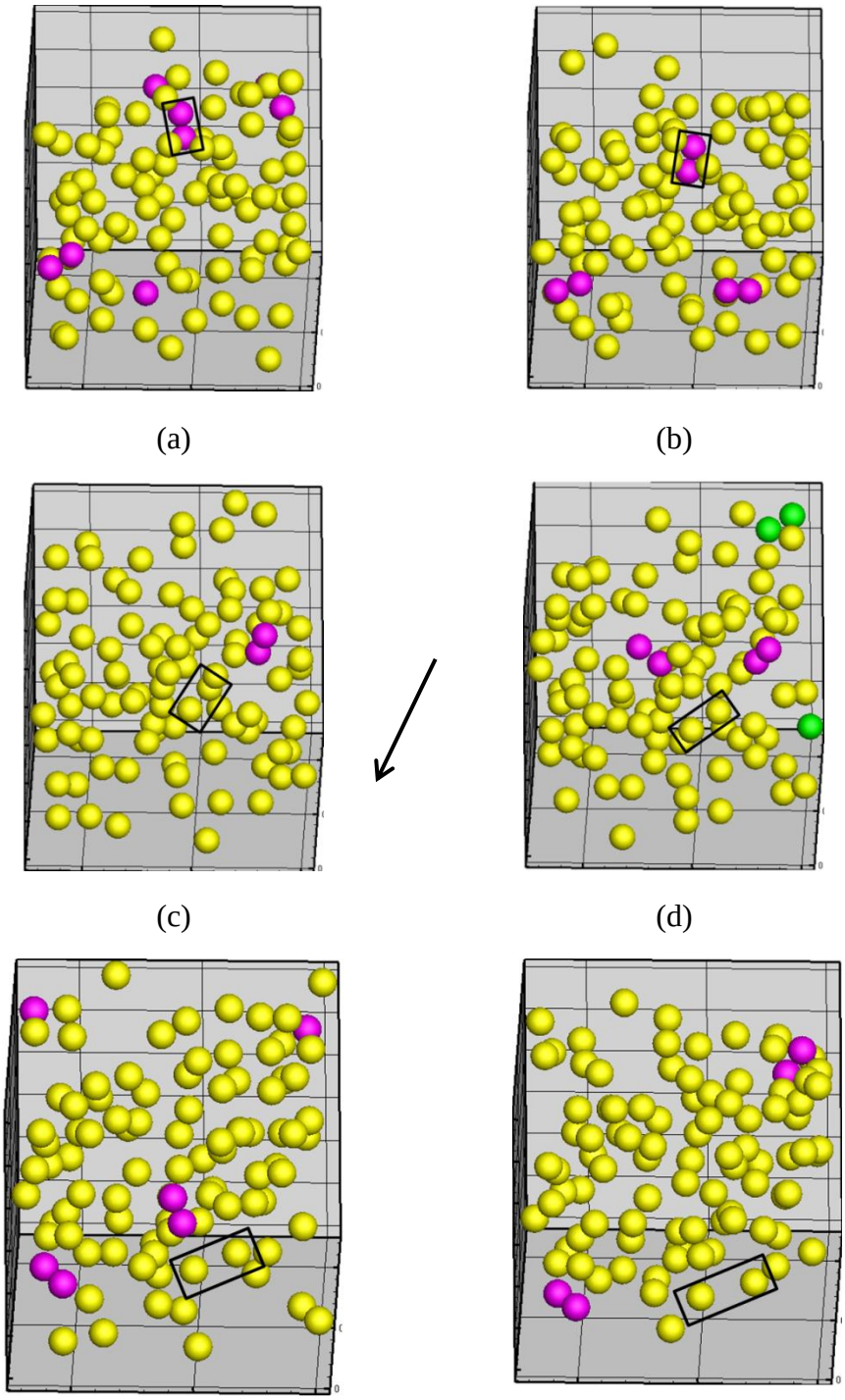

Fig. 4.14 Sequential snapshots of Drafting-Kissing and Tumbling (DKT) event observed in the present simulation (φ=0.05, Re=50) (Arrow shows gravity direction)

To see the interactions of wakes between particles, distributions of magnitude of

vorticity in the computational domain are shown in Fig. 4.15, which shows the contour plots of the slice at the middle of the computational domain for φ=0.05 and 0.3; *Re*=1 and 50. In the figure the circles are the particle cross-sections. The magnitude of vorticity is non-dimensionalized by V_{p}/d_p.

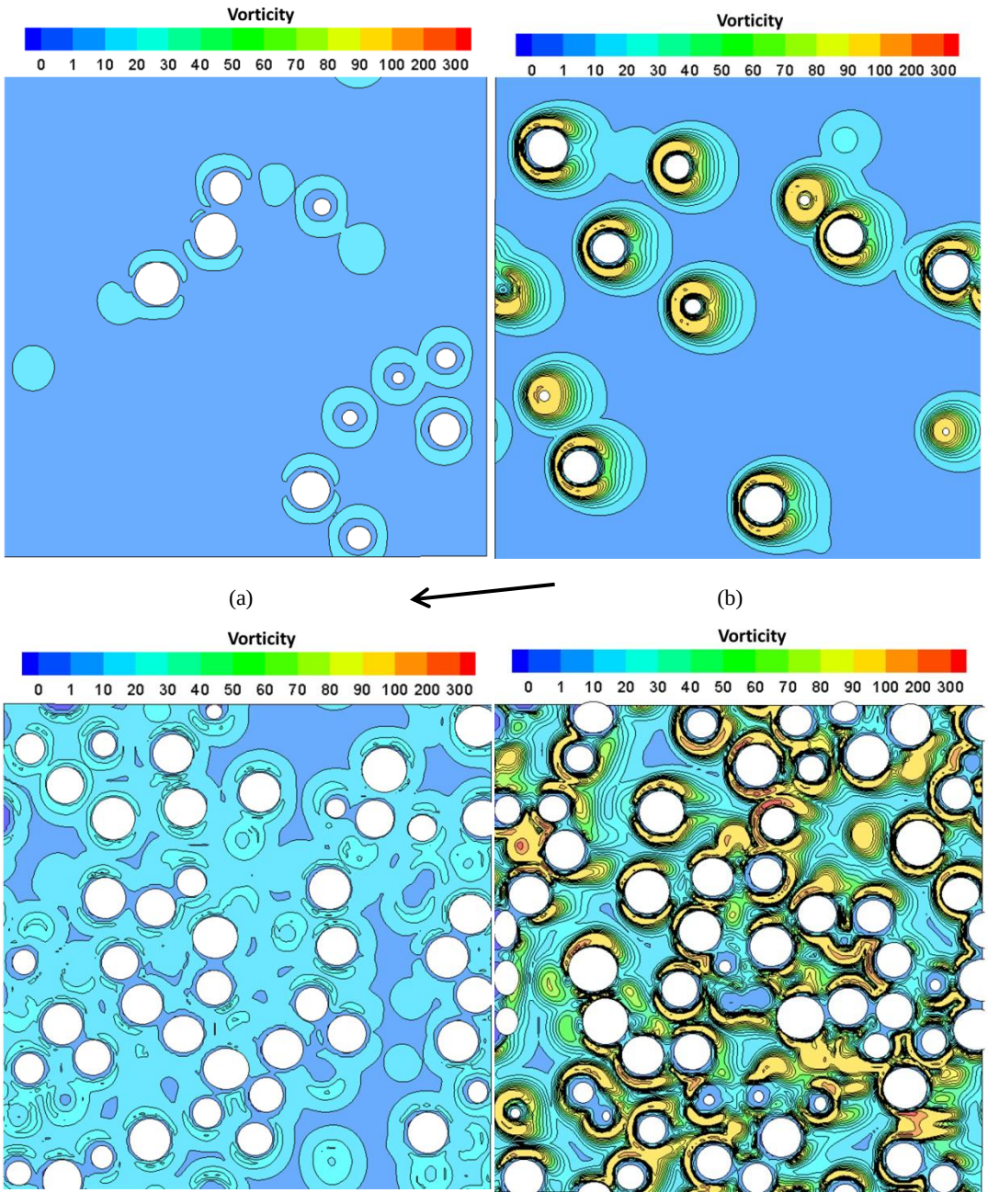

Fig. 4.15 Contour plot of magnitude of vorticity (a) φ=0.05 and *Re*=1 (b) φ=0.05 and *Re*=50 (c) φ=0.3 and *Re*=1 (d) φ=0.3 and *Re*=50 (Arrow shows gravity direction)

It can be seen that as the Reynolds number increases the intensity and area of vorticity region around the particles also increases and thus the downstream wakes affects greater region. On the other hand when the solid volume fraction increases the downstream wakes structures are perturbed among many particles because of small inter-particle spacing.

The deviation of average particle velocity from the power law of Richardson and Zaki was only observed for the case of φ=0.05 and *Re*=50. This can be due to the particle microstructures which are developed from the DKT events. As it is already explained that DKT events will lead to horizontally separated particles and thus the drag force experienced by each particle will be increased because of absence of particle motions in the wakes of other particles for longer times. Thus this reduces the average particle velocity of spheres in comparison with the power law associated with the random sphere distributions.

4.5 Conclusions

In this chapter, the dynamics of settling particles is studied numerically by using Immersed Boundary Method and Discrete Element Method. The Reynolds number based on the terminal velocity of particle ranges from 0.1 to 50 and the solid volume fraction ranges from single sphere to 0.4.

It is found that the settling velocity for low solid volume fractions and moderate Reynolds number largely deviates from the established power law of Richardson and Zaki. This deviation is observed in the region of $0.002<\varphi<0.1$ in which two body interactions or effects of DKT are observed to be dominant. For dense suspensions $\varphi>0.1$ the smaller inter-particle distances diminishes the wake structures necessary for DKT. DKT leads to horizontally separated particle pairs and thus increase in the drag force on particles. The increase in drag force decreases the average settling velocity and this is the reason for the deviation from Richardson and Zaki relation and nonlinearity in the average settling velocity for monodisperse spherical particles. By using the present simulation data, curve fitting is done and a new correlation is proposed for average settling velocity. Furthermore, the effect of domain size on velocity fluctuations of particles and fluid is also studied for both low and moderate range of Reynolds number. The increase of velocity fluctuations with domain size diminishes for moderate Reynolds number due to the decrease in the region affected by

particles by increase in Reynolds number. It is also observed that the Reynolds number has an adverse effect on particle pairing and clustering for dilute suspension in the present range of *Re*. The reason for this phenomenon can also be DKT as it supports horizontally separated pairs and not particle clusters. Furthermore, it was observed in this chapter that for studying the nonlinear effects in settling, dilute suspensions are the best candidates. In the next chapter, dilute suspensions are studied in more detail.

Chapter 5 **Particle settling for dilute suspension**

In the previous chapter it was observed that the dilute suspension showed a strong nonlinearity and deviation from expected settling behaviour. In this chapter, in order to clarify the physics of this strong nonlinearity, dilute suspension settling is studied in more detail for the extended range of Reynolds number. The sequence of this chapter is as follows in Section 5.1 brief introduction and literature review are given, it is followed by simulation setup in Section 5.2, discussion of results in Section 5.3 and conclusions in Section 5.4.

5.1 Introduction

In the previous chapter, particles dispersion in hindered settling was studied. Furthermore, it was observed that solid volume fraction inversely affect this two body event in settling. DKT showed strong effects for $\varphi \leq 0.01$ mild effects $0.01 < \varphi \leq 0.1$ and about no effects for $0.1 < \varphi \leq 0.4$. In this chapter, effects of particle clusters on average settling velocity, velocity fluctuations and particle structures are studied for $\varphi \leq 0.05$ and $1 < Re \leq 300$. Furthermore, it is studied how solid volume fraction adversely affects the particle clusters in dilute suspension. For point particles in externally induced homogenous turbulence it is proposed[24] that ratio of average settling velocity of particle to fluid velocity fluctuation is a good criteria for measuring particle clustering. In this chapter, this ratio is studied for particle induced turbulence.

5.2 Simulation Setup

As shown in the previous chapters, periodic domain is used in all the three directions. The particles are settled under the action of gravity with zero volume flow rate in the domain to mimic the unbounded suspension. For the conditions of particles and fluid please read Section 4.2. For investigations $\varphi \cong 0.005$, 0.01, 0.03, 0.05 and $Re \cong 1$, 50, 100, 175, 250, 300 are studied. The settling Reynolds number is controlled by changing the gravity magnitude. The Reynolds number (Re) is based on the terminal velocity of single particle.

All the results which will be discussed later are time averaged for about 1000

Stokes time after steady state is obtained. For φ=0.005, 0.01 L/d_p=170 is used and for φ=0.03, 0.05 L/d_p=100 is used in the horizontal two directions. The domain size in the gravity direction is elongated two times than the other two directions. These domain sizes ensured sufficient number of particles for obtaining the averaged results. The number of particles in the computational domain for φ=0.005, 0.01, 0.03 and 0.05 are 11729, 23458, 14324 and 23874 respectively.

5.3 Results and discussion

5.3.1 Time evolution of average Reynolds number

The temporal evolution of average settling Reynolds number ($Re_p = V_p d_p/\nu$) of particles is shown in Fig. 5.1. The average fluid velocity is zero during simulations, thus the Reynolds number based on the slip velocity between particles and fluid and the average particle settling velocity are same. In all the studied cases of φ and *Re*, as can be seen in Fig. 5.1, the mean settling velocity initially increases and reaches a peak value, then it decreases and approaches a steady state. Furthermore, fluctuations in the average settling velocity about the steady state increase with the increase in the Reynolds number. These fluctuations and existence of peaks and valleys are due to the changing microstructures during settling. Velocity fluctuations in the average settling velocity and their relation with microstructures is explained in detail by Xiong et al.[83]

In Fig. 5.1 the broken lines correspond to the Reynolds numbers calculated from Eq. (4.7). It can be seen that for φ=0.005 and 0.01, the average settling velocity from simulations for *Re*=175, 250 and 300 is usually greater than the Reynolds number calculated from Eq. (4.7). Moreover, for the other cases, it is less than the value predicted by Eq. (4.7).

For more clarification, the ratio of Re_p to *Re* is calculated with void fraction (1-φ) in Fig. 5.2 and n_e with φ for different *Re* in Fig. 5.3. The general trend of Re_p/Re is shown by solid black line for 1≤*Re*≤100 and black dashed line for 175≤*Re*≤300 in Fig. 5.2. In Fig. 5.3 the two blue dashed lines shows the upper and lower limit of n_e from Eq. (4.8) for 1≤*Re*≤300. As Eq. (4.8) is independent with solid volume fraction thus straight lines are obtained.

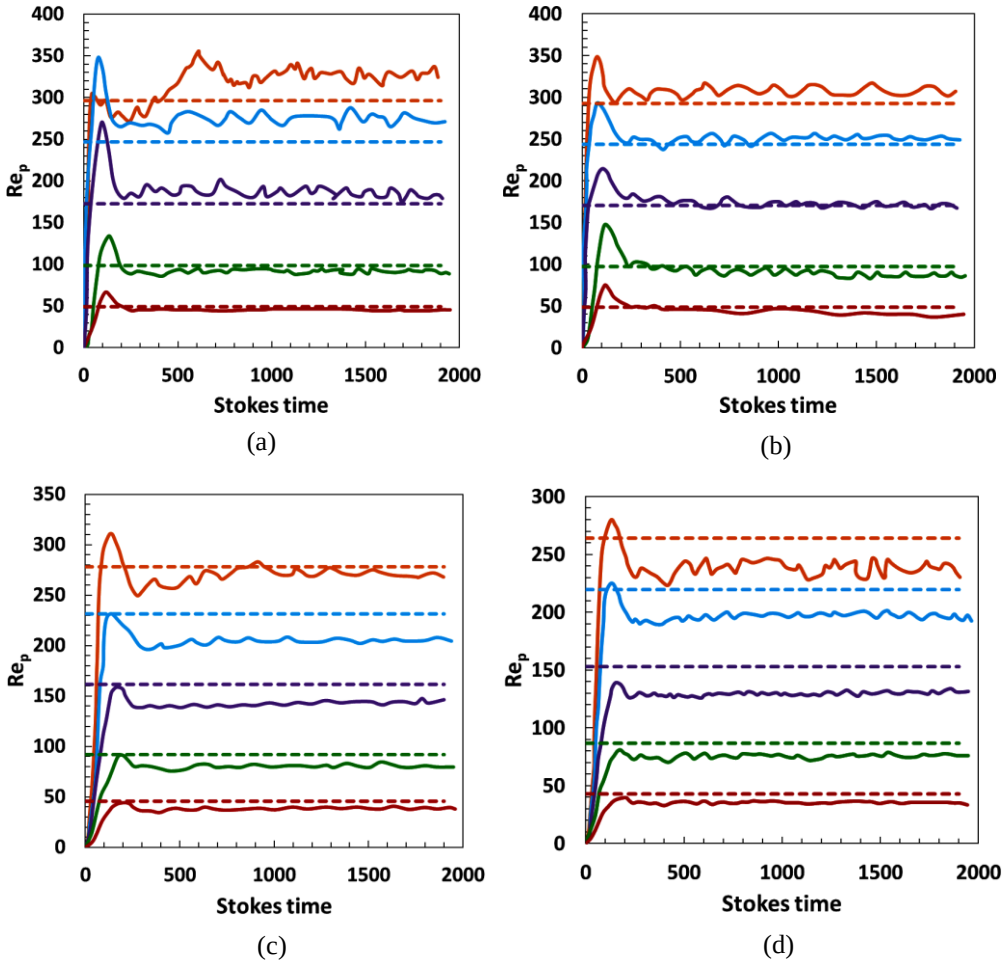

Fig. 5.1. Time evolution of settling Reynolds number (a) φ=0.005 (b) φ=0.01(c) φ=0.03 (d) φ=0.05 (*Re*=300, 250 175, 100 and 50 is represented by orange, blue, purple, green and red color respectively)

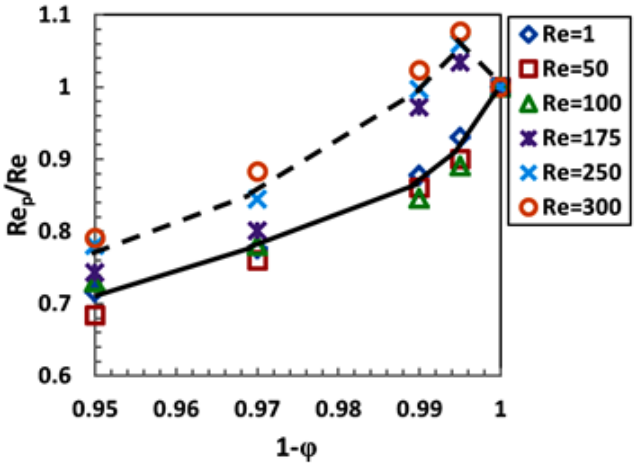

Fig. 5.2. Variation of Re_p/Re with (1-φ)

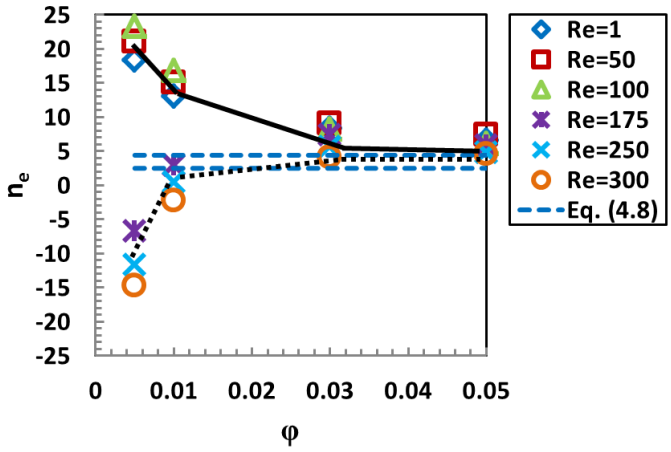

Fig. 5.3. Variation of n_e with *Re* and φ

It can be seen in Fig. 5.3 that Eq. (4.8) shown by blue dashed line is not a suitable approximation for n_e in the studied range of *Re* and φ. The trend of n_e observed by simulations is as follows.

1. For $0.005 \leq \varphi \leq 0.01$ and $1 \leq Re \leq 100$, n_e decreases with Reynolds number.
2. For $0.005 \leq \varphi \leq 0.01$ and $175 \leq Re \leq 300$, n_e increases with Reynolds number.
3. For $0.03 \leq \varphi \leq 0.05$ and $1 \leq Re \leq 300$ n_e varies with in the range of 9 to 4.

In the studied range of Reynolds number and solid volume fraction a better way for the development of average settling velocity relation is to introduce a multiplication factor k_1 in Eq. (4.11). The improved relation is given by:

$$Re_p = k_1 Re(1-\varphi)^{n_e} \tag{5.1}$$

In the above relation, n_e remains the same as proposed by Richardson and Zaki[42]. This method was proposed by De Felice[74] for more concentrated suspensions, i.e. $\varphi > 0.05$. The equation for k_1 is given by Eq. (5.2). The lines of curve fitting are shown by solid black line in Fig. 5.4.

$$k_1 = \begin{cases} 0.17C^2 - 0.37C + 1 & 0.005 \leq \varphi \leq 0.01 \\ 0.06C^2 - 0.18C + 0.96 & 0.03 \leq \varphi \leq 0.05 \end{cases} \tag{5.2}$$

where $C = \log Re$

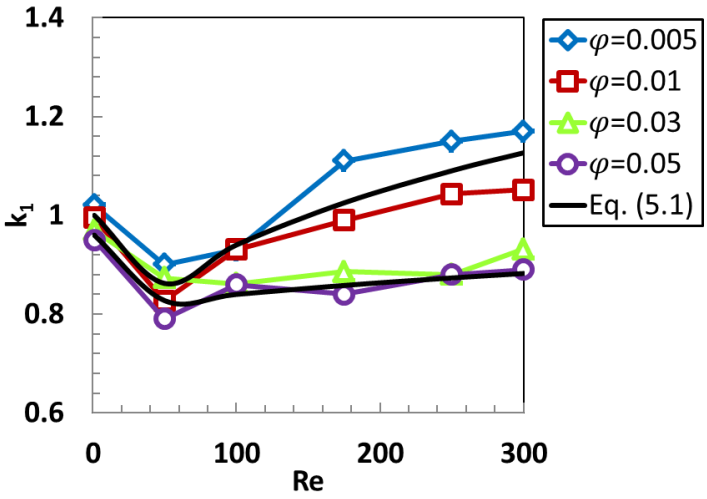

Fig. 5.4. Variation of k_1 with *Re* and φ

The studied behavior of averaged settling velocity is due to the different microstructures formed at different Reynolds number and will be discussed in the next section.

5.3.2 Particle structures during settling

In the previous chapter it was observed that the particles make structures during settling due to hydrodynamic interactions. The radial distribution function (RDF) for the studied cases is shown in Fig. 5.5. For comparison with the hard spheres structure (HS), RDF of the Percus-Yevick [70,89] equation is also shown.

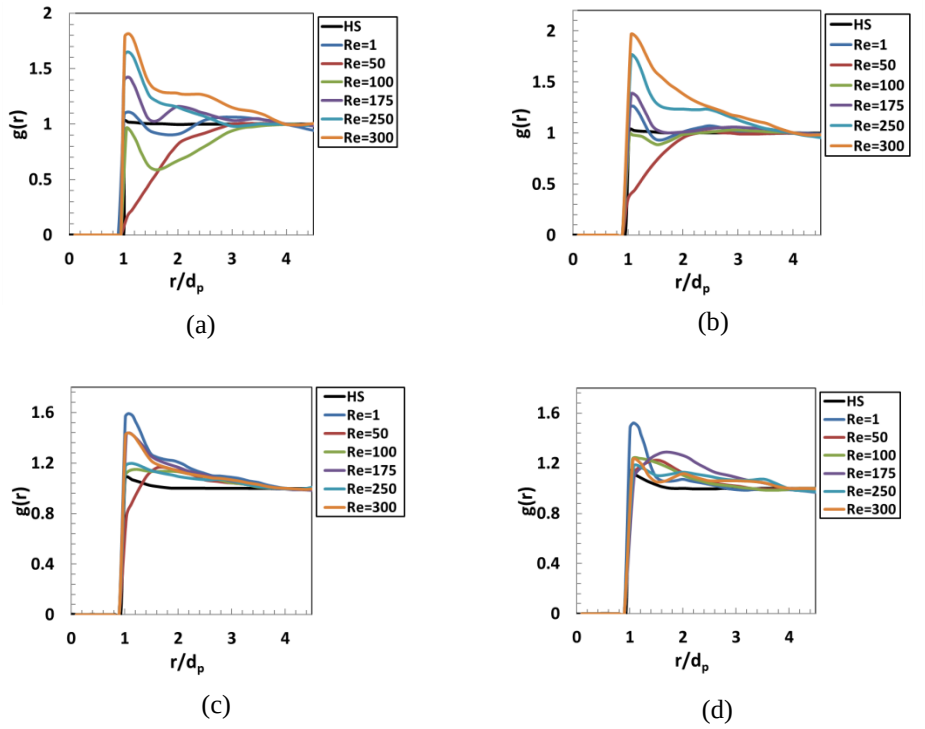

Fig. 5.5. Radial distribution function for (a) φ=0.005 (b) φ=0.01 (c) φ=0.03 (d) φ=0.05

It can be seen that in about all the studied cases, RDF of the particles settling under gravity and that of hard spheres is different. In case of φ=0.005, 0.01, RDF shows closer particle pairs for *Re*=300, 250, 175 and 1. Moreover in these cases, the peak value at r/d_p =1 and the region of r in which RDF>1 is inversely proportional to the Reynolds number. For φ=0.005, 0.01 and *Re*=50, 100 the RDF around r/d_p =1 is smaller than the HS distribution indicating most of the particles separated with each other. For φ=0.03, 0.05 weak particle clustering is observed for *Re*=1. However, further increase in Reynolds number has negligible effect on RDF.

Another way for characterizing the particle clustering is to calculate nearest neighbor distance (D_{NN}). D_{NN} is defined by.

$$D_{NN} = \frac{1}{n_p}\sum_{i=1}^{n_p} \min_{j=1,n_p\, j\neq i} r_{i,j} \tag{5.3}$$

where $r_{i,j}$ is the distance between centres of particles i and j which is given by Eq. (5.4).

$$r_{i,j} = |\boldsymbol{r}_i - \boldsymbol{r}_j| \tag{5.4}$$

$\boldsymbol{r}_i$ and $\boldsymbol{r}_j$ are the position vectors of particle i and j respectively. The function $\min_{j=1,n_p\ j\neq i}$ in Eq. (5.3) is a function that gives the minimum $r_{i,j}$ for particle i and j=1 to n_p and j is not equal to i. Fig. 5.6 shows the time evolution of D_{NN} non-dimensionalized by D_{NN_0} which is the initial value of D_{NN} (i.e. for random arrangements of particles). Thus at Stokes times equal to zero the value of D_{NN}/D_{NN_0} is equal to one.

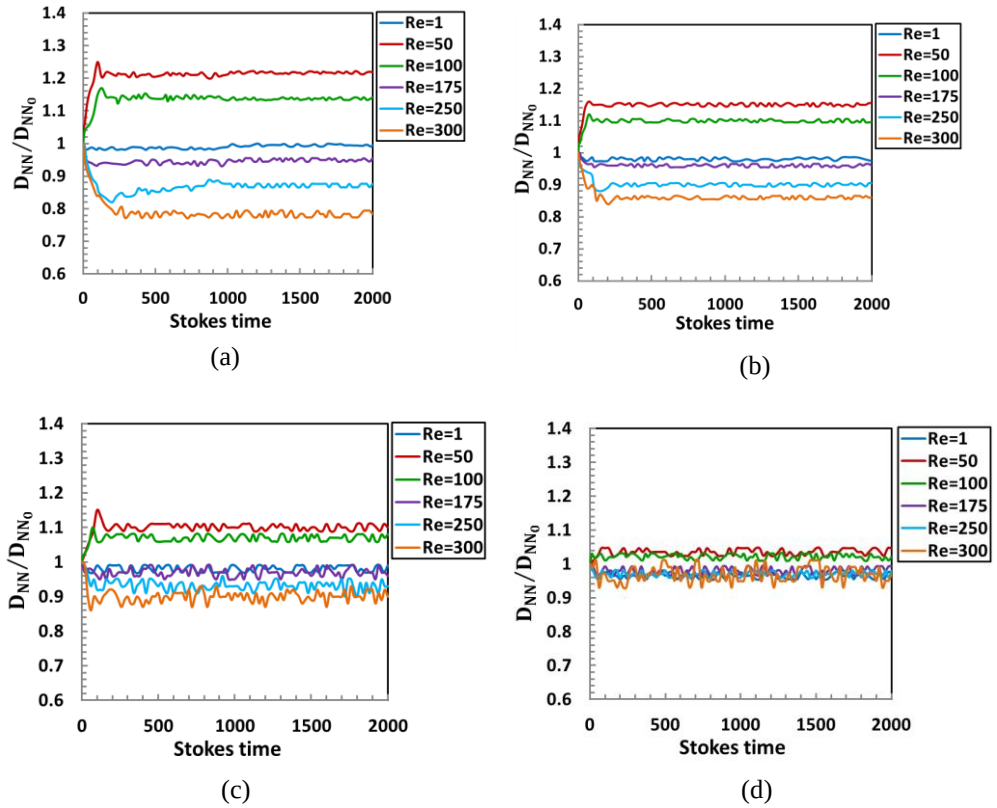

Fig. 5.6. D_{NN}/D_{NN_0} for (a) φ=0.005 (b) φ=0.01 (c) φ=0.03 (d) φ=0.05

Similar like RDF, for φ=0.005, 0.01 D_{NN}/D_{NN_0} becomes less than one as the time evolves and become steady for *Re*=300, 250, 175 and 1. This indicates higher degree of clustering. For φ=0.005, 0.01 and *Re*=50, 100 D_{NN}/D_{NN_0} becomes greater than one showing separated particles. For $\varphi \geqq 0.03$ the effects of Reynolds number on

D_{NN}/D_{NN_0} diminishes.

The explanation of particle structures for $Re \leq 50$ was explained in detail in the previous chapter. By observing the trend of D_{NN}/D_{NN_0} and RDF for Re=100 i.e. particle dispersion, similar discussion can be made. However for $Re \geqq 175$ particles are showing clusters which increases with the increase in Reynolds number. In these range of Reynolds number, the downstream wakes become strong and the particles can interact with each other over large distances. When particles enter in the wakes of upstream particles they become entrapped and remain in these high fluid shear regions, thus making vertically elongated closed particle pairs or clusters and voids in low fluid shear regions. These clusters are quite robust and they persist over long time intervals. Furthermore, these clusters fall faster than the average and this is the reason for higher average settling velocity of particles for $Re \geqq 175$ in comparison with Eq. (4.11). The above discussion is valid for φ=0.005 and 0.01. For φ =0.03 and 0.05, the ratio of average inter-particle distance to the particle diameter is 2.1 and 2.5 respectively as compared to 3.7 and 4.7 for φ=0.005 and 0.01. The ratio of average inter-particle distance to particle diameter (l_p/d_p) is calculated by Eq. (5.5).

$$\frac{l_p}{d_p} = \left(\frac{\pi}{6\varphi}\right)^{1/3} \tag{5.5}$$

The smaller inter-particle distance makes the wakes structures perturbed and thus long chain particle clusters are not formed. This behavior was also observed and explained by Kajishima[52,53]. For further explanation, Figs. 5.7 and 5.8 shows the distributions of particles in the computational domain for φ=0.005 and 0.05 respectively at t'=1500 ($t'=t\,U_s/d_p$ where t' is Stokes time, t is the actual time, U_s is the terminal velocity of single particle and d_p is the particle diameter). For understanding the effects of vortices the iso-surfaces of $\nabla^2 p=10^4$ are also calculated and shown in the enlarged view of small section of the computational domain. In Fig. 5.7 (b) and (c), it can be seen that due to particle-particle wake interactions vertical elongated particle clusters are formed. These elongated clusters make the regions of high particle densities and voidage in the computational domain (especially for Re=300) as can be seen in the top view. Particles also cluster for Re=175 as can be seen is in Fig. 5.7(b) and Fig. 5.8(b). For single particle case, Re=175 corresponds to axi-symmetric vortex flow regime without any vortex shedding. But since the particles come close to each other (for φ=0.005 due to particle-particle wake interactions and for φ=0.05 due to smaller inter-particle spacing) they act as single identities and

consequently the effective Reynolds number increases. The shedding of vortices can be particularly seen in Fig. 5.7(b) and (c). Each particle shed vortices but since the particles are in clusters, the vortices are mixed and very long elongated hair-pin vortices are formed especially for φ=0.005. These long vortices increase the effects of upstream particles and hence the entrapment of downstream particles get further increased resulting in long elongated vertical clusters. However for φ=0.05, because of relatively smaller inter-particle distances the wakes are shared among lots of particles even with those which are not in line with the upstream particles. Thus the effects of wakes on particle clustering get diffused.

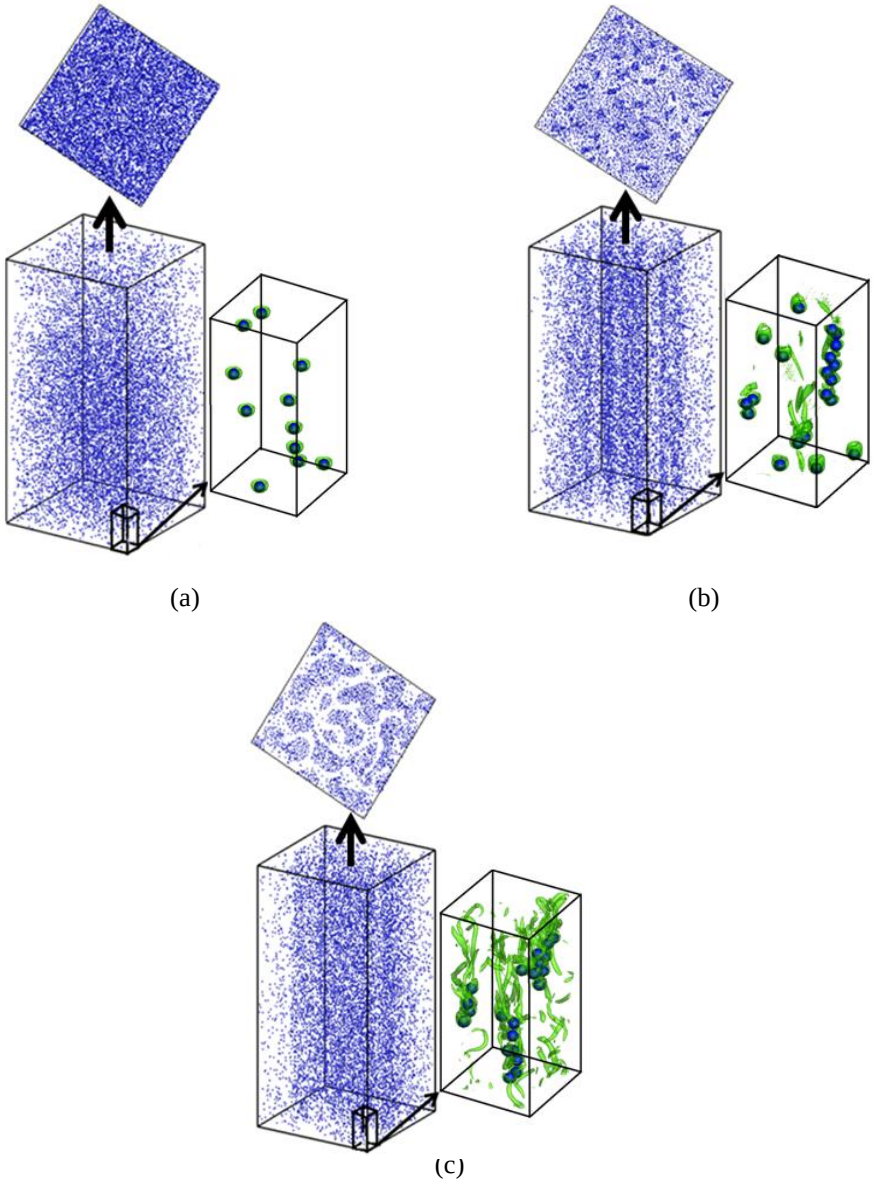

Fig. 5.7. Particle distribution in the computational domain for φ=0.005
(a) *Re*=50 (b) *Re*=175 (c) *Re*=300

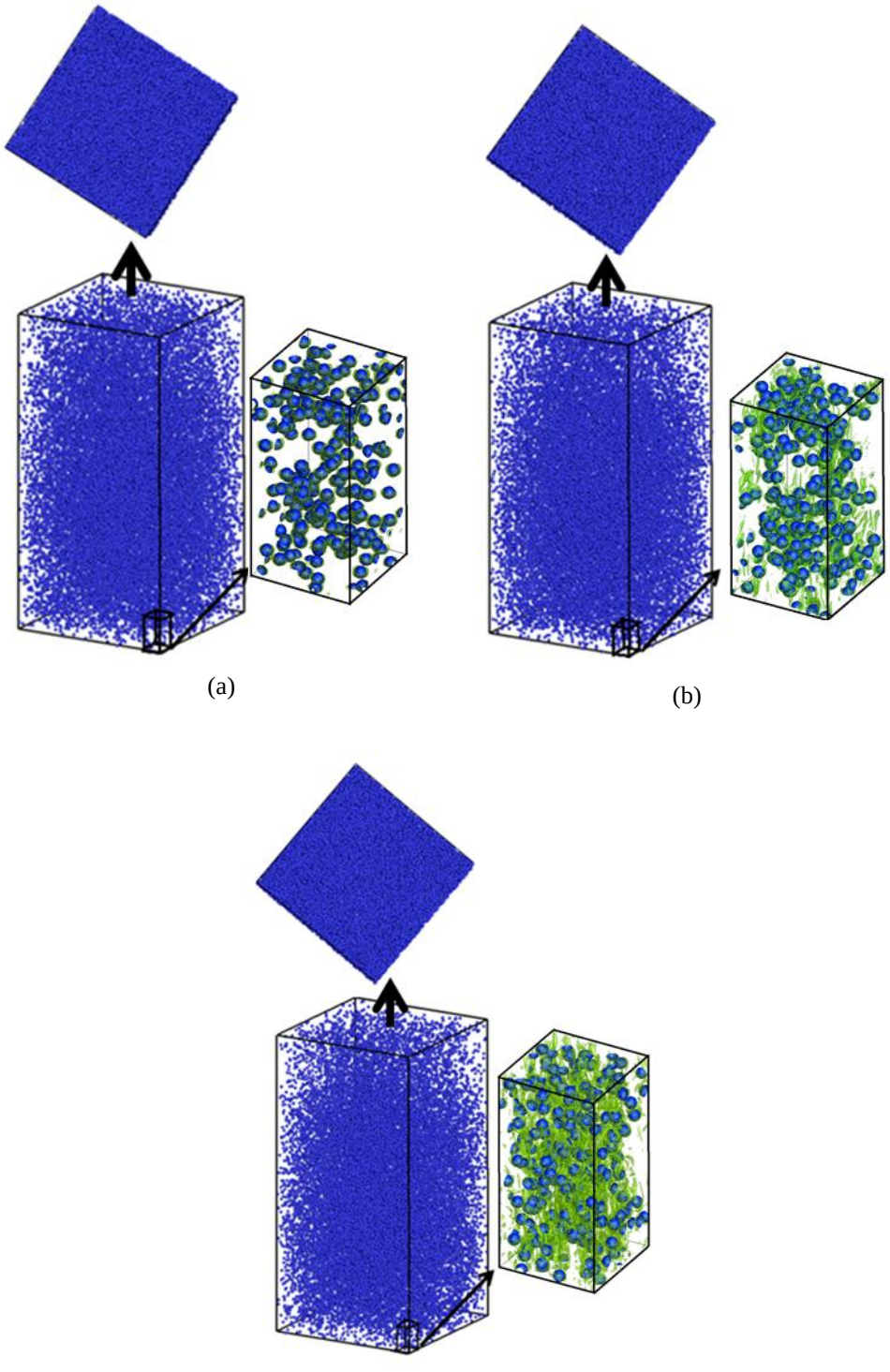

Fig. 5.8. Particle distribution in the computational domain for φ=0.05 (a) *Re*=50 (b) *Re*=175 (c) *Re*=300

One more interesting point which is observed in simulations is that particle clustering is a dynamic phenomenon. The downstream vortices from particles are the regions of high fluid shear. When particles move in high fluid shear regions, they experience Saffman lift force[92] due to the difference of pressure distribution on the particle. Furthermore when particles collide, they also develop rotation. Rotating particles develop lift force due to the Magnus effect[93]. Both these lift forces on particles are sometimes forcing the particles to remain in the same cluster and sometimes forcing them to break-away from one cluster and joins another cluster. Thus in this way, the high density regions of particles kept changing their locations in the computational domain during settling.

5.3.3 Fluid velocity fluctuation

This section is related to the turbulence modulation due to particles. In the present case, there is no external source of turbulence thus any fluctuation or disturbance in the fluid velocity is due to particles. For quantification of turbulence, both along and perpendicular to the gravity direction, RMS values of fluid velocity fluctuations ($\acute{U}_{rms}$) is used and φ=0.005 and 0.05 is used as an example in Fig. 5.9. The velocity fluctuations are non-dimensionalized with the terminal velocity.

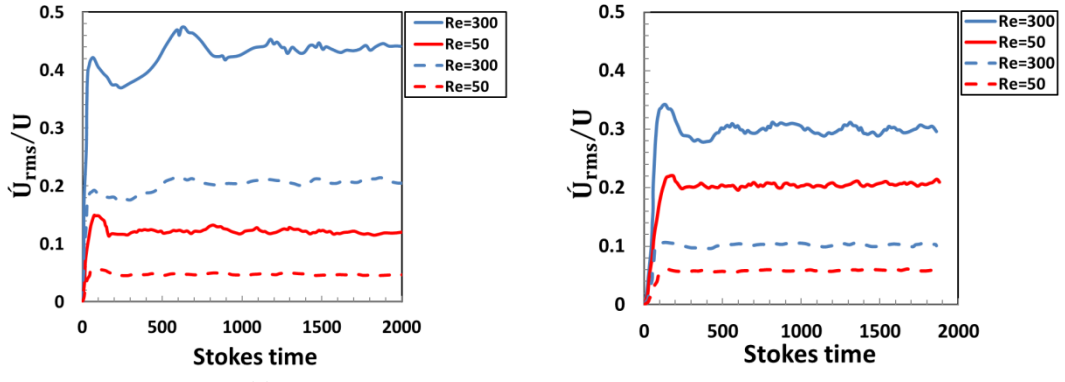

(a) (b)

Fig. 5.9. Time evolution of fluid velocity fluctuations (a) φ=0.005 (b) φ=0.05. Solid line is for fluctuations in the gravity direction and dashed line is for fluctuations perpendicular to the gravity direction

It can be inferred from Fig. 5.9 that the fluid velocity fluctuations for higher Reynolds number are higher. For φ=0.005, the velocity fluctuations for *Re*=300 are about 4 times higher than for *Re*=50. On the other hand for φ=0.05, the velocity fluctuations for *Re*=300 are about 1.5 times higher than for *Re*=50. The larger increase

in the velocity fluctuations with the Reynolds number for φ=0.005 can be due to the enhancements of particle clusters or structures.

One more point that can be noticed from Fig. 5.9 is that the fluid velocity fluctuations in both directions synchronize with each other. However, the fluid velocity fluctuations in the gravity direction are more dominant and have larger value than in the direction perpendicular to gravity. For φ=0.005 and 0.05 the ratio of fluid velocity fluctuations in the gravity direction to the fluid velocity fluctuations perpendicular to the gravity direction are about 2 and 3 respectively. This anisotropy in the velocity fluctuations is due to the wake effects in the settling direction and was also observed by Parthasarathy et al.[94,95] and Xiong et al.[83]. The smaller anisotropy observed for φ=0.005 can be due to complex three dimensional interactions between clusters.

Jin et al.[24] studied preferential concentration of settling particles in isotropic turbulence, for both point and finite-sized particles by numerical simulations. They observed that when point particles fall under the action of gravity in turbulent flow they develop mean drift velocity with the surrounding fluid which increases with the increase in the settling velocity of particles. This increase in drift velocity, drives the particles away from the clustered regions (high strain rate regions of turbulent flow) and thus make the particle arrangements more uniform. For the quantitative measure of this phenomenon they used ratio of average settling velocity to root mean square of fluid velocity fluctuations ($V_p/\acute{U}_{rms}$). Jin et al.[24] proposed that this ratio is inversely proportional to particle clustering. The variation of this ratio with studied Reynolds number and solid volume fraction is shown in Fig. 5.10.

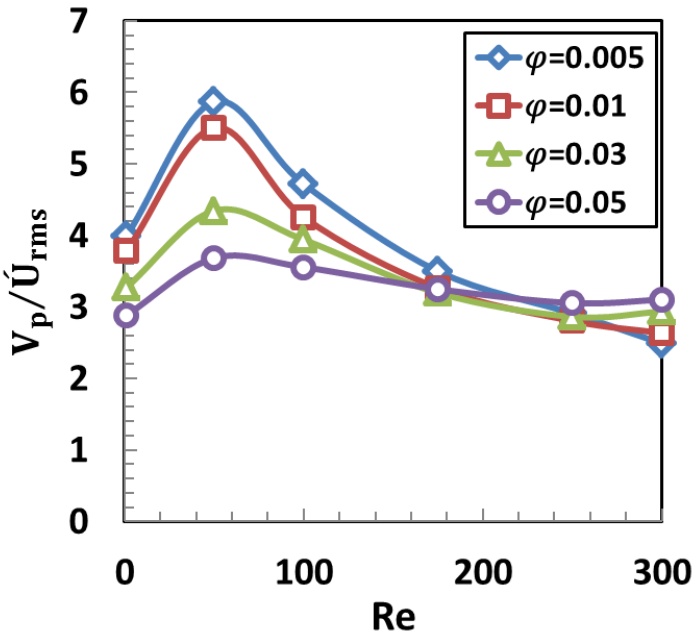

Fig. 5.10. Variation of $V_p/\acute{U}_{rms}$ with *Re*

From Fig. 5.10, it can be seen that for all φ, the qualitative trend of $V_p/\acute{U}_{rms}$ with *Re* is about same. $V_p/\acute{U}_{rms}$ is maximum at *Re*=50 and then it decreases with the increase in the Reynolds number till *Re*=300. Furthermore, $V_p/\acute{U}_{rms}$ decreases with the increase in φ.

To see the relationship between $V_p/\acute{U}_{rms}$ and particle clustering; plot between $V_p/\acute{U}_{rms}$ and time averaged D_{NN}/D_{NN_0} is shown in Fig. 5.11.

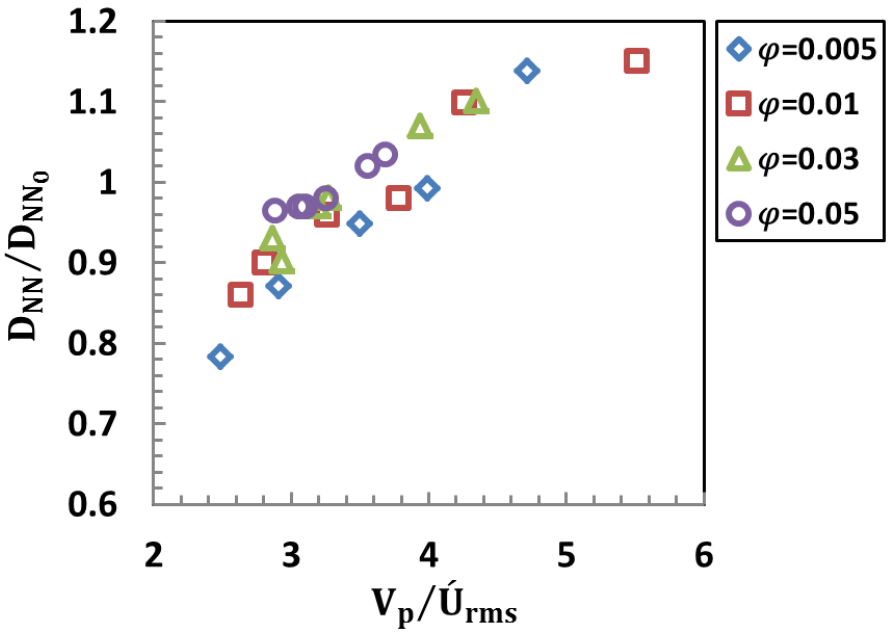

Fig. 5.11. Variation of D_{NN}/D_{NN_0} with $V_p/\acute{U}_{rms}$

It can be seen that D_{NN}/D_{NN_0} increases with the increase in $V_p/\acute{U}_{rms}$. Thus it can be inferred that $V_p/\acute{U}_{rms}$ can be an indicator of particle clustering for free settling without any external source of turbulence. It is because of the relatively larger increase in fluid velocity fluctuations in comparison with average settling velocity when particles form clusters.

5.4 Conclusions

In this chapter, in order to clarify the physics of the strong nonlinearity observed in the dilute range in the previous chapter, settling dynamics of finite sized particles are investigated by DNS using Immersed Boundary Method and Dscrete Element Method. It is observed that for φ=0.005 and 0.01 particles form clusters for *Re*=175, 250, 300. The iso-surfaces of $\nabla^2 p$ showed that the wake structures between particles promote clustering for these cases. However for the rest of studied cases strong particle clustering is not observed. This is because either the cluster promoting wake structure is not developed or attenuated due to smaller inter-particle distance. Weak wakes for *Re*=50 and 100 promote drafting-kissing and tumbling scenario which lead to separated particles. Clustered particle enhances averaging settling velocity and fluid velocity fluctuations in comparison with non-clustered particles. It was found that there is a strong correlation between D_{NN}/D_{NN_0}.

Chapter 6 **Conclusions**

In the present thesis, particle resolved direct numerical simulations are used to study hindered settling. The main objective is to study the effects of Reynolds number and solid volume fraction on the settling of monodisperse spheres. The range of Reynolds number in this thesis varies from 0.1 to 50 for dense suspension and up to 300 for dilute suspension. The conclusions of this thesis are given below:

In Chapter 1, the background, aims and objectives of this thesis is given. In Chapter 2, details of formulation are given. In this thesis, Immersed Boundary Method and Discrete Element Method is used. Thus in Chapter 2, details of the equations of the mentioned methods are given.

In Chapter 3, fluid flow through fixed arrangements of particles are studied and extensive literature data are compared for benchmarking the present simulation code. Reynolds number is varied from 0.01 to 1000 and solid volume fraction is varied from 0.05 to 0.5. The simulations results showed good agreement with most of the available results with the exception of Beetstra et al.[14]. The main reason for this was the overestimation of drag force by Beetstra et al.[14] due to the use of relatively coarse grid. The variation of average drag force on spheres with Reynolds number is studied and it is observed that At the end, a new drag relation for randomly arranged monodisperse particles is proposed given by Eq. (3.14). The results of Chapter 3 gave a platform for performing simulations on more complex free settling particles in Chapters 4 and 5.

In Chapter 4, particle settling is studied for moderate Reynolds number ($1 \leq Re \leq 50$) and wide range of solid volume fractions ($0.002 \leq \varphi \leq 0.4$). The present simulations showed deviation of average settling velocity from the standard power law of Richardson and Zaki[42] for moderate Reynolds number and dilute suspension. It was found that the strong nonlinearity is caused by Drafting-Kissing and Tumbling (DKT) phenomenon. DKT is a phenomenon caused by particles binary interactions, finally make a horizontally separated particle pair that enhances the fluid drag on the particles. The effects of DKT and deviation from power law diminish with the increase in solid volume fraction due to the lack of space to make a binary interaction. At the end, the simulation results are curve fitted to propose a new relation for average settling velocity given by Eq. (4.10)-(4.12).

Chapter 4 introduced more specific problem in particle settling in dilute suspension regime. Thus in Chapter 5, particle settling is studied with particular emphasis on dilute suspension ($0.005 \leq \varphi \leq 0.05$) and with relatively higher Reynolds number ($175 \leq Re \leq 300$). For higher Reynolds number, the strong inter-particle wakes promoted particle clusters due to entrapment of particles in high fluid shear regions. This led to increase in settling velocity and fluid velocity fluctuations. The relation for average settling in dilute regime is given by Eq. (5.1) and (5.2).

This thesis can be used for further studies in hindered settling. In the present thesis, effects of Stokes number or external source of inter-particle attractions like magnetic force is not studied. These areas can be investigated by using the results from this thesis.

References

1. Houghton EL, Carpenter PW. *Aerodynamics for engineering students.* 2003.
2. Campbell DJ. Research & Technology. *NASA/TM-2002-211333.* 2001.
3. Nguyen NQ, Ladd AJC. Sedimentation of hard-sphere suspensions at low Reynolds number. *J Fluid Mech.* 2005;525:73-104.
4. Ding J, Gidaspow D. A bubbling fluidization model using kinetic-theory of granular flow. *AIChE J.* 1990;36(4):523-538.
5. Jackson R. A fluid mechanical description of fluidized beds. *Ind. Eng. Chem. Fundam. 6.* 1967:527–539.
6. Tsuji Y, Kawaguchi T, Tanaka T. Discrete particle simulation of 2-dimensional fluidized-bed. *Powder Technol.* 1993;77(1):79-87.
7. Hoomans BPB, Kuipers JAM, Briels WJ, vanSwaaij WPM. Discrete particle simulation of bubble and slug formation in a two-dimensional gas-fluidised bed: A hard-sphere approach. *Chem Eng Sci.* 1996;51(1):99-118.
8. Xu BH, Yu AB. Numerical simulation of the gas-solid flow in a fluidized bed by combining discrete particle method with computational fluid dynamics. *Chem Eng Sci.* 1997;52(16):2785-2809.
9. Berrouk AS, Wu CL. Two-dimensional discrete particle model: Comment on the numerical simulation of cluster flow behavior in the riser of circulating fluidized beds by Liu and Lu. *Chem Eng J.* 2010;160(2):810-811.
10. Xu M, Chen FG, Liu XH, Ge W, Li JH. Discrete particle simulation of gas-solid two-phase flows with multi-scale CPU-GPU hybrid computation. *Chem Eng J.* 2012;207:746-757.
11. Cundall PA, Strack ODL. Discrete numerical-model for granular assemblies. *Geotechnique.* 1979;29(1):47-65.
12. Hill RJ, Koch DL, Ladd AJC. Moderate-Reynolds-number flows in ordered and random arrays of spheres. *J Fluid Mech.* 2001;448:243-278.
13. Hill RJ, Koch DL, Ladd AJC. The first effects of fluid inertia on flows in ordered and random arrays of spheres. *J Fluid Mech.* 2001;448:213-241.
14. Beetstra R, van der Hoef MA, Kuipers JAM. Drag force of intermediate Reynolds number flow past mono- and bidisperse arrays of spheres. *AIChE J.* 2007;53(2):489-501.
15. Tenneti S, Garg R, Subramaniam S. Drag law for monodisperse gas-solid systems using particle-resolved direct numerical simulation of flow past fixed assemblies of spheres. *Int J Multiphas Flow.* 2011;37(9):1072-1092.
16. Climent E, Maxey MR. Numerical simulations of random suspensions at finite Reynolds numbers. *Int J Multiphas Flow.* 2003;29(4):579-601.

17. Yin XL, Koch DL. Hindered settling velocity and microstructure in suspensions of solid spheres with moderate Reynolds numbers. *Phys Fluids.* 2007;19(9):093302.
18. Yin XL, Koch DL. Velocity fluctuations and hydrodynamic diffusion in finite-Reynolds-number sedimenting suspensions. *Phys Fluids.* 2008;20(4):04335.
19. Ladd AJC. Numerical simulations of particulate suspensions via a discretized Boltzmann-equation .2. numerical results. *J Fluid Mech.* 1994;271:311-339.
20. Ladd AJC. Numerical simulations of particulate suspensions via a discretized Boltzmann-equation .1. theoretical foundation. *J Fluid Mech.* 1994;271:285-309.
21. Kajishima T, Takiguchi S. Interaction between particle clusters and particle-induced turbulence. *Int J Heat Fluid Fl.* 2002;23(5):639-646.
22. Kajishima T. Influence of particle rotation on the interaction between particle clusters and particle-induced turbulence. *Int J Heat Fluid Fl.* 2004;25(5):721-728.
23. Doychev T, Uhlmann M. Settling of finite-size particles in an ambient fluid: A numerical study. paper presented at: 8-th international conference on multiphase flow2013 Jeju, Korea.
24. Jin G, Wang Y, Zhang J, He G. Turbulent clustering of point particles and finite-size particles in isotropic turbulent flows. *Ind Eng Chem Res.* 2013.
25. Peskin CS. Flow patterns around heart valves - numerical method. *J Comput Phys.* 1972;10(2):252-271.
26. Kajishima T, Takiguchi S, Hamasaki H, Miyake Y. Turbulence structure of particle-laden flow in a vertical plane channel due to vortex shedding. *Jsme Int J B-Fluid T.* 2001;44(4):526-535.
27. Tsuji T, Narutomi R, Yokomine T, Ebara S, Shimizu A. Unsteady three-dimensional simulation of interactions between flow and two particles. *Int J Multiphas Flow.* 2003;29(9):1431-1450.
28. Glowinski R, Pan TW, Hesla TI, Joseph DD, Periaux J. A distributed Lagrange multiplier/fictitious domain method for flows around moving rigid bodies: Application to particulate flow. *Int J Numer Meth Fl.* 1999;30(8):1043-1066.
29. Simeonov JA, Calantoni J. Modeling mechanical contact and lubrication in direct numerical simulations of colliding particles. *Int J Multiphas Flow.* 2012;46:38-53.
30. Benyahia S. On the effect of subgrid drag closures. *Ind Eng Chem Res.* 2010;49(11):5122-5131.
31. Gomez LC, Milioli FE. A numerical simulation analysis of the effect of the interface drag function on cluster evolution in a CFB riser gas-solid flow. *Braz J Chem Eng.* 2004;21(4):569-583.
32. Heynderickx GJ, Das AK, De Wilde J, Marin GB. Effect of clustering on gas-solid drag in dilute two-phase flow. *Ind Eng Chem Res.* 2004;43(16):4635-4646.
33. Wang SA, Lu HL, Liu GD, Sheng ZH, Xu PF, Gidaspow D. Modeling of cluster structure-dependent drag with Eulerian approach for circulating fluidized beds. *Powder Technol.*

2011;208(1):98-110.

34. Du W, Bao XJ, Xu J, Wei WS. Computational fluid dynamics (CFD) modeling of spouted bed: Assessment of drag coefficient correlations. *Chem Eng Sci.* 2006;61(5):1401-1420.
35. Bokkers GA, Annaland MVS, Kuipers JAM. Mixing and segregation in a bidisperse gas-solid fluidised bed: a numerical and experimental study. *Powder Technol.* 2004;140(3):176-186.
36. Leboreiro J, Joseph GG, Hrenya CM, Snider DM, Banejee SS, Galvin JE. The influence of binary drag laws on simulations of species segregation in gas-fluidized beds. *Powder Technol.* 2008;184(3):275-290.
37. Hasimoto H. On the Periodic Fundamental solutions of the Stokes equations and their application to viscous flow past a cubic array of spheres. *J Fluid Mech.* 1959;5(2):317-328.
38. Sangani AS, Acrivos A. Slow flow through a periodic array of spheres. *Int J Multiphas Flow.* 1982;8(4):343-360.
39. Kim S, Russel WB. Modeling of porous-media by renormalization of the Stokes equations. *J Fluid Mech.* 1985;154(May):269-286.
40. Goldstein S. Concerning some solutions of the boundary layer equations in hydrodynamics. *P Camb Philos Soc.* 1930;26:1-30.
41. Ergun S. Fluid flow through packed columns. *Chem Eng Prog.* 1952;48(2):89-94.
42. Richardson J, Zaki WN. Sedimentation and fluidization: Part 1. *Trans. Inst. Chem. Eng. 32.* 1954:35-53.
43. Wen CY, Yu YH. Mechanics of fluidization. *Chem. Eng. Prog. Symp. Ser. 62.* 1966:100–111.
44. Gidaspow D. Hydrodynamics of fluidization and heat transfer: supercomputer modeling. *Appl. Mech. Rev. 39.* 1986:1–23.
45. Difelice R. The voidage function for fluid particle interaction systems. *Int J Multiphas Flow.* 1994;20(1):153-159.
46. Syamlal M, Rogers W, O' Brien TJ. A generalized drag correlation for multiparticle systems. *Tech. Rep., Morgantown Energy Technology Center DOE Report.* 1987.
47. Koch DL, Ladd AJC. Moderate Reynolds number flows through periodic and random arrays of aligned cylinders. *J Fluid Mech.* 1997;349:31-66.
48. Andrade JS, Almeida MP, Mendes J, Havlin S, Suki B, Stanley HE. Fluid flow through porous media: The role of stagnant zones. *Phys Rev Lett.* 1997;79(20):3901-3904.
49. Rojas S, Koplik J. Nonlinear flow in porous media. *Phys Rev E.* 1998;58(4):4776-4782.
50. Van der Hoef MA, Beetstra R, Kuipers JAM. Lattice-Boltzmann simulations of low-Reynolds-number flow past mono- and bidisperse arrays of spheres: results for the permeability and drag force. *J Fluid Mech.* 2005;528:233-254.
51. Yin XL, Sundaresan S. Drag law for bidisperse gas-solid suspensions containing equally sized spheres. *Ind Eng Chem Res.* 2009;48(1):227-241.

52. Yin XL, Sundaresan S. Fluid-particle drag in low-Reynolds-number polydisperse gas-solid suspensions. *AIChE J.* 2009;55(6):1352-1368.
53. Holloway W, Yin XL, Sundaresan S. Fluid-particle drag in inertial polydisperse gas-solid suspensions. *AIChE J.* 2010;56(8):1995-2004.
54. Zick AA, Homsy GM. Stokes-Flow through Periodic Arrays of Spheres. *J Fluid Mech.* 1982;115(Feb):13-26.
55. Koch DL, Sangani AS. Particle pressure and marginal stability limits for a homogeneous monodisperse gas-fluidized bed: kinetic theory and numerical simulations. *J Fluid Mech.* 1999;400:229-263.
56. Ladd AJC. Hydrodynamic transport-coefficients of random dispersions of hard-spheres. *J Chem Phys.* 1990;93(5):3484-3494.
57. Schiller L, Naumann A. A drag coefficient correlation. *V.D.I. Zeitung.* 1935.
58. Tanaka M, Kida S. Characterization of vortex tubes and sheets. *Phys Fluids a-Fluid.* 1993;5(9):2079-2080.
59. Nicolai H, Guazzelli E. Effect of the vessel size on the hydrodynamic diffusion of sedimenting spheres. *Phys Fluids.* 1995;7(1):3-5.
60. Nicolai H, Herzhaft B, Hinch EJ, Oger L, Guazzelli E. Particle-Velocity fluctuations and hydrodynamic self-diffusion of sedimenting non-brownian spheres. *Phys Fluids.* 1995;7(1):12-23.
61. Nicolai H, Peysson Y, Guazzelli E. Velocity fluctuations of a heavy sphere falling through a sedimenting suspension. *Phys Fluids.* 1996;8(4):855-862.
62. Segre PN. Origin of stability in sedimentation. *Phys Rev Lett.* 2002;89(25).
63. Segre PN, Herbolzheimer E, Chaikin PM. Long-range correlations in sedimentation. *Phys Rev Lett.* 1997;79(13):2574-2577.
64. Segre PN, Liu F, Umbanhowar P, Weitz DA. An effective gravitational temperature for sedimentation. *Nature.* 2001;409(6820):594-597.
65. Brenner MP. Screening mechanisms in sedimentation. *Phys Fluids.* 1999;11(4):754-772.
66. Caflisch RE, Luke JHC. Variance in the sedimentation speed of a suspension. *Phys Fluids.* 1985;28(3):759-760.
67. Ladd AJC. Hydrodynamic screening in sedimenting suspensions of non-Brownian spheres. *Phys Rev Lett.* 1996;76(8):1392-1395.
68. Ladd AJC. Sedimentation of homogeneous suspensions of non-Brownian spheres. *Phys Fluids.* 1997;9(3):491-499.
69. Ladd AJC. Effects of container walls on the velocity fluctuations of sedimenting spheres. *Phys Rev Lett.* 2002;88(4) :048301.
70. Thiele E. Equation of state for hard spheres. *J Chem Phys.* 1963;39(2):474-479.

71. Hartman M, Trnka D, Havlin V. A relationship to estimate the porosity in liquid solid fluidized-beds. *Chem Eng Sci.* 1992;47(12):3162-3166.

72. Ham JM, Homsy GM. Hindered settling and hydrodynamic dispersion in quiescent sedimenting suspensions. *Int J Multiphas Flow.* 1988;14(5):533-546.

73. Alnaafa MA, Selim MS. Sedimentation of monodisperse and bidisperse hard-sphere colloidal suspensions. *AIChE J.* 1992;38(10):1618-1630.

74. Di Felice R. The sedimentation velocity of dilute suspensions of nearly monosized spheres. *Int J Multiphas Flow.* 1999;25(4):559-574.

75. Garside J, Aldibouni MR. Velocity-voidage relationships for fluidization and sedimentation in solid-liquid systems. *Ind Eng Chem Proc Dd.* 1977;16(2):206-214.

76. Ladd AJC, Verberg R. Lattice-Boltzmann simulations of particle-fluid suspensions. *J Stat Phys.* 2001;104(5-6):1191-1251.

77. Koch DL. Hydrodynamic diffusion in dilute sedimenting suspensions at moderate Reynolds-numbers. *Phys Fluids a-Fluid.* 1993;5(5):1141-1155.

78. Fortes AF, Joseph DD, Lundgren TS. Nonlinear mechanics of fluidization of beds of spherical-particles. *J Fluid Mech.* 1987;177:467-483.

79. Chen YM, Jang CS, Cai P, Fan LS. On the formation and disintegration of particle clusters in a liquid solid transport bed. *Chem Eng Sci.* 1991;46(9):2253-2268.

80. Talini L, Leblond J, Feuillebois F. A pulsed field gradient NMR technique for the determination of the structure of suspensions of non-Brownian particles with application to packings of spheres. *J Magn Reson.* 1998;132(2):287-297.

81. Herrmann HJ, Hong DC, Stanley HE. Backbone and elastic backbone of percolation clusters obtained by the new method of burning. *J Phys a-Math Gen.* 1984;17(5):L261-L266.

82. Wylie JJ, Koch DL. Particle clustering due to hydrodynamic interactions. *Phys Fluids.* 2000;12(5):964-970.

83. Xiong QG, Li B, Chen FG, Ma JS, Ge W, Li JH. Direct numerical simulation of sub-grid structures in gas-solid flow-GPU implementation of macro-scale pseudo-particle modeling. *Chem Eng Sci.* 2010;65(19):5356-5365.

84. Li F, Lannin JS. Radial-distribution function of amorphous-carbon. *Phys Rev Lett.* 1990;65(15):1905-1908.

85. Wilhelm J, Frey E. Radial distribution function of semiflexible polymers. *Phys Rev Lett.* 1996;77(12):2581-2584.

86. Yarnell JL, Katz MJ, Wenzel RG, Koenig SH. Structure factor and radial-distribution function for liquid argon at 85degrees K. *Phys Rev A.* 1973;7(6):2130-2144.

87. Nijboer BRA, Vanhove L. Radial distribution function of a gas of hard spheres and the superposition approximation. *Phys Rev.* 1952;85(5):777-783.

88. Mason G. Radial distribution functions from small packings of spheres. *Nature.* 1968;217(5130):733-735.
89. Wertheim MS. Exact solution of the percus-yevick integral equation for hard spheres. *Phys Rev Lett.* 1963;10(8):321-323.
90. Hamid A, Yamamoto R. Direct numerical simulations of anisotropic diffusion of spherical particles in sedimentation. *Phys Rev E.* 2013;87(2):022310.
91. Bossis G, Brady JF. Self-diffusion of brownian particles in concentrated suspensions under shear. *J Chem Phys.* 1987;87(9):5437-5448.
92. Saffman PG. The lift force on a small sphere in the presence of a wall. *J Fluid Mech.* 1965;22(4):385-400.
93. Dennis SCR, Singh SN, Ingham DB. The steady flow due to a rotating sphere at low and moderate reynolds-numbers. *J Fluid Mech.* 1980;101(Nov):257-279.
94. Parthasarathy RN, Faeth GM. Turbulence modulation in homogeneous dilute particle-laden flows. *J Fluid Mech.* 1990;220:485-514.
95. Parthasarathy RN, Faeth GM. Turbulent dispersion of particles in self-generated homogeneous turbulence. *J Fluid Mech.* 1990;220:515-537.

List of publications

JOURNAL PAPERS

1. Ali Abbas Zaidi, Takuya Tsuji, Toshitsugu Tanaka, 'Direct Numerical Simulations of inertial settling of non-Brownian particles', *Korean Journal of Chemical Engineering*, (2014), (In Press).

2. Ali Abbas Zaidi, Takuya Tsuji, Toshitsugu Tanaka, 'Direct numerical simulation of finite sized particles settling for high Reynolds number and dilute suspension', *International Journal of Heat and Fluid Flow*, Vol. 50 (2014), pp. 330-341.

3. Ali Abbas Zaidi, Takuya Tsuji, Toshitsugu Tanaka, 'A New Relation of Drag Force for High Stokes Number Monodisperse Spheres by Direct Numerical Simulation', *Advance Powder Technology*, Vol. 25, No. 6 (2014), pp. 1860-1871.

INTERNATIONAL CONFERENCE PAPERS/MEETINGS

1. Ali Abbas Zaidi, Takuya Tsuji, Toshitsugu Tanaka, 'Hindered Settling Velocity & Structure formation during particle settling by Direct Numerical Simulation', The 7nd World Congress on Particle Technology (WCP7), Beijing, China, May 19 - 22, *Procedia Engineering*, (2014), in press.

2. Ali Abbas Zaidi, Takuya Tsuji, Toshitsugu Tanaka, 'Dynamic Behavior of Sedimenting Particles at Moderate Reynolds Number', 8th International Conference on Multiphase Flow, ICMF 2013, Jeju, Korea, May 26 - 31, (2013), ICMF2013-450.

3. Ali Abbas Zaidi, Takuya Tsuji, Toshitsugu Tanaka, 'Drag force relation by direct numerical simulation for gas-solid flows', 13th AIChE annual meeting, United States, (2013)

4. Ali Abbas Zaidi, Hirotaka Yada, Takuya Tsuji and Toshitsugu Tanaka, 'Microscopic DEM-CFD Coupling Simulation of Spouted Bed', Proc. of the 5th Asian Particle Technology Symposium (APT2012), Singapore, (2012), 078.

CONFERENCE PAPERS/SYMPOSIUMS IN JAPAN

1. Ali Abbas Zaidi, Takuya Tsuji, Toshitsugu Tanaka, 'Effect of domain size on velocity fluctuations of settling particles at finite Reynolds number', Japanese Society of Multiphase flow Symposium, (2013)

2. Ali Abbas Zaidi, Takuya Tsuji, Toshitsugu Tanaka, ‘Effect of domain size on microstructure in suspensions of solid spheres with moderate Reynolds number’, Japanese Society of Fluid Mechanics Annual Meeting, (2013)

3. Ali Abbas Zaidi, Takuya Tsuji, Toshitsugu Tanaka, ‘Effect of Stokes number on drag force for monodisperse spheres’, Japanese Society of Fluid Mechanics Annual Meeting, (2014)

Acknowledgments

This study was financially supported by Ministry of Education, Culture, Sports, Science and Technology, Japan from October 2010 to March 2014. We are grateful to Ministry for letting the author to stay and study in Japan without any financial burden. The author would also like to show deep thanks to Professor Toshitsugu Tanaka for accepting him as his PhD student and guidance throughout the research period. All the simulations were performed in Cybermedia Center, Osaka University and Academic Center for Computing and Media Studies, Kyoto University. We acknowledge their support and assistance.

The author would like to show thanks to Professor Takeo Kajishima, Professor Takeru Yano and Associate Professor Takuya Tsuji for their review of thesis and valuable comments. The author would also like to acknowledge the help from Assistant Professor Kimiaki Washino and all the lab. members especially Mr. Fujihara for his helpful discussion and to family and friends for their patience.

2014/01/14